2011-03-04

Facies Analysis and Reservoir Characterization of Subtidal, Intertidal, and Supratidal Zones of the Mudstone-rich Entrada Sandstone, South-Central Utah

Tanner Charles Hicks
Brigham Young University - Provo

Facies Analysis and Reservoir Characterization of Subtidal, Intertidal, and

Supratidal Zones of the Mudstone-rich Entrada

Sandstone, South-central Utah

Tanner C. Hicks

A thesis submitted to the faculty of
Brigham Young University
In partial fulfillment of the requirements for the degree of

Master of Science

Thomas H. Morris
John H. Mcbride
Scott M. Ritter

Department of Geology

Brigham Young University

April 2011

ABSTRACT

Facies Analysis and Reservoir Characterization of Subtidal, Intertidal, and
Supratidal Zones of the Mudstone-rich Entrada
Sandstone, South-central Utah

Tanner C. Hicks
Department of Geology, BYU
Master of Science

Understanding thickness variation and facies transitions in the mudstone-rich part of the Upper Middle Jurassic (Callovian) Entrada Sandstone depositional system is critical for constraining the paleogeography and evaluating the economic potential of Utah's Entrada Sandstone. Facies of the Entrada Sandstone in south-central Utah are dominated by mudstone-rich intertidal facies that were widespread within the Jurassic seaway. Intertidal deposits interfinger basinward with subtidal ooid-bearing shoals and bars, and landward supratidal sabkha, and erg-margin eolian deposits. Three sections were measured to improve understanding of the lateral and vertical facies transitions. Variations in thickness indicate the rate of developing accommodation space was high along the southwestern shoreline and relatively low along the northeastern shoreline during Callovian time. Although accommodation space was highest in the west, sediment supply from the west kept pace with, and eventually outpaced subsidence. In the east, sediment supply was significant but at one time was outpaced by subsidence, creating a complete range of facies, from subtidal to supratidal deposits. Along this eastern shoreline, erg-margin coastal dunes associated with the larger erg to the east eventually prograded westward. The variation in subsidence, sediment supply, and sediment source makes sequence stratigraphic correlation difficult.

Reservoir-quality sandstones are associated with muddy sections of the Entrada Sandstone within the San Rafael Swell. Porosity and permeability of the facies in this area indicate excellent reservoir potential in three of eight facies that were studied. Porosities of these potential reservoirs ranged from 11-22%, with permeabilities ranging from 44-430md. These high quality reservoir facies are surrounded by muddy, low reservoir-quality rocks, creating conditions amenable to the development of stratigraphic hydrocarbon traps.

Based on further study and a modern analog at the north of the Gulf of California, Hicks and others' (2010) depositional model for the Entrada Sandstone of south-central Utah has been modified to include newly interpreted facies. This improved depositional model may have predictive power in exploring for stratigraphic and combination traps within the Entrada system of Utah and analogous depositional systems throughout the world.

ACKNOWLEDGMENTS

TABLE OF CONTENTS

Chapter One

Facies Analysis of the Transitions Between Subtidal, Intertidal, and Supratidal
Zones of the Entrada Sandstone, South-central Utah: A Provisional
Sequence Stratigraphic Analysis

Chapter Two

Facies Analysis and Reservoir Characterization of the Mudstone-rich Portion of the Entrada
Sandstone, South-central Utah: Emphasis on the Bitter Seep Wash Sandstone at
South Salt Wash and Bitter Seep Wash

LIST OF TABLES

LIST OF FIGURES

Chapter 1

Chapter 2

PREFACE

 Chapter 1 of this thesis was published in UGA Guidebook 39 in 2010. It includes a regional thickness and facies analysis of the deposits within the Entrada Sandstone of south-central Utah. It also contains a provisional sequence stratigraphic framework for the Entrada Sandstone.

 Chapter 2 of this thesis summarizes facies analysis and reservoir characteristics in the mudstone-rich part of the Entrada Sandstone in south-central Utah. It emphasizes the facies analysis and reservoir characterization of the Bitter Seep Wash Sandstone (BSWS) found in South Salt Wash and Bitter Seep Wash on the west flank of the San Rafael Swell. Sedimentologic aspects of all facies are compared. A porosity vs. permeability cross plot allows the exploration geoscientist additional data with which to develop exploration strategies for the Entrada Sandstone within Utah and for analogous depositional systems elsewhere.

Chapter One

Facies Analysis of the Transitions Between Subtidal, Intertidal, and Supratidal
Zones of the Entrada Sandstone, South-central Utah: A Provisional
Sequence Stratigraphic Analysis

ABSTRACT

Facies analysis suggests that much of the late Middle Jurassic (Callovian) Entrada

Sandstone of south-central Utah is dominated by mudstone-rich intertidal facies. These intertidal

deposits interfinger with subtidal ooid-bearing shoals and bars as well as supratidal sabkha and

erg-margin eolian deposits. Three sections of the Entrada Sandstone in south-central Utah were

measured in detail to improve understanding of the lateral and vertical facies transitions away

from the understudied, mudstone-rich portion of the formation. Understanding facies transitions

is necessary for constraining the paleogeography and evaluating the economic potential of the

Entrada Sandstone as a hydrocarbon reservoir. The thickness of the Entrada Sandstone varies

from the southwest (369.1 m), to the north (194.9 m), and to the east (92.1 m), a lateral distance

of 193 km. This variation indicates that during Callovian time, the rate of developing

accommodation space was high along the southwestern shoreline and relatively low along the

northeastern shoreline. This is likely the result of the western sections being closer to the Jurassic

Western Cordilleran. Although accommodation space was highest to the west, sediment supply

from the west kept pace with, and eventually outpaced subsidence. To the east, sediment supply

was significant but was at one time outpaced by subsidence causing deposition of subtidal ooid-

bearing shoals and bars. The eastern section displays a complete range of facies, from the

subtidal to supratidal erg-margin. Along this eastern shoreline, erg-margin coastal dunes

associated with the larger erg to the east eventually prograded westward. The variation in

subsidence, sediment supply, and sediment source makes sequence stratigraphic correlation

difficult. We conclude that candidate sequences interpreted for each section cannot be correlated with certainty without the aid of absolute ages.

INTRODUCTION

Geographic Location

In this study we examine facies transitions of the Entrada Sandstone from Escalante northward, to the west and east flanks of the San Rafael Swell (figure 1). This region was chosen because the Entrada Sandstone is dominated by mudstone-rich rocks which have not been extensively studied (see Morris and others, 2005 for review). Facies transitions into more sandstone-dominated rocks to the south and east of the San Rafael Swell are of particular interest to geoscientists because they provide insights into the depositional history, paleogeography, and economic potential of the Entrada Sandstone.

Locations of the three sections range from south-southwest to north-northeast and include: the Escalante Composite (EC) section which is located along what was the southern end of the Jurassic Seaway, the western San Rafael Swell (WSRS) section located along the western margin of the seaway, and the eastern San Rafael Swell (ESRS) section located along the eastern margin of the seaway (figure 1). The EC and the WSRS sections were measured and interpreted for this study whereas the previously interpreted ESRS section was incorporated in an effort to better understand the Entrada Sandstone regionally (Marino, 1992; and Marino and Morris, 1996). The EC section included measuring section along both the Hole-in-the-Rock Road south of Escalante, and Posey Lake Road north of Escalante (see inset of figure 1). The WSRS section is located adjacent to South Salt Wash along Moore Road, approximately 24 km southeast of Ferron, Utah within the Short Canyon 7.5 minute quadrangle. The ESRS section is located

approximately 13 km west-southwest of Woodside, Utah adjacent to Summerville Wash within the Dry Mesa 7.5 minute quadrangle.

Geologic History

The Entrada Sandstone was deposited during late Middle Jurassic (Callovian) time approximately 161.2 to164.7 Ma (Sprinkel, 1994; Dickinson and Gehrels, 2003; Hintze and Kowallis, 2009). Preceding Entrada Sandstone deposition, much of central Utah was covered by a shallow seaway that waxed and waned during Bajocian and Bathonian time. This seaway, referred to as the Sundance or Carmel Sea, deposited much of the Carmel and Twin Creek Formations and, at its latest stage, the Arapien Shale (Kocurek and Dott, 1983; Sprinkel, 1994; Blakey and Ranney, 2008; Hintze and Kowallis, 2009). During Bathonian time, coastal dune fields persisted along the southern margin of the seaway and occasionally prograded over its broad tidal flats (Tanner, 1965; Kocurek and Dott, 1983).

As the sea continued to fluctuate through Callovian time, restricted marine and tidal flat environments formed within central Utah creating thick tidal flat (Smith, 1976) and sabkha deposits (Blakey and others, 1983; Blakey 1989). Coastal dune deposits (erg-margin) developed along the southern and eastern margins of the seaway in southern and eastern Utah. The erg-margin deposits interfingered with tidal flat and sabkha deposits (Kocurek and Dott, 1983; Blakey, 1989; Marino and Morris, 1996; Carr-Craybaugh and Kocurek, 1998; Morris and others, 2005). Entrada Sandstone eolianites are thickest and most extensive in eastern Utah and constitute the Slickrock Member of the Entrada Sandstone in Arches National Park and in the Moab, Utah area (Kocurek and Dott, 1983).

The J-3 unconformity overlies the Entrada Sandstone throughout southern, eastern, and central Utah. The unconformity is overlain by the Curtis Formation and locally by the

Summerville Formation, which were deposited in a marine foreland basin (Smith, 1976; Sprinkel, 1994; Hintze and Kowallis, 2009; Perkes, in prep). The nature of the unconformity between the Entrada Sandstone and the Curtis Formation is largely a disconformity although locally it can be an angular unconformity (Keach and others, 2006). The Jurassic Cordillera foreland trough narrowed and the axis migrated eastward and northward during deposition of the Curtis Formation (Blakey and Ranney, 2008; Perkes, in prep).

Purpose

The transitions between mudstone-dominated, marine-influenced facies and sandstone-dominated erg-margin facies of the Entrada Sandstone have been recognized as potential stratigraphic and combination traps for hydrocarbon accumulations (Marino and Morris, 1996; Morris and others, 2005; Keach and others, 2006). Based on this model, hydrocarbon production has recently been established from the Entrada Sandstone within the Uinta Basin. (Eckels and others, 2005). There exists further potential for development of this play in south-central Utah where these facies transition in the subsurface, especially where they are overlying and subjacent to Cretaceous rocks which have proven to be a potential source and seal for hydrocarbons. The Entrada Sandstone is bleached in numerous locales in south-central Utah, indicating a history of subsurface fluid movement, possibly hydrocarbons, through these rocks (Beitler and others, 2003). Sandstone bodies of reservoir-quality within the mudstone-dominated section can potentially accumulate hydrocarbons. The greatest known potential for stratigraphic traps is in areas where mudstone-dominated facies transition into the erg-margin and erg-proper facies to the east and south. In the present study we define facies within and laterally associated to the mudstone-dominated Entrada Sandstone interval located in south-central Utah. Ultimately, the depositional history and paleogeography of the Entrada Sandstone cannot be complete without

these detailed analyses. Our study assists in the broader need to understand facies transitions and, for the first time, place the south-central portion of the Entrada Sandstone into a preliminary sequence stratigraphic framework. Our study also serves to better understand the paleogeographic evolution of the late Middle Jurassic Interior Seaway and its associated margins. This may aid exploration and production strategies targeting the Entrada Sandstone. All of these efforts, however, require detailed facies analysis.

Methods

Based on previous paleogeographic reconstructions, we chose three study locations that incorporate subtidal, intertidal, and supratidal transitions in south-central Utah (figure 1). Our interpretations use a modified version of published tidal flat models (Klein, 1972; Galloway, 1986; and Dalrymple and others, 1992) and supratidal erg-margin models (Kocerek and Havholm, 1991) (figure 2). A total of 657 m of outcrop was measured at sufficient detail to interpret facies and to establish facies changes. These changes were defined by significant surfaces. Units in each section were defined by changes in lithology and sedimentary characteristics. At each location we photographed, described, and categorized the meso- and macro-scale primary and secondary sedimentary structures as well as stratigraphic characteristics. These include lithology, bedforms, grain size, bounding surfaces, sandstone body geomorphology, cyclic bedding, and other notable characteristics. The measured sections were then placed into a preliminary sequence stratigraphic framework. In places there are anomalous sandstone bodies that are understudied and poorly defined relative to depositional processes. Future work will focus on these bodies as part of a reservoir characterization study.

FIELD DATA

Escalante Composite Section

Escalante, Utah is a region with spectacular exposures of the Entrada Sandstone. In this region, the Entrada Sandstone is comprised of three formal members, in chronological order: the Gunsight Butte Member, the Cannonville Member, and the Escalante Member (figure 3) Doelling and others, 2000; Hintze and Kowallis, 2009). Our composite section was measured in three locations near Escalante in order to measure the best exposures of each member. The cumulative thickness of the Entrada Sandstone is 369.1 m in the Escalante area. The Gunsight Butte Member and Cannonville Member were measured north of Escalante along Posey Lake Road (see figure 1 inset). We measured 133 units in the Gunsight Butte Member and 118 units in the Cannonville Member. The Escalante Member, which contains 91 units was measured southeast of Escalante along Hole-in-the-Rock Road, near Devil's Garden National Monument. We simplify and summarize the important units of each member below under the subheading of Data/Observations. Descriptions of the units within these members begin with the basal unit and continue upward.

We broadly interpret which parts of the subtidal, intertidal and supratidal zones are represented within each member (figure 4). It should be noted that on this relatively broad, flat coastal region, facies transitions occur frequently. This is due to the fact that small changes in base-level, sediment supply, and/or subsidence or uplift would dramatically shift the position of the shoreline, especially if the facies belts are relatively narrow. Therefore, we summarize here only the larger, general shifts seen in each member of the Entrada Sandstone. Furthermore, within tidal flat depositional systems, grain size generally diminishes in a landward direction because the transport energy is received from the ocean. This is in distinct contrast to a standard marginal marine shoreface system in which grain size increases in a landward direction.

Gunsight Butte

The Gunsight Butte Member of the Entrada Sandstone is the basal member in the Escalante area and is approximately 138.1 m thick (figure 4). It underlies the Cannonville Member of the Entrada Sandstone and overlies the Carmel Formation (figure 3). The Carmel Formation is exposed in the study area but the contact with the Entrada Sandstone is often covered by Quaternary deposits. The Gunsight Butte Member was measured 6 km north of Escalante from an outcrop on the west side of Posey Lake Road. GPS coordinates of this location are: 37˚48'55.10"N 111˚38'02.99"W.

Data/Observations: The basal unit of the Gunsight Butte Member of the Entrada Sandstone is a 3.3 meter thick calcareous siltstone bed with asymmetrical ripple lamination. The contact with the underlying Carmel Formation is sharp. Tinted greenish-gray, this unit is laterally extensive, slope-forming, and grades vertically into a 1.5 m thick, reddish, fine-grained sandstone. The sandstone is calcite cemented, laterally extensive, and contains asymmetrical ripple lamination. This 1.5 m unit is bounded above by a sharp contact. The overlying 45 m interval of section is dominated by red mudstone. This mudstone is poorly cemented with calcite, laterally extensive, and is very recessive. Convolute bedding is observed in the basal beds of this mudstone. In the upper half of this mudstone bed there is a 0.3 m thick coarse-grained sandstone that is well cemented. This sandstone grades vertically into a 5.5 m thick fine-grained sandstone that is laterally extensive and displays alternating ripple lamination and "wavy" laminations interpreted to represent either thin flaser ripple lamination or disturbed algal mats.

The 45 m thick mudstone-dominated interval is truncated by a reddish brown to reddish orange, very fine-grained sandstone that is moderately to well-cemented. This sandstone-dominated unit is 37 m thick and contains three 2 m thick packages of mudstone. Each package is composed of several mudstone beds. The mudstone beds are generally pale reddish brown and

form slopes. These mudstone beds alternate with moderate orange pink, very well sorted, fine-grained, ledge-forming sandstone beds. Sandstone beds between the packages contain high angle trough cross stratification (TCS) from a meter to several meters thick, wavy-laminated strata, and occasional polygons exposed on bedding planes (figure 4, picture A). Several sandstone beds display three-dimensional ripple lamination.

The next 4.0 m of section contain alternating 0.5 m thick, pale reddish brown, fine-grained, ledge-forming sandstone beds and 10 cm thick slope-forming mudstone beds (figure 4, picture B). The sandstone beds are laterally extensive and display both low angle TCS and planar lamination.

The sandstone and mudstone pattern changes for the next 10.2 m with the sandstone beds transitioning to approximately 15 cm thick, grayish orange pink, slope-forming sandstone beds. They are moderately cemented and interbedded with equal thickness, pale reddish brown, slope-forming mudstone beds.

The overlying 5.6 m of section is comprised of grayish orange pink to moderate orange pink, well rounded, well sorted, fine- to very fine-grained sandstone beds. Some of these sandstone beds display low angle TCS and asymmetrical ripple lamination. Within one sandstone, there is a 0.3 m thick, sub-rounded, moderately sorted, coarse-grained sandstone.

Well sorted, well rounded, fine- to very fine-grained sandstone beds alternate between slopes and ledges for the next 15 m. These sandstone beds are mottled (bioturbation?) and several sandstone beds contain flame structures, rootlets and secondary nodules.

The next 8.5 m consist of pale reddish brown, well sorted, well rounded, fine-grained sandstone beds that are thin bedded, ledge-forming, and laterally extensive. These sandstone

beds display low and high angle TCS. The sandstone beds alternate with poorly cemented siltstone beds which are slope-forming and laterally extensive.

The uppermost 9.0 m of section consists of well sorted, well rounded, moderate orange pink, ledge-forming sandstone beds that alternate with pale reddish brown, slope-forming mudstone beds. The sandstone beds display high angle TCS, apparent festoon cross stratification and asymmetrical ripples with ripple indices of 15 or lower. One laterally extensive fine-grained sandstone reverse grades into a medium-grained sandstone.

Interpretations: The Gunsight Butte Member of the Entrada Sandstone in the Escalante, Utah area broadly represents a coarsening upward succession of siliclastic facies. The 45 m interval of the section near its base is the finest grained, mudstone-dominated part of the Gunsight Butte Member. This interval is interpreted to have been deposited in the high intertidal facies wherein tidal channels were small, subtle, and transported only very fine sand-, silt-, and clay-sized sediment (Klein, 1972). This area would be located in the most landward portion of the intertidal flat and possibly in the most seaward portion of the supratidal zone.

The overlying 37 m are interpreted to represent the encroachment of small coastal eolian dunes into the area. These small dunes deposited well sorted, fine-grained sandstone beds. Interdunal areas produced algal mats which are recorded in the rock record as whispy, wavy laminae. Occasional flood events produced the mudstone-dominated interbeds which became desiccated during regressions and dry intervals. This facies belt represents a supratidal sabkha that preserved parts of small migrating eolian dunes. The sabkha resulted from a relative fall in base level in this area. Thus, this facies prograded over the underlying high intertidal facies.

The upper interval (approximately 51.3 m) of the Gunsight Butte Member is interpreted as the middle intertidal facies. This middle intertidal facies is characterized by sandstone-rich

tidal channels and overbank mudstone. This interpretation suggests that relative to the underlying 37 m portion of the section, there must have been a relative rise in sea-level. Thus, the Gunsight Butte Member records an initial fall in relative sea-level and a subsequent rise.

Cannonville

The Cannonville Member was measured along the west side of Posey Lake Road, approximately 10 km north of Escalante. The GPS coordinates at the base of this section are: 37˚51'12.29"N 111˚38'02.99"W.

Data/Observations: The first of many white, fine- to very fine-grained sandstone beds mark the bottom contact of the Cannonville Member with the Gunsight Butte Member (figure 4, picture C). With an approximate total thickness of 140.5 m, it differs from the Gunsight Butte Member in that its alternations between fine-grained sandstone beds and mudstone beds in the lower 26.5 m of the section become more repetitive. Within the basal 26.5 m interval, there are 0.1 to 0.8 m thick, light colored sandstone beds alternating with 0.25 m thick, pale reddish brown mudstone beds. The sandstone beds display low to high angle TCS, planar lamination, flame structures, algal mats, rootlets, fluid escape structures including remnant collapsed mud volcanoes (figure 4, picture D), and rare mud-filled channel scours between sandstone and mudstone beds (figure 4, picture E). Fluid escape structures also include dish and pillar structures (figure 4, picture F). The sandstone beds alternate with the mudstone beds and very fine-grained laminated silty sandstone beds.

The next 34.7 m interval of the section is dominated by fine- to medium-grained sandstone beds. Very thick bedded (up to 8.7 m), very light colored sandstone beds become interbedded with approximately 0.4 m thick, pale reddish brown sandstone beds. Both the brown and very light gray sandstone beds are well sorted, rounded, and fine- to medium-grained. They

are poorly cemented and form slopes. Two ledge-forming layers, 0.3 and 0.1 m thick, respectively, are found in the lower 20 m of this 34.7 m interval. These two beds display high angle TCS and one has a scoured contact.

The next 39.2 m interval of the Cannonville Member is a thick span of alternating sandstone and mudstone beds. The anonymously colored pale greenish yellow sandstone beds are well sorted, rounded, and fine-grained. Although they are poor to moderately cemented and slope-forming, they appear massive in outcrop view. Weathering makes it difficult to see bedding and primary sedimentary structures. The thickest sandstone bed is 16 m thick. The mudstone beds are pale red, slope-forming units transitioning at the top to a dusky red, moderately cemented mudstone.

The next stratigraphic interval of the Cannonville Member is only 20.1 m thick. The basal-most beds of this interval comprise 4.7 m of section. Lithologically, the 4.7 m is comprised of thick bedded, pale reddish brown, very well sorted, well rounded, fine-grained sandstone. The sandstone is friable and slope-forming and is interbedded with thin siltstone beds, some of which display bioturbation. Approximately 1 m above the base of the interval is a candidate ash layer (figure 4, note asterisks designating candidate ash beds). It is 7 cm thick and is sandwiched between two bleached units. It has a soapy texture. Overlying the 4.7 m interval are 3 m of alternating red and light-colored fine-grained sandstone beds. These sandstone beds are well sorted, well rounded, friable, and slope-forming. The next 2 m is largely a pale olive, slope-forming siltstone. It is divided by two thick bedded sandstone beds that are lensoidal, have TCS, are friable, and are ledge-forming. The 2 m siltstone bed is bounded on the bottom and top by slope-forming sandstone beds. Another candidate ash bed with a soapy texture and pale olive color is included in this siltstone bed. The overlying 8.2 m is comprised of fine- to very fine-

grained sandstone beds and sand-rich siltstone beds. Bioturbation is evident in the siltstone beds and low angle TCS is present in some ledge-forming sandstone beds.

The uppermost 20 m of the Cannonville Member is dominated by light colored, sand-rich siltstone beds that are largely nondescript and slope-forming (figure 4, picture G). The basal portion of this interval is a relatively continuous, light colored, very thick bedded, slope-forming, sand-rich siltstone bed which transitions from 15 percent yellow banding at the bottom to 60 percent yellow banding near the top. This yellowish banded interval is obvious when viewing the outcrop from a distance. Overlying this banded unit there is a 4.1 m well sorted, sand-rich siltstone bed that changes from a pale yellow brown to a grayish orange color. It continues to be slope-forming.

Interpretations: The lower 61.2 m of the Cannonville Member broadly coarsen upward. In an intertidal depositional setting, this grain size change suggests relative sea-level rise. The ratio of sandstone to mudstone and siltstone increases up section and the individual sandstone beds become thicker. We interpret the basal 26.5 m to be middle intertidal facies where interbedded mudstone and sandstone beds are prominent. The next 34.7 m of the Cannonville section are sandstone-dominated and interpreted to be the lower intertidal facies (Klein, 1972). The overlying 39.2 m are fine sandstone beds alternating with lesser mudstone beds. This section represents the lower part of the middle intertidal facies. The next interval of 20.1 m is interpreted as middle intertidal facies. This is evidenced by interbeds of scoured, low and high angle TCS sandstone beds that occasionally contain coarse sand grains at their bases. We interpret these sandstone beds to be shallow intertidal channels. The uppermost 20 m are dominated by non-descript siltstone beds. We interpret this interval to represent the high intertidal facies that is transitioning into the supratidal zone. In this depositional setting it is difficult for high energy

processes to dominate. Instead, low energy dominates as small tidal channels flood broad areas with mud and silt. Sand grains are incorporated by eolian processes of the supratidal sabkha

In summary, we interpret the Cannonville Member to be deposited within the lower, middle, and high intertidal zones. There was a relative sea-level rise from the basal Cannonville through the middle interval. This was followed by a relative fall during the last part of Cannonville time.

<u>Escalante</u>

The Escalante Member is the uppermost member of the Entrada Sandstone and forms a contact with the overlying Summerville Formation or possibly Tidwell Member of the Morrison Formation (Doelling, personal communication) which is thin and appears to pinch and swell in this area (figure 4). There is no Curtis Formation in this section. The Escalante Member can be broadly divided into two intervals (figure 4). The lower stratigraphic interval is relatively thin (13 m) in comparison to the upper interval which is 77.5 m thick. Sandstone of eolian origin dominates the upper interval of the Escalante Member whereas slope-forming siltstone beds dominate the lower interval. The outcrop measured for the Escalante Member is along cliffs northwest of Devil's Garden National Monument along Hole-in-the-Rock Road (figure 1). GPS coordinates of the location are: 37˚34'58.89"N, 111˚,25"55.62" W.

Data/Observations: The lower 13 m interval of the Escalante Member is comprised of very pale orange, well sorted, rounded, sand-rich siltstone beds that alternate with yellowish gray mudstone. The sand-rich siltstone beds are laterally extensive, slope-forming units of 1 to 6 m in thickness and the mudstone beds are 10 cm thick. The mudstone beds are moderately sorted and slope-forming. The sand-rich siltstone beds transition into a 4.5 m thick, well sorted, well rounded, fine-grained sandstone bed with rootlet traces.

The transitional 4.5 m sandstone is considered the base of the upper interval of the Escalante Member. A 0.70 m thick portion of this sandstone is interbedded with 1-2 cm thick, pale olive mudstone beds. Herringbone cross stratification and soft sediment deformation is observed within the sandstone (figure 4, pictures H and I). The overlying 73 m is dominantly comprised of well sorted, well rounded, fine-grained sandstone beds that display high angle TCS. This part of the section forms cliffs. These sandstone beds transition from dark yellowish orange at the base to grayish orange pink in the middle to yellowish gray at the top. The high angle TCS sets become thicker up section. The basal 1/3 of the 73 m section is more likely to contain fluid escape structures, convolute bedding, rootlets, and herringbone cross stratification (figure 4, picture H). Six interbeds of wavy laminated silty sandstone beds punctuate the high angle TCS sandstone beds (figure 4, pictures J and K). These six interbeds range from 0.3 m to 3.7 m thick. In the middle of the 73 m is 3.1 m of slope cover. The basal 0.1 m of this slope cover is partially exposed. It consists of a recessive, dark reddish brown, friable mudstone bed.

Interpretations: The two-part Escalante Member is relatively easily interpreted. The lower 13 m are dominated by non-descript siltstone and mudstone beds. We interpret this interval to represent the high intertidal facies that is transitioning into the supratidal zone. It is difficult for high energy processes to dominate in this depositional setting. Low energy processes deposit mud and silt in broad areas between small tidal channels.

The upper 77.5 m interval is dominated by erg-margin eolian dunes and interdunal areas of the supratidal erg-margin. However, within the basal 6 m of this interval, thin interbeds of mudstone encompass lensoidal, thin bedded sandstone. These sandstone beds represent small tidal channels that are underlying the thick succession of eolian sandstone. They indicate the transition from largely tidally influenced deposits to supratidal deposits. The overlying sandstone

is fine-grained, well sorted, well rounded, and displays abundant and relatively thick sets of low and high angle TCS, typical of eolian dune sets. Between dune sets, algal-matted interdunal deposits accumulated to significant thickness (figure 4, picture J). The algal mats attest to wet surface conditions between dune sets. The algal mat deposits have been described within the Entrada erg-margin setting by numerous authors (Kocurek, 1981; Kocurek and Havholm, 1991; Carr-Craybaugh and Kocurek, 1998; Morris and others, 2005; Monn, 2006). Most of the upper 77.5 m section is bleached white indicating some post-depositional fluid transfer through these sandstone beds (Beitler and others, 2003).

In summary, the Escalante Member of the Entrada Sandstone in the Escalante study area displays transitional facies from the high intertidal to supratidal erg-margin. Broadly, this represents a relative fall in sea-level and associated nearshore progradation of sedimentary facies.

West San Rafael Swell Section

Salt Wash is approximately 24 km southeast of Ferron, UT on the west flank of the San Rafael Swell. It is a large strike valley formed by erosion of the lower interval of the Entrada Sandstone. The total thickness of 194.9 m was divided into three distinct intervals based on lithologic and geomorphologic characteristics (figure 5). There were 116 units measured. We simplify and summarize the important units of each member below.

Interval 1 (Lower)

Data/Observations: Interval 1 has a cumulative thickness of 90.8 m. The basal section has a sharp contact with the underlying Carmel Formation. The first 32 m of interval 1 are very recessive and dominated by slope cover. Within the slope cover three reddish-brown, very thickly bedded, calcareous siltstone beds are exposed which contain many cross-cutting gypsum

stringers and show signs of soft sediment deformation. The silty unit is overlain by a 2.9 m siltstone bed with apparent low-angle TCS that coarsens up section. A 1.4 m reddish brown siltstone bed overlies the previous siltstone beds but does not have any visible bedforms. It is better cemented, has disturbed bedding, and has gypsum stringers near its base. Overlying this siltstone bed is 2.5 m of very fine-grained sandstone. This sandstone has very disturbed bedding, ball and pillow structures, and where exposed, a very distinct meter-scale polygonal surface (figure 5, picture A; see modern analog from the Namibia coast figure 5, picture B). This is overlain by a 0.6 m slightly finer-grained sandstone that contains some low angle TCS as well as another polygonal surface and is bleached white at its upper contact. Locally this surface displays concentrations of gypsum nodules.

Overlying this sandstone bed is a medium bedded 0.15 m dark purple claystone bed containing fairly euhedral biotite crystals. It is poorly cemented, does not react with diluted HCl, and it is very laterally extensive. It is considered a candidate ash bed. It is overlain by a 0.2 m thick bleached white, poorly sorted, very fine-grained sandstone cemented with calcite.

Overlying the bleached sandstone are 15 m of reddish brown, silty mudstone beds. Above this there is a very thickly-bedded (3.35 m), dark reddish brown, moderately well-sorted, very fine-grained sandstone bed. It is well cemented with calcite, laterally extensive, and forms a small ledge. The next 7.9 m are reddish brown, poorly sorted, silty sandstone beds. Overlying the silty sandstone beds is a thin bed (0.05 m) of purple claystone. It is laterally extensive and very similar to the purple claystone bed stratigraphically below; however, it does not have any visible biotite or bleaching in the rocks above or below. The next 0.95 m are reddish brown mudstone. This mudstone is capped by a 0.05 m light green calcite-rich bed that appears to be laterally

extensive and has polygonal to circular impressions throughout that are approximately 0.75 cm in diameter.

The next 23.3 m are dominantly reddish brown, poorly sorted, silty sandstone beds. The silty sandstone beds are laterally extensive, and contain no visible bedforms. Within this section are three sandstone beds, ranging in thickness from 0.2 m to 3 m. The two medium-bedded sandstone beds are light gray, calcite cemented, and very fine-grained. They are laterally extensive and contain climbing.

The final three units of Interval 1 represent a coarsening upward succession. The lowest unit is 1.8 m of reddish brown mudstone. It is interbedded with laterally continuous laminae of light gray silty sandstone. Overlying this mudstone is 0.35 m of light gray, moderately sorted, very fine sandstone. It is well cemented, laterally continuous, and contains unidirectional climbing ripples oriented approximately at 60° azimuth (figure 5, pictures C and D). The caprock is 1.1 m of reddish brown, moderately sorted, subrounded, very fine sandstone (figure 5, pictures E, F, and G). It is well cemented, laterally continuous, and contains small ripple lamination and rare ooids.

Interpretations: Interval 1 is interpreted as the middle intertidal facies with two periods of sea-level fall when sabkhas were present. It is capped by middle intertidal channel sandstone deposits. The units suggest a relatively stable position in sea-level.

The silty sandstone beds throughout this section are mottled or have disturbed bedding and are interpreted to be the middle intertidal facies. They were deposited by low energy tidal currents. Inter-channel areas were occasionally subaerially exposed.

Both sabkha deposits within Interval 1 indicate a period of time when relative sea-level dropped, leaving desiccation features (Kocurek and Hunter, 1986). Bedding is highly disturbed;

however, there were no indications of bioturbation in this interval so it is possible this was caused by dissolution or reworking of mud cracks. During the dry periods when sea-level was low, evaporites were deposited and over time dissolved, producing disturbed bedding. Disturbed bedding could have also resulted from mud cracks being broken and rounded by weak tidal currents. The lack of bioturbation may be due to a hypersaline environment associated with a sabkha or tidal flat.

The sandstone beds at the top of Interval 1 contain climbing ripples indicating a high influx of sediment. Large amounts of relatively coarse sediment suggest the middle intertidal environment. This requires a relative rise in sea-level. This rise brings stronger tidal channel currents, storm deposits, and potentially subtidal ooids into the middle intertidal zone (Galloway, 1986). The gypsum stringers crosscut bedding and are therefore post depositional.

In summary, Interval 1 of the West San Rafael Swell section displays a slight rise in sea-level. It is dominated by the middle intertidal facies but includes two sabkha (supratidal) incursions.

Interval 2 (Middle)

Data/Observations: Interval 2 has a cumulative thickness of 30.9 m and begins about 91 m from the base of the section. It is composed of approximately eight repetitive cycles of fining upward successions.

The lower 1/3 of each fining upward succession are sandstone beds containing climbing ripples and some TCS (figure 5, picture D). The upper 2/3 are primarily dark to reddish brown, slope-forming, silty mudstones and sandstone with gypsum stringers throughout. Some contain thin sandstone stringers with small ripple lamination. Several of the muddier sections had

18

reduction spots near their upper contact with the sandstone of the next succession. In the middle of Interval 2, there is a sandstone with small gypsum nodules within disturbed "krinkly" beds.

Near the top of Interval 2 there is a sandstone with mud-draped ripple lamina (possible double draped lamina; figure 5, pictures H and I) and a clearly visible fluid escape structure. A very thick bed (2.8 m) of reddish brown silty sandstone exists approximately 1 m below the upper contact of Interval 2. This silty sandstone has polygonal surfaces and a mottled look similar to those seen in Interval 1.

Interpretations: This section is interpreted to be a succession of fining upward repetitive cycles that are parasequence-scale. Each cycle fines upward from the sand-rich middle intertidal to the finer-grained high intertidal facies. The mudstone beds above the sandstone beds tend to be interbedded with fine sandstone containing ripple lamination. The interbedded sandstone within these mudstone beds could indicate relatively higher energy conditions on the high intertidal facies such as would be produced by storms and tidal channels.

The sandstone in the middle of Interval 2 with "krinkly" beds and gypsum nodules may have been deposited and formed by desiccation of the sediment. When sea-level falls it allows evaporites to be deposited and through dissolution disturbs the bedding. This sandstone is relatively coarse and was likely deposited in the middle intertidal facies by intertidal channels.

Within the upper 1/3 of Interval 2 double draped lamina are present and likely represent deposition within the middle intertidal facies. Maximum flood or ebb velocities deposit the sand and during slack water, mud falls out of suspension, settling on the sand. Located within the double draped lamina interval there is an obvious fluid escape structure, indicating that it was a very wet environment such as the intertidal facies.

In summary, during Interval 2, sea-level seems to be relatively constant depositing high intertidal to middle intertidal sediments. Occasional pulses of sea-level rise or possibly storm events affected the tidal flat. These rises allowed deposition of the relatively coarser middle intertidal sandstone beds. Desiccation features at the top of Interval 2 indicate another drop in sea-level.

<u>Interval 3 (Upper)</u>

Interval 3 has a cumulative thickness of 73.2 m. The contact between Intervals 2 and 3 is marked by an abrupt end to the stepped topography of Interval 2, and the beginning of a large cliff with many "hoodoo" beds.

Data/Observations: The basal unit of this interval is a 4.65 m thick, dark brown silty mudstone. It is laterally continuous and contains several very thin beds of sandstone. Overlying this unit is a 0.35 m reddish brown, moderately sorted, fine-grained, subangular sandstone with a very thin bed of gypsum. An 8.5 m dark brown, silty sandstone overlies the previous sandstone. It has a high concentration of gypsum nodules near its upper contact. It is somewhat mottled and displays desiccation polygons. Overlying this silty sandstone is 2.55 m of reddish brown, poorly sorted, medium- to fine-grained sandstone. There are disturbed patches of medium-grained sandstone surrounded by fine-grained sandstone. This sandstone is laterally extensive and capped by a 0.95 m thick, massive sandstone. This massive sandstone is one of the coarsest beds in the WSRS section and has a somewhat mottled appearance. The next 3.35 m is coarsening upward from mudstone to siltstone to sandstone at approximately 1 meter scale. The upper sandstone is laterally extensive, thinly laminated, has low angle ripple lamination, and some mudstone lamina. The next 5.25 m are dominated by silty sandstone. One thick bed of sandstone (0.8 m) lies near the basal portion of this section. The silty sandstone beds have disrupted bedding which

gives it a somewhat mottled look. One of the silty sandstone beds has thin- to medium-beds that contain silt-draped ripple lamination. This bed weathers out into hoodoos. The uppermost silty sandstone has gypsum nodules throughout. Overlying the silty sandstone is a 13.1 m reddish brown, poorly sorted sandstone. It is laterally extensive and has disturbed bedding, soft sediment deformation, and weathers out into hoodoos. Gypsum nodules and stringers are more concentrated in the lower portion of this rock, although they are present throughout. Some of the gypsum nodules tend to follow laterally continuous horizons. The sandstone coarsens upward and has a mottled appearance. The next sandstone is 3.5 m thick and is the same as the previous sandstone, except that it does not contain any gypsum nodules or stringers. Overlying this sandstone is 0.45 m of dark brown mudstone. This unit is also laterally extensive. There is a 0.35 m light colored, fine-grained sandstone overlying the mudstone. The sandstone is laterally extensive, has planar to low angle TCS, and is capped by a thin bed of silty sandstone that pinches and swells. 1.15 m of reddish brown, fine-grained sandstone overlies the previous bed, is laterally extensive, and has ripple lamination near the base capped by low-angle TCS. The next 3.1 m are reddish brown, well sorted, very fine- to fine-grained sandstone beds. The lower sandstone beds have climbing ripples. The lower portion is interbedded with very thin beds of mudstone. The overlying sandstone displays planar to low-angle TCS. The uppermost sandstone has soft sediment deformation and weathers out into hoodoos. A thick bed (0.5 m) of dark brown mudstone overlies the 3.1 m of sandstone beds. The mudstone bed is laterally extensive and has areas with reduction spots. There are a few very thin, laterally extensive beds of sandstone which display small ripple lamination. The following 1.55 m is dominated by reddish brown, fine-grained sandstone beds. The sandstone beds are laterally extensive and are massive. Within these sandstone beds is another thin purple bed, similar to the one seen in Interval 1 with bleaching

above and below. This is also a candidate ash bed. These sandstone beds are overlain by 0.2 m of dark brown mudstone with numerous reduction spots. The next 5.5 m is reddish brown, poorly sorted, silty sandstone. This silty sandstone is laterally extensive, has disturbed bedding and signs of soft sediment deformation. Halfway up it contains a medium-grained sandstone bed. The lower portion of this 5.5 m silty sandstone has a few lamina where gypsum nodules are concentrated. These tend to be the recessive layers within hoodoos.

The final 17.3 m of strata in the WSRS section have a slightly higher ratio of sandstone to siltstone. The sandstone beds are reddish brown, moderately sorted, and very fine- to medium-grained. The sandstone beds near the base of this portion of Interval 3 have some planar bedding and small scours. The siltstone beds tend to weather out into hoodoos. The sandstone beds near the top of this section have ripple lamination, low-angle TCS, climbing ripples, and some mud-draped ripple lamination. Some of the mudstone beds contain thin white sandstone lamina, some of which are ripple laminated.

Interpretations: Interval 3 is interpreted to have been initially dominated by the middle intertidal facies. The high intertidal to sabkha facies was deposited later in its depositional history.

The lower half of Interval 3 is interpreted as middle intertidal deposits. The disturbed bedding and soft sediment deformation indicate a fairly wet environment as predicted in the middle intertidal zone. It is coarser grained than the overlying upper section.

The upper half of Interval 3 is interpreted as the high intertidal to sabkha facies. As sea-level dropped it allowed the high intertidal and muddy sabkha facies to be deposited in a low energy environment. The relatively thin sandstone beds in this interval are likely small tidal channel or storm deposits. There are beds with gypsum nodules that are interpreted to be exposed

evaporative surfaces. There are some coarser-grained sediments in this upper half that represent short pulses of middle intertidal deposition.

Within Interval 3 there is an overall fall in sea-level. High intertidal to sabkha facies prograded over middle intertidal facies in this area. This West San Rafael Swell (WSRS) section only records deposits of middle intertidal to supratidal sabkha zones.

East Flank San Rafael Swell

Marino (1992) and Marino and Morris (1996) interpreted nine sedimentary facies in a measured section of the Entrada Sandstone which is located on the east flank of the San Rafael Swell adjacent to Summerville Wash (figure 1). Their section is 92.1 m in cumulative thickness and is summarized and used herein (figure 6). This section can be broadly separated into six intervals. The basal interval is interpreted to be dominated by mudstone and silty mudstone of the high intertidal facies. Interval two contains cross bedded sandstone beds that contain up to 30% ooids suggesting a very shallow subtidal depositional setting (figure 6, pictures A and B) (Galloway, 1986). Interval 3 is dominated by silty mudstone interpreted to be located in the high intertidal zone. Interval 4 contains cyclic, parasequence-scale, fining upward successions interpreted to be deposited within the middle intertidal to lower intertidal facies (figure 6, picture C). Marino (1992) and Marino and Morris (1996) also interpreted two sandstone beds in this interval as being deposited in the "shoreface to foreshore" setting. Interval 5 is an eolian sandstone representing typical Entrada Sandstone erg-margin facies displaying interbeds of high angle trough cross stratification and interdunal algal mat deposits. Interval 6 is composed again of silty mudstone and silty sandstone of the middle to high intertidal facies (figure 6, picture D).

SEQUENCE STRATIGRAPHY

We herein provide a preliminary analysis of the sequence stratigraphy of the three measured sections. Given the variable thicknesses of the three sections and the variation in the number of candidate sequences, correlation between sections can only be speculative. To date, we cannot demonstrate the regional extent of these candidate sequence boundaries. Absolute ages within the Entrada Sandstone will eventually clarify sequence stratigraphic correlations.

Escalante Composite Section

Sequence stratigraphy for the Escalante Composite (EC) section was based on changes in depositional facies (figure 7). Within the EC section we have defined three candidate sequences. Each of these is bounded by a candidate sequence boundary (SB) which represents a time of relative sea-level fall. The base of this section is interpreted as the high intertidal facies. The overlying supratidal sabkha facies indicates a relative drop in sea-level. The candidate SB sits at the base of this facies. The supratidal facies is overlain by coarsening upward middle and lower intertidal facies. This represents a relative rise in sea-level. The lower intertidal facies is then overlain by the middle intertidal which represents a relative drop in sea-level or a progradational phase of deposition. Sea-level regresses more dramatically as the middle intertidal is covered by the high intertidal and sabkha facies marking subaerial exposure and the next candidate SB. The uppermost facies are supratidal sabkha and erg-margin deposits. These facies represent the third and final candidate sequence in the Escalante Composite Section.

West Flank San Rafael Swell-South Salt Wash

The West San Rafael Swell (WSRS) section is dominated by middle to high intertidal deposits. Our preliminary interpretation places six candidate sequences within this section. The lowest portion of this section was interpreted as middle intertidal deposits (figure 7). This is

overlain by sabkha deposits, the base of which is the candidate sequence boundary (SB). Sea-level rises again and middle intertidal deposits overlie the sabkha. The system then returns to a sabkha environment representing another drop in sea-level. Another candidate SB is placed at the sabkha facies' lower boundary followed by another sea-level rise. Approximately 25 m above the second candidate sequence boundary there is a significant increase in the mudstone to siltstone ratio. This mudstone-dominated section represents the high intertidal zone and a relative drop in sea-level. Thus, we place another candidate SB at its base. At the top of this mudstone-dominated section there is a relatively thin bed with abundant gypsum nodules that represents the supratidal sabkha and another relative fall in sea-level. This represents the fourth candidate SB in the WSRS section. Relatively sandstone-rich middle intertidal facies lie above the gypsum nodular bed indicating a transgression of the sea bringing middle intertidal deposits above the high intertidal and sabkha facies. A fifth and last candidate SB is placed above the sandstone-rich section. This final candidate SB is overlain by the uppermost portion of the WSRS section which again displays an increase in the mudstone to sandstone ratio. It is comprised of alternating sand-rich, middle intertidal deposits and mudstone-dominated, high intertidal deposits representing a relative fall in sea-level.

East Flank San Rafael Swell

Like the Escalante Composite section, the east flank of the San Rafael Swell also displays three candidate sequences. The basal section was interpreted as the high intertidal facies (figure 7). Overlying this is the middle intertidal facies indicating continued rise in sea-level. We interpret a relatively dramatic change of facies to subtidal ooid shoals and tidal bundles above these deposits. This indicates further transgression of the sea.

Overlying the subtidal deposits is the mudstone-dominated high intertidal facies. This indicates a dramatic relative sea-level fall and thus a candidate sequence boundary (SB) at its base. The next facies to be deposited include the middle and lower intertidal deposits, indicating a relative rise in sea-level. Overlying these deposits is the erg-margin facies indicating a significant relative sea-level fall and the second candidate SB. The rocks overlying this candidate SB comprise the third and final candidate sequence.

DISCUSSION

Differences in Thickness

The measured sections reveal large differences in thickness (figure 7). Thickness tends to increase from the ESRS to the WSRS and thickens even more to the south in the Escalante area. This indicates the depocenter during Entrada Sandstone time was largely in the south near Escalante with less deposition occurring in the north. A reason for this is that the southwest section was closer to the Jurassic Western Cordilleran and the associated foreland trough. As the land subsided, greater accommodation space was created allowing for more deposition of sediment in the areas near the mountain range. The thickness decreases to the north and east where the effects of subsidence would have had a smaller impact. Also, sediment supply may have been more readily available from the west. The ESRS site was being sourced from the east where the large Entrada Sandstone erg existed (Marino and Morris, 1996; Morris and others, 2005).

Depositional Environment

We interpret this region to have been a large, broad, tidal flat with associated subtidal, supratidal sabkha, and supratidal erg-margin zones (figure 7). The deepest water facies (subtidal ooid shoals and bars) is located at the ESRS section (figure 6). This section also displays the

most complete range in facies, spanning the subtidal (ooid shoals and bars) to the supratidal (erg-margin eolian dunes). The greatest accumulation of erg-margin deposits is located to the south near Escalante (figure 4). The WSRS section displays the least range of facies (middle intertidal to supratidal sabkha) (figures 4 and 7). These data suggest that although the southwest and west areas were subsiding most rapidly (see above), sediment supply kept pace and eventually outpaced subsidence. To the northeast, sediment supply was outpaced by subsidence. At one time, subtidal ooid shoals and bars were deposited. We conclude that the rate of sediment supply to the Callovian Jurassic seaway was higher from the west than the east.

Sequence Stratigraphy

Based on changes in major facies packages, we interpret three sequences (possibly third-order) in the Escalante Composite (EC) section, six in the West San Rafael Swell (ESRS) section, and three in the East San Rafael (ESRS) section. We conclude that the three sections, which span a distance of 193 km, reflect different influences of sediment supply and subsidence. This is likely the result of the EC and WSRS sections being closer to the Jurassic Western Cordilleran relative to the ESRS section. Crabaugh and Kocurek (1993) has identified four third-order sequences east of our study area, however the fourth sequence is part of the Curtis and Summerville Formations.

Based on the different number of possible sequences and the vast differences in sediment supply and subsidence, regional sequence stratigraphic correlation does not appear plausible at this time. If an attempt was made, it would be highly tentative until some absolute ages could be obtained from the Entrada Sandstone. Obtaining absolute ages from candidate ash beds is one focus of our ongoing research.

CONCLUSIONS

Thickness variations of the Entrada Sandstone indicate greater subsidence and sediment supply in the southwest part of the study area. This likely indicates its proximity to the Jurassic Western Cordilleran and the developing foreland basin. Although facies range from subtidal ooid shoals to erg-margin sandstones within the study area, the majority of the study area is composed of mudstone-dominated intertidal facies that repeatedly experienced subaerial exposure. A preliminary sequence stratigraphic analysis of each section indicates suggests that the Escalante Composite (EC) section and East San Rafael Swell (ESRS) section each contain three candidate sequences and the West San Rafael Swell (WSRS) section contains six candidate sequences. It is difficult to correlate sequence boundaries due to rapid fluctuations of intertidal facies of the West San Rafael Swell section. The regional extent of each candidate sequence must be proven, which is difficult without an absolute time framework. Future research will attempt to establish this time framework by analyzing and dating candidate ash beds.
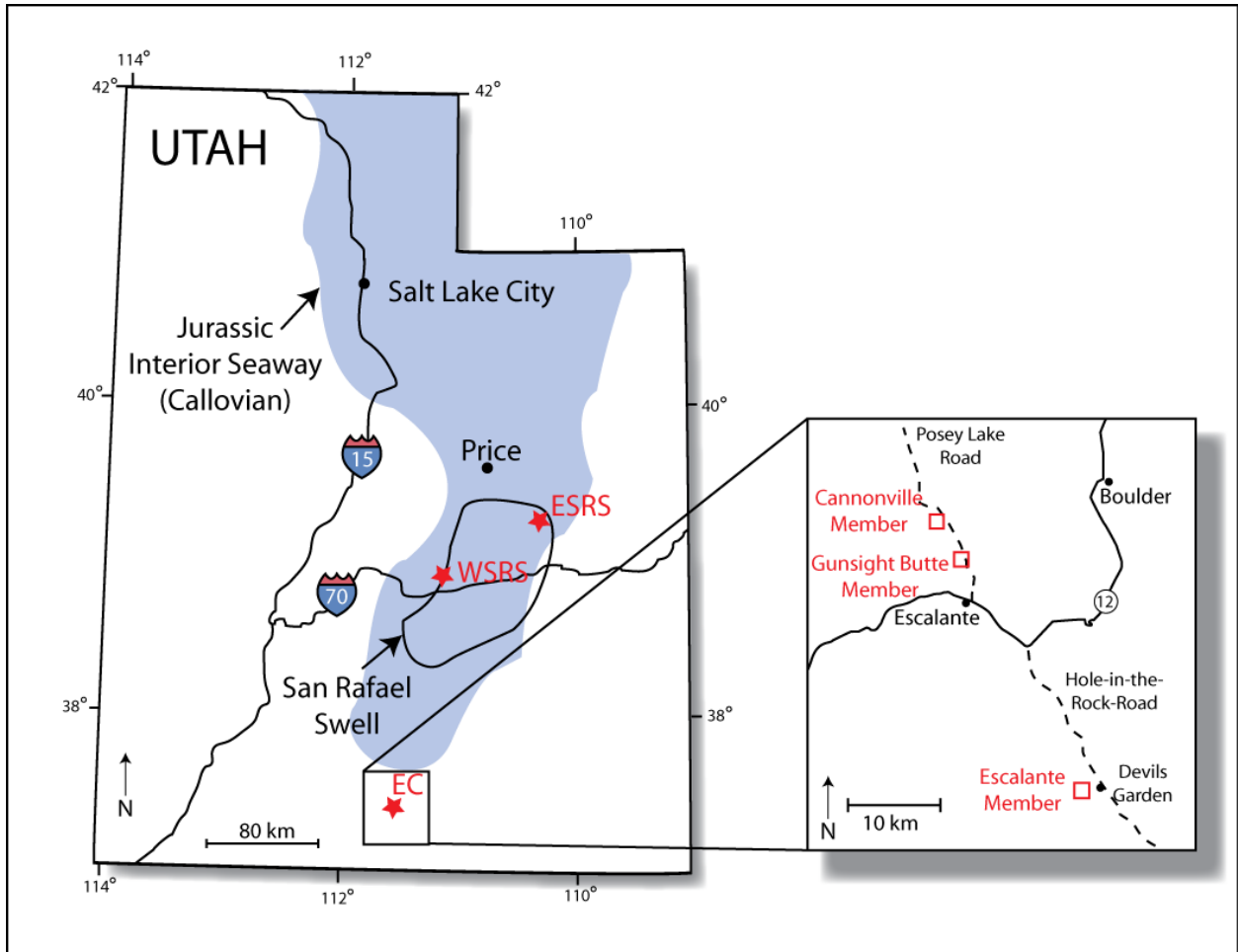
Figure 1: Index map of Utah showing the locations of our measured sections of the Entrada Sandstone including the Escalante Composite (EC), West San Rafael Swell (WSRS), and East San Rafael Swell (ESRS) sections. The inset shows the location of sections used for the EC section. The solid line outlines the present day San Rafael Swell and the dashed line is the approximate extent of the Jurassic Seaway during Callovian time (Perkes, in prep).
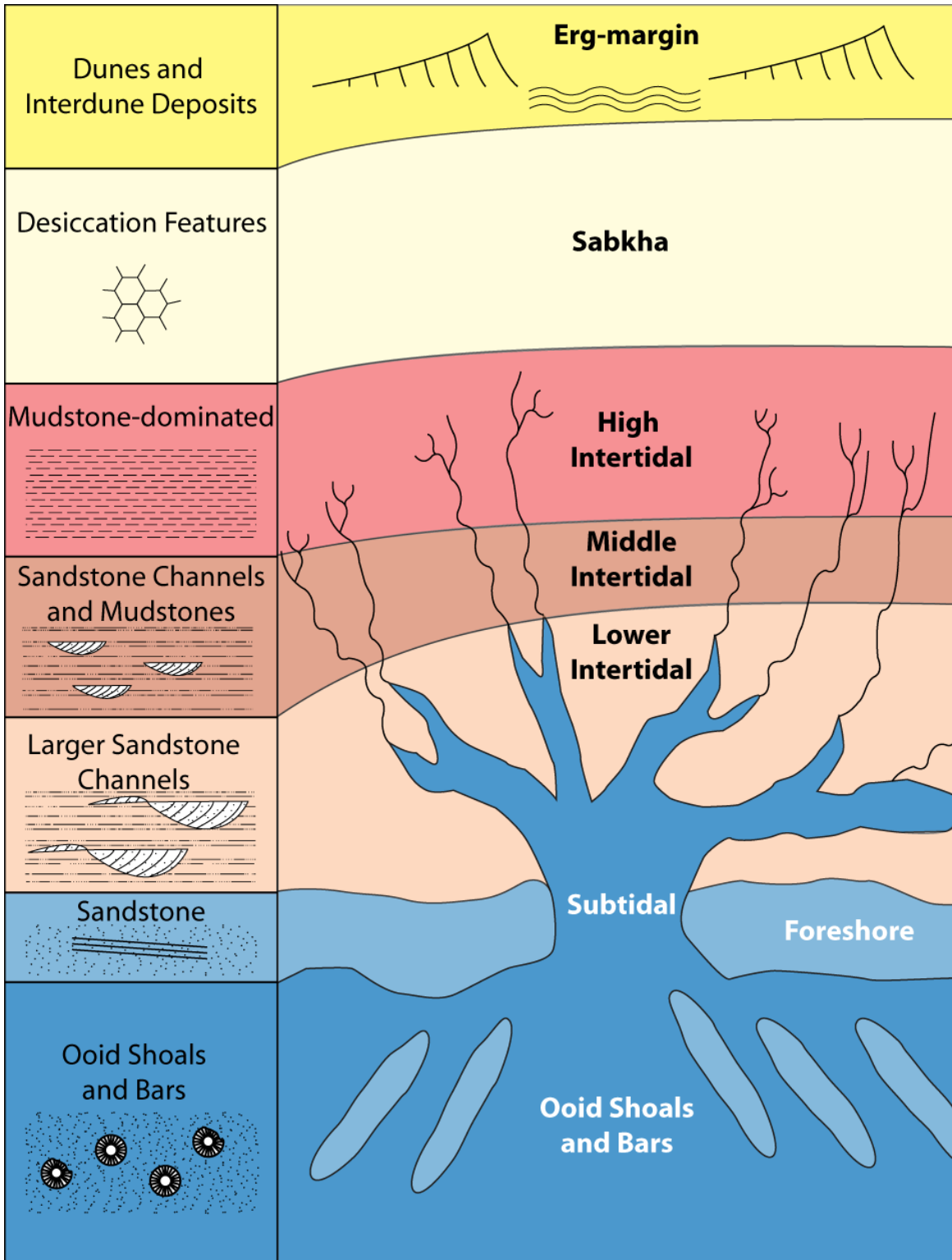
Figure 2: Plan-view of the depositional model used in this study. The model integrates published tidal flat models (Dalrymple 1992; Galloway, 1986, Klein, 1972) and supratidal erg-margin models (Kocurek and Havholm, 1991). Key features of each facies are indicated in the left column.

Ma	Stage	San Rafael Swell Stratigraphy	Escalante Stratigraphy
	KIMMER-IDGIAN	Morrison Fm.	Morrison Fm.
156	OXFORDIAN	J-5	J-5
		Summerville Fm.	Summerville Fm.
		Curtis Fm.	J-3
161		J-3	
	CALLOVIAN	Entrada Ss.	Entrada Ss.
165	BATHONIAN	Carmel Fm.	Carmel Fm.

Figure 3: General stratigraphic relationships of the Entrada Sandstone in the Escalante and San Rafael Swell regions (modifed from Sprinkel 1994, Wilcox 2007, and Perkes, in prep).
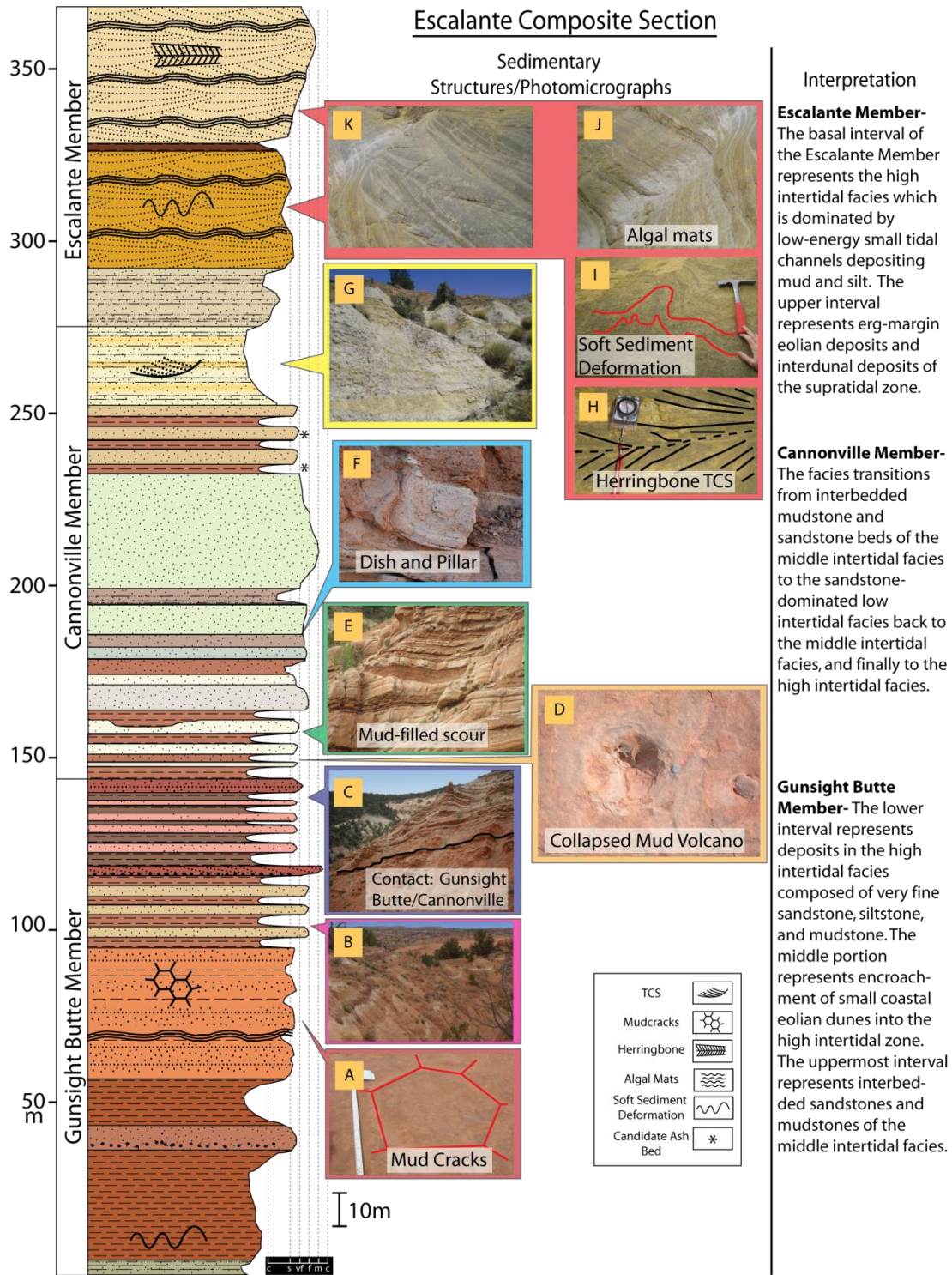
Figure 4: Stratigraphic column (left) of the Escalante Composite (EC) section displaying grain size and geomorphic expression. The two center columns contain photographs taken of the outcrop or key mesoscale bedforms useful in determining the depositional environment and facies. Shaded colors indicate the location of the photographs within the stratigraphic section. The right column contains our interpretations relative to depositional conditions.
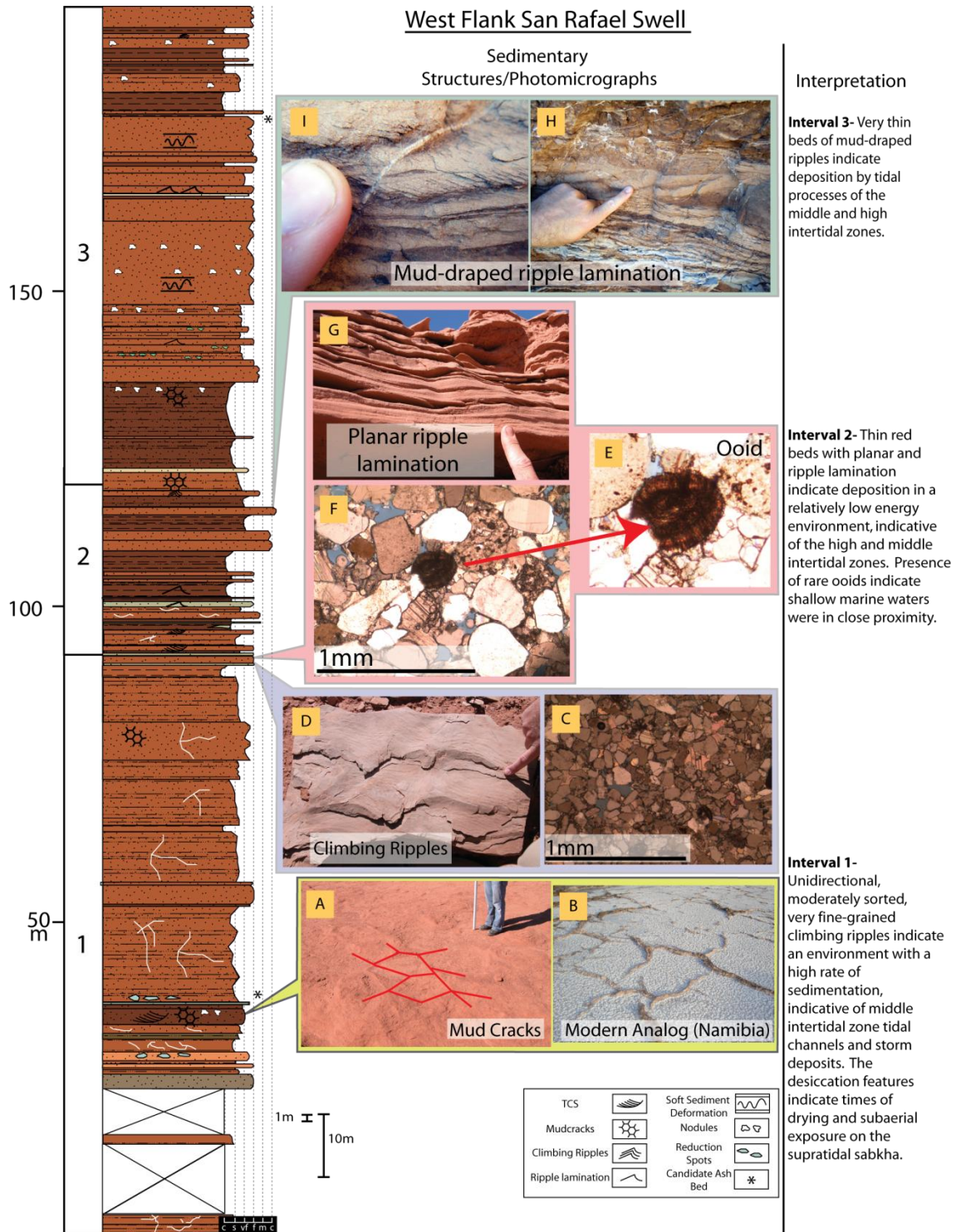
Figure 5: Stratigraphic column (left) of the West Flank of the San Rafael Swell (WSRS) displaying grain size and geomorphic expression. The center column contains photographs taken of the outcrop, key mesoscale bedforms, and photomicrographs of thin sections useful in determining the depositional environment and facies. Shaded colors indicate the location of the photographs within the stratigraphic section. The right column contains our interpretations relative to depositional conditions.
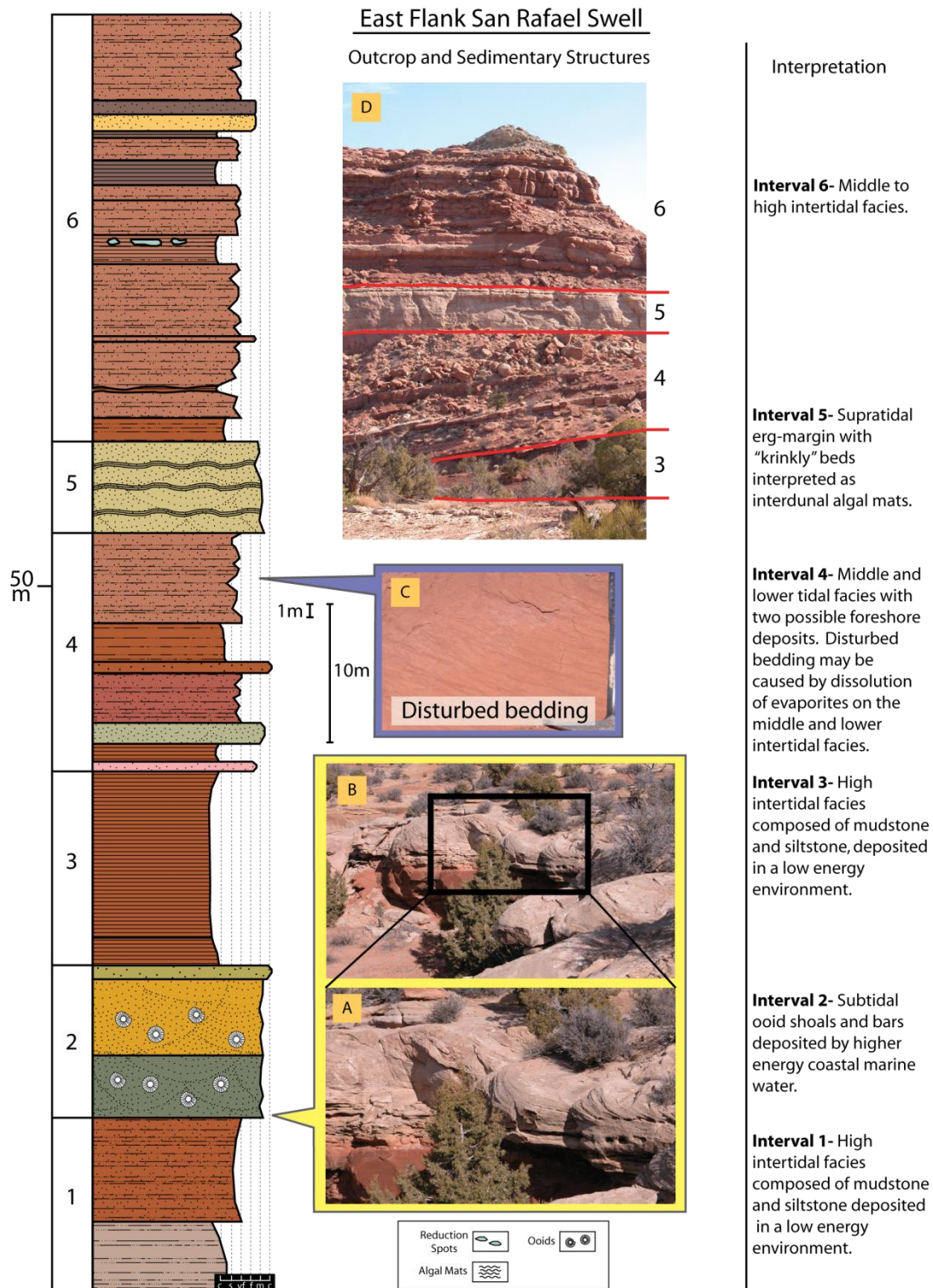
Figure 6: Stratigraphic column (left) of the ESRS displaying grain size and geomorphic expression. The first column contains photographs taken of the outcrop or key mesoscale bedforms useful in determining the depositional environment and facies. Shaded colors indicate the location of the photographs within the stratigraphic section. The third column contains our interpretations relative to depositional conditions.
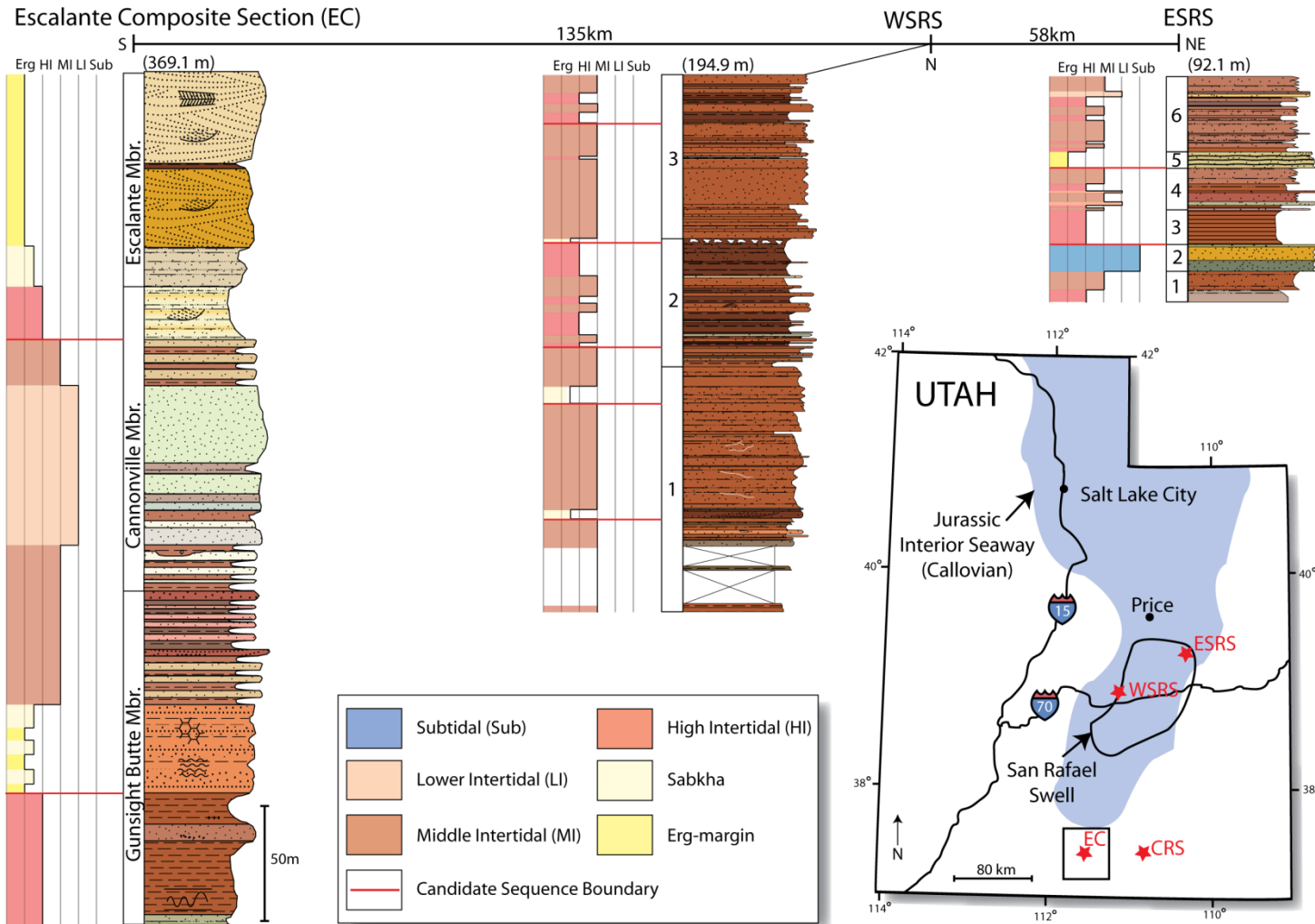
Figure 7: Facies and sequence stratigraphic interpretation for each of the measured sections. The scale bar above the columns shows the relative distance between locations. The stratigraphic columns illustrate geomorphic expression. For ease of discussion we have divided the columns into the respective members (Escalante Composite section) or stratigraphic intervals (e.g. 1, 2, 3, etc…of WSRS and ESRS sections). Note the red lines indicating candidate sequence boundaries.

REFERENCES CITED

Beitler, B., Chan, M.A., and Parry, W.T., 2003, Bleaching of Jurassic Navajo Sandstone on Colorado Plateau Laramide highs-evidence of exhumed hydrocarbon supergiants?: Geology, v. 31, no. 12, p. 1041-1044.

Blakey, R.C., 1989, Triassic and Jurassic geology of the southern Colorado Plateau: Arizona Geological Society Digest, v. 17, p. 369-396.

Blakey, R.C., Peterson, F., Caputo, M.V., Geesaman, R.C., and Voorhees, B.J., 1983, Paleogeography of Middle Jurassic continental, shoreline, and shallow marine sedimentation, southern Utah: Rocky Mountain Paleography Symposium, v. 2, p. 77-100.

Blakey, R.C., and Ranney, W., 2008, Ancient landscapes of the Colorado Plateau: Grand Canyon, Grand Canyon Association, 156 p.

Carr-Crabaugh, M., and Kocurek, G., 1998, Continental sequence stratigraphy of a wet eolian system; a key to relative sea-level change, *in* Shanley, K., and McCabe, P., editors, Relative roles of eustasy, climate, and tectonism in continental rocks: SEPM Special Publications, v. 59, p. 213-228.

Crabaugh, M., and Kocurek, G., 1993, Entrada Sandstone: an example of a wet aeolian system, *in* Pye, K., editor, The dynamics and environmental context of aeolian sedimentary systems: Geological Society of London Special Publication 72, p. 103-126.

Dalrymple, R.W., Zaitlin, B.A., and Boyd, R., 1992, Estuarine facies models: Conceptual basis and stratigraphic implications: Journal of Sedimentary Petrology, v. 62, p. 1130-1146.

Dickinson, W.R., and Gehrels, G.E., 2003, U-Pb ages of detrital zircons from Permian and Jurassic eolian sandstones of the Colorado Plateau, USA: Paleogeographic implications: Sedimentary Geology, v. 163, p. 29-66.

Doelling, H.H., Blackett, R.E., Hamblin, A.H., Powell, J.D., and Pollock, G.L., 2000, Geology of Grand Staircase-Escalante National Monument, Utah: Utah Geological Association, Publication 28, p. 189-231.

Eckels, M.T., Suek, D.H., and Harrison, P.J., 2005, New, old plays in southern Uinta basin get fresh look with 3D seismic technology: Oil & Gas Journal, v. 103, p. 32-40.

Galloway, W.E., 1986, Reservoir facies architecture of microtidal barrier systems: The American Association of Petroleum Geologists Bulletin, v. 70, no. 7, p. 787-808.

Hintze, L.F., and Kowallis, B.J., 2009, Geologic history of Utah: Brigham Young University Geology Studies, Special Publication 9, 225 p.

Keach, R.W., Morris, T.H., McBride, J.H., Mullen, M., Leetaru, H.E., and O'Neal, R., 2006, Interpretations of the Jurassic Entrada Sandstone play using 3D seismic attribute analysis, Uinta Basin, Utah: Utah Geological Survey, Open File Report 493, 22 p.

Klein, G.D., 1972, Determination of paleotidal range in clastic sedimentary rocks: Twenty-fourth (XXIV) International Geological Congress, v. 6, p. 397-405.

Kocurek, G., 1981, Significance of interdune deposits and bounding surfaces in aeolian dune sands: Sedimentology, v. 28, p.753-780.

Kocurek, G., and Dott, R.H., Jr., 1983, Jurassic paleogeography and paleoclimate of the central and southern Rocky Mountains Region: Rocky Mountain Paleography Symposium, p. 101-116.

Kocurek, G. and Havholm, K.G., 1991, Eolian event stratigraphy; a conceptual framework: American Association of Petroleum Geologists Bulletin, v. 75 (3), p. 612.

Kocurek, G., and Hunter, R.E., 1986, Origin of polygonal fractures in sand, uppermost Navajo and Page Sandstones, Page, Arizona, Journal of Sedimentary Petrology, v. 56, no. 6, p. 895-904.

Marino, J.E., 1992, Erg margin and marginal marine facies analysis of the Entrada Sandstone, San Rafael Swell, Utah: Implications to hydrocarbon entrapment: Provo, Brigham Young University, M.S. thesis, 140 p.

Marino, J.E., and Morris, T.H., 1996, Erg margin and marginal marine facies analysis of the Entrada Sandstone, Utah: Implications to depositional models and hydrocarbon entrapment, *in* Morales, M., editor, The continental Jurassic: Museum of Northern Arizona, Bulletin 60, p. 483-496.

Monn, W.D., 2006, A multidisciplinary approach to reservoir characterization of the coastal Entrada erg-margin gas play: Provo, Brigham Young University, M.S. thesis, 33 p.

Morris, T.H., McBride, J.H., and Monn, W.D., 2005, A multidisciplinary approach to reservoir characteristics of the coastal Entrada erg-margin gas play, Utah: Utah Geological Survey, Open File Report 459, 50p.

Perkes, T., in prep, Integrating facies analysis, terrestrial sequence stratigraphy, and the first detrital zircon (U-Pb) ages of the Twist Gulch Formation, Utah, USA: Constraining paleogeography and chronostratigraphy: Provo, Brigham Young University, unpublished M.S. thesis.

Smith, L.S., 1976, Paleoenvironments of the Upper Entrada Sandstone and the Curtis Formation on the west flank of the San Rafael Swell, Emery County, Utah: Brigham Young University Geology Studies, v. 23, p. 113-171.

Sprinkel, D.A., 1994, Stratigraphic and time-stratigraphic cross sections: A north-south transect from near the Uinta Mountain axis across the Basin and Range transition zone to the western margin of the San Rafael Swell: U.S. Geological Survey, Miscellaneous Investigations Series, I-2184-D.

Tanner, W.F., 1965, Upper Jurassic Paleogeography of the Four Corners Region: Journal of Sedimentary Petrology, v. 35, p. 564-574.

Wilcox, W.T., 2007, Depositional age and sequence stratigraphy of the Jurassic Curtis, Summerville, and Stump Formations, Utah and Colorado: Oxford, University of Miami, unpublished M.S. thesis.

Chapter Two

Facies Analysis and Reservoir Characterization of the Mudstone-rich Portion of the Entrada
Sandstone, South-central Utah: Emphasis on the Bitter Seep Wash Sandstone at
South Salt Wash and Bitter Seep Wash

ABSTRACT

Three reservoir-quality sandstone facies are present in the understudied mudstone-rich

portion of the late Middle Jurassic (Callovian) Entrada Sandstone, San Rafael Swell, Utah.

Deposition of the muddy Entrada Sandstone is interpreted to be found in three distinct zones: the

subtidal, the intertidal, and the supratidal. The subtidal zone includes the ooid-bearing shoal and

bar facies. The intertidal zone includes the lower, middle, and high intertidal facies, including a

storm facies. The supratidal zone comprises the sabkha, eolian-filled supratidal sabkha pond,

and erg-margin eolian facies. We incorporate these eight facies into a working depositional

model and propose a modern analogue from the north end of the Gulf of California. Porosity and

permeability analysis indicates excellent reservoir potential in three of these facies: the lower

intertidal channel facies, the eolian-filled supratidal sabkha pond facies, and the supratidal erg-

margin eolian facies. Porosities in these facies range from approximately 11-22% while

permeabilities range from approximately 44-430md. During facies migration these high-quality

reservoir facies are enveloped by mostly muddy, low-quality reservoir facies that may act as

seals to subsurface fluid flow, potentially creating stratigraphic and combination hydrocarbon

traps. Porosities of sealing facies range from approximately 4-11% with permeabilities ranging

from approximately 0.05-1.65md. Porosity-permeability cross plots indicate succinct fields that

separate these facies. We conclude that within the mudstone-rich portion of the Entrada

Sandstone system, an accurate depositional facies model must be integrated with reservoir

characteristics of the respective facies in order to develop predictive strategies for subsurface hydrocarbon exploration.

<center>INTRODUCTION</center>

Geographic Location

Reservoir characteristics of facies within and adjacent to the mudstone-rich Entrada Sandstone of south-central Utah have been marginally studied (see Morris and others, 2005 for review). To better understand these reservoir characteristics, facies within the Entrada Sandstone on the west and east flanks of the San Rafael Swell are examined (figure 1). In the course of this study a sandstone stratigraphically located in the upper 1/3 of the Entrada Sandstone was identified approximately 5km (3.1mi) south of the WSRS measured section. We named this sandstone the Bitter Seep Wash Sandstone (BSWS) after the location where it was discovered (figure 1). This sandstone is a major focus of this study because it provides insights to the economic potential of the Entrada Sandstone as well as its depositional history and paleogeography.

Core plugs were extracted from two outcrop locations: the western San Rafael Swell (WSRS) section on the interpreted western margin of the Callovian phase of the Jurassic seaway, and the eastern San Rafael Swell (ESRS) section located along the interpreted eastern margin of the Jurassic seaway (Hicks and others, 2010). The WSRS section is located adjacent to South Salt Wash along the Moore Road cutoff, approximately 24km southeast of Ferron, Utah within the Short Canyon 7.5 minute quadrangle (figure 1). The ESRS section is located approximately 13km (8.1mi) west-southwest of Woodside, Utah adjacent to Summerville Wash within the Dry Mesa 7.5 minute quadrangle. The BSWS is located approximately 17km (10.6mi) southeast of

Emery, Utah along South Salt Wash and Bitter Seep Wash in the northern end of the Big Bend Draw 7.5 minute quadrangle.

The Entrada Sandstone is well exposed within the San Rafael Swell (SRS) and in specific locales to the south. The SRS study area exhibits the classic mudstone-rich facies that have been interpreted as marine tidal flat, sabkha, and supratidal deposits (Smith, 1976; Marino, 1992; Marino and Morris, 1996; and Hicks and others, 2010). The ESRS section contains a complete range of facies from the subtidal ooid-bearing shoal and bar facies to supratidal erg-margin facies (Hicks and others, 2010). The WSRS section is dominated by middle intertidal to sabkha facies deposits. The BSWS, which is enveloped within mudstone-rich facies, crops out approximately 5km (3mi) south-southwest of the WSRS section. This sandstone has not been studied previously and is poorly defined relative to depositional process. Particular focus was placed on the BSWS in an effort to understand the depositional facies, place the facies within the context of a depositional model, and understand its reservoir potential.

Geologic History

The Entrada Sandstone was deposited during late Middle Jurassic (Callovian) time, approximately 161.2 to164.7 Ma (Sprinkel, 1994; Dickinson and Gehrels, 2009; Hintze and Kowallis, 2009; Perkes and Morris, in press). Before the Entrada Sandstone was deposited, much of central Utah was covered by a shallow seaway that waxed and waned during Bajocian and Bathonian time. Within this seaway, referred to as the Sundance or Carmel Sea, much of the Carmel and Twin Creek Formations and, at its latest phase, the Arapien Shale were deposited (Kocurek and Dott, 1983; Sprinkel, 1994; Blakey and Ranney, 2008; Hintze and Kowallis, 2009). During Bathonian time, coastal dune fields existed along the southern margin of this seaway and occasionally prograded over its broad tidal flats (Tanner, 1965; Kocurek and Dott,

41

1983). The Callovian phase of this seaway has been referred to as the Western Jurassic Interior

Seaway (not a precursor to the Western Cretaceous Interior Seaway) by Wilcox and Currie

(2008) and by Perkes and Morris (in press) and the Utah-Idaho Trough by Peterson and Smith

(1986) and Riggs and Blakey (1993). It is herein called the Jurassic seaway. As the sea

continued to fluctuate through Callovian time, restricted marine and tidal flat environments

formed within central Utah, creating thick, mud-rich tidal flat (Smith, 1976) and sabkha deposits

(Blakey and others, 1983; Blakey 1989). The southward narrowing of this seaway may have

accentuated tidal influences. Alluvial and tidally-influenced shoreline deposits dominated the

western and central areas of the seaway. Coastal dune deposits (erg-margin) developed along the

southern and eastern margins of the seaway, respectively located near Escalante, UT and

Woodside, UT, where they interfingered with tidally-influenced shoreline and sabkha deposits

(Kocurek and Dott, 1983; Blakey, 1989; Marino and Morris, 1996; Carr-Crabaugh and Kocurek,

1998; Morris and others, 2005). Entrada Sandstone erg deposits are thickest and most extensive

in eastern Utah and constitute the Slickrock Member of the Entrada Sandstone in Arches

National Park and in the Moab, Utah area (Kocurek and Dott, 1983).

The J-3 unconformity is a regional uncomformity within the Colorado Plateau that

overlies the Entrada Sandstone throughout southern, eastern, and central Utah (Pipiringos and

O'Sullivan, 1978). The unconformity is overlain by the Curtis Formation and locally by the

Summerville Formation, which were also deposited in a marine foreland basin (Smith, 1976;

Sprinkel, 1994; Hintze and Kowallis, 2009; Wilcox and Currie, 2008; Perkes and Morris, in

press). The contact between the Entrada Sandstone and the Curtis Formation is largely

disconformable although locally it can be an angular unconformity (Keach and others, 2006).

During deposition of the Curtis Formation the Jurassic Cordillera foreland trough narrowed, and the axis migrated east and north (Blakey and Ranney, 2008; Perkes and Morris, in press).

Purpose

The transitions between mudstone-rich, marine-influenced facies, and sandstone-dominated erg-margin facies of the Entrada Sandstone have been recognized as potential stratigraphic and combination traps for hydrocarbons (Marino and Morris, 1996; Morris and others, 2005; Keach and others, 2006). Based on these transitions, hydrocarbons have been produced from the Entrada Sandstone within the Uinta basin (Eckels and others, 2005). Further potential exists for development of this play in south-central Utah where sandstone beds and mudstone beds interfinger in the subsurface. Hydrocarbon charging can occur where the Entrada Sandstone is overlain by, and subjacent to Cretaceous rocks, which have proven to be a potential source for hydrocarbons. The Entrada Sandstone is bleached in numerous locales in south-central Utah, indicating a history of subsurface fluid movement, possibly hydrocarbons (Marino and Morris, 1996; Beitler and others, 2003). Although the greatest known potential for stratigraphic traps is in areas where mudstone-rich facies transition into the erg-margin and erg-facies to the east and south of the Jurassic seaway, other reservoir-quality facies also exist.

METHODS

Analysis of the Bitter Seep Wash Sandstone

Isopach – Fifty-five thickness measurements of the Bitter Seep Wash Sandstone (BSWS), located in South Salt Wash and Bitter Seep Wash provide data on its geometry. These measurements were recorded at approximately 100m (328ft) intervals at every reachable exposure of the BSWS. Measurements were made with a measuring tape and the location was recorded on a GPS device for accurate mapping. These locations were loaded into ArcMap and

projected onto an aerial photograph. A hand contoured isopach map (at 1 m (3.3 ft) intervals) was then prepared.

Paleocurrent Analysis **-** To better understand the depositional environment of the BSWS, 67 paleocurrent measurements were recorded using a Suunto compass. Where possible, foreset surfaces were used, but the majority of measurements were taken from the plan-view exposed surface of the sandstone by measuring the azimuth perpendicular to visible foresets and reactivation surfaces.

Grain-size Analysis **-** Two large samples were collected from thick and thin parts of the sandstone, respectively. Both samples were very friable and were easily prepared for grain-size analysis. Each sample was disaggregated and then shaken through nine sieves (using a RoTap device) at half phi units, ranging from 0 to 4Φ, in order to produce the data needed for statistical approaches including histograms and cumulative frequency curves. The graphic mean, mode, standard deviation (sorting), skewness and kurtosis were calculated from these curves.

Porosity & Permeability Analysis **-** To obtain porosity and permeability data of the BSWS, 21 core plugs were extracted from four different locations within the Bitter Seep Wash area (figure 2). At each location, core plugs were taken near the base of the sandstone and at 0.5m (1.6ft) intervals vertically through the sandstone. In many areas, plugs were unobtainable because of the friability of the sandstone. For the most accurate porosity and permeability analysis, each core plug was trimmed into cylinders 2.54cm (1in.) in diameter, and 5.08cm (2in.) in length. After being trimmed and dried, their weight was recorded. The length and diameter were then measured with calipers; the length was measured twice and the diameter was measured five times down the length of the core plug. These procedures follow the newly developed lab manual for the Temco/CLI Ultrapore 300 and Ultra Perm 500 in the BYU Sedimentology

44

Laboratory. The porosity and permeability data were recorded on a crossplot to delineate the reservoir potential of the various facies. The friable nature of the sandstone permitted sampling only in isolated areas, therefore a porosity fence-diagram was not produced.

Next, each core plug was measured in the permeameter at five different confining pressures: 500, 1000, 1500, 2000, and 2500 psi. The purpose for this was to see if there would be a change in permeability with increased confining pressure. According to Selley (1998) the relationship between lithostatic pressure and depth is approximately 1psi/ft. Many hydrocarbon reservoirs are below 762m (2500ft.) equivalent to 2500 psi; however, both the permeameter and rock integrity was limited to 2500 psi.

Facies Identification

Hicks and others (2010) interpreted six Entrada facies on the east and west flanks of the San Rafael Swell (figure F1). Using their facies interpretations and discovering two more facies (storm, and eolian-filled supratidal sabkha pond facies) we determined locations to collect core plugs.

Data for these facies were collected from both the west San Rafael Swell (WSRS) section and east San Rafael Swell (ESRS) section (figure 1). The sabkha, high intertidal, middle intertidal, and storm facies' data were collected at the WSRS section. The erg-margin, lower intertidal channel, and ooid-bearing shoal and bar facies' data were collected at the ESRS section.

Porosity and Permeability - Concurrent with the porosity and permeability analysis of the BSWS, 44 core plugs were also extracted from six other facies. At each core plug extraction location an attempt was made to extract 10 core plugs over a distance of 2m (6.6ft) along the specific bed. Each of these core plugs was processed and analyzed in the porosimeter and

permeameter by the same methods as those from the BSWS. The porosity and permeability of all core plugs, including the BSWS, were then graphed on a porosity vs. permeability cross plot.

Petrographic and Petrologic Analysis **-** To properly classify and understand the provenance of each facies it was necessary to perform petrographic and petrologic analyses. Fourteen thin sections were made from samples representing the subtidal ooid-bearing shoal and bar, lower intertidal channel, middle intertidal, storm, sabkha, erg-margin facies, and the BSWS. The high-intertidal facies, which is the most mudstone-rich facies, was difficult to sample, has little reservoir potential, and was not analyzed. Two thin sections were made from each facies: one from the core plug with the highest porosity and one from the core plug with the lowest porosity. Each core plug was injected with blue epoxy to highlight porosity and stained red for plagioclase and yellow for feldspar. A 300-point count was completed for each thin section. We also noted textural features, textural maturity, relative compositional maturity, cement types, and any diagenetic alteration. The data were then plotted on QFL (quartz, feldspar, and lithics), QmFLt (monocrystalline quartz, feldspar, and lithics), and QmPK (monocrystalline quartz, plagioclase, and potassium feldspar) ternary diagrams (Dickinson and Suczek, 1979: and Dott, 1964) to determine the proper classification and delineate the tectonic provenance. These data as well as the definition of each tectonic provenance are presented in Appendix A.

<div align="center">FACIES</div>

Below is a summary of facies previously studied by Hicks and others (2010). After publication of that study, we completed more field work and lab analyses, which provided more data on each facies. This included the discovery of two more facies not discussed in Hicks and others (2010).

The purpose of this section is to provide brief field and petrologic descriptions as well as an interpretation of each facies. Facies 5 (storm) and the Bitter Seep Wash Sandstone (BSWS) (discussed in detail below), are the newly discovered facies, while facies 1 (erg-margin), 2 (sabkha), 3 (high-intertidal), 4 (middle-intertidal), facies 6 (lower-intertidal channel), and 7 (subtidal ooid-bearing shoal and bar) were discussed in Hicks and others (2010). All facies with the exception of eolian-filled supratidal pond facies interpreted from the BSWS (see details below) are summarized in Table 1.

Facies 1 (Erg-Margin Eolian Sandstone Facies)

Data - Facies one is a white to light gray, fine-grained, moderately to well-sorted, sub-rounded to rounded feldspathic arenite with carbonate cement. This facies displays relatively large high- to low-angle trough cross stratification (TCS) with relatively abundant reactivation surfaces (figures 3 and 4). It is interbedded with centimeter-scale wavy laminated beds ranging from very thin to thick (figure 3). This facies locally contains apparent multi-directional TCS and soft-sediment deformation (figure 5).

In thin section, monocrystalline quartz is found to be the dominant framework grain (48.3-53%) with smaller amounts of coarse polycrystalline quartz (4.7-5.7%), plagioclase (3.7-5.7%), and K-feldspar (6%) (figures 3, A3, and A4). Grain contacts are point and long contacts. There are rare concavo-convex contacts. This facies has interparticle porosity ranging from 14-17.7%. Rare echinoderm fragments were also present.

Interpretation - This facies is interpreted as the erg-margin eolian sandstone facies deposited in a relatively wet environment proximal to the Jurassic seaway. The high and low-angle TCS and reactivation surfaces are very typical of eolian sandstone deposits. The wavy laminated beds are interpreted to be algal mats formed in moist sand flats between dunes. Soft

sediment deformation is also indicative of a relatively wet environment. Rare multi-directional

TCS indicate times when the prevailing wind changed directions. Echinoderm fragments are

interpreted to have blown into the dune field from the nearby shoreline. All of these

characteristics are indicative of a relatively wet eolian environment near the edge of the Jurassic

seaway.

Several authors have studied the Entrada Sandstone and shared similar observations and

interpretations (Kocurek, 1981b; Kocurek and Havholm, 1991; Carr-Crabaugh and Kocurek,

1998; Dickinson and Gehrels, 2003; Morris and others, 2005; Monn, 2006).

QFL percentages indicate the tectonic provenance to be the continental block provenance.

Point and long grain contacts with rare concavo-convex contacts indicate moderate burial

depths.

Facies 2 (Sabkha Facies)

Data - Facies two is characterized by light and dark reddish brown, silt-sized,

moderately-sorted, sub-angular, feldspathic siltstone with carbonate cement. Typical features

include disturbed bedding, gypsum nodules, and large (1m scale) desiccation features (figures 6

and 7).

The dominant framework grain is monocrystalline quartz (32.7-39%), with smaller

amounts of coarse polycrystalline (3-12%) and undulose quartz (4-11%) (figures 6, A5, and A6).

Grain contacts are point and long contacts. Laminae-scale (approx. 1cm) bands of matrix are

present as well as many gypsum nodules. Gypsum does not occupy interparticle pore space.

Interpretation - This facies is interpreted to represent supratidal sabkha deposition. Key

features include disrupted bedding caused by dissolution of precipitated salts, the presence of

gypsum nodules, and the formation of polygonal desiccation features at the surface. All of these

features indicate subaerial exposure, evaporative pumping, and precipitation of evaporitic minerals within the sediment, all of which are common in sabkha environments (Thompson and Meadows, 1997).

QFL percentages indicate the tectonic provenance to be the continental block provenance. Point and long contacts indicate relatively shallow burial depths.

Facies 3 (High Intertidal Facies)

Data - Facies three is comprised of reddish brown, siltstone to very fine-grained mudstone with carbonate cement. It is the most thinly laminated and muddiest of the facies. Thin sandstone horizons (approx. 1-3cm) with small ripple laminations are occasionally interbedded with the mudstone (figure 8). These mudstone beds are thin (approx. 5cm), flat bottomed (i.e., little scour), and laterally extensive. They routinely display cross-cutting "stringers" or veins of gypsum which do not occupy interparticle porosity.

This facies is very poorly exposed. Sedimentary features were difficult to observe. Plan-view features were not observed at all. Plugs could not be extracted from this facies due to its mud content.

Interpretations - This facies is interpreted as the high intertidal facies. It is the most mudstone-rich of all the facies, indicating a low energy depositional environment. As the tidal waters moved landward onto the broad tidal flat, water energy dissipated and slack-water conditions existed. During this time, hydraulically light materials (mud- and silt-sized sediment) settled from suspension. The gypsum veins are interpreted to be filled fractures of secondary origin.

Clifton (1983) described the intertidal environment as having thin, regular alternations of clay, silt, and fine sand. Yeo and Risk (1981) also described the upper mudflat facies as being thinly laminated and very muddy.

Facies 4 (Middle Intertidal Facies)

Data - Facies four is a light reddish-brown, poorly sorted, angular- to subangular grained feldspathic siltstone with some very fine-grained sand grains. The grains are cemented by carbonate cement. Matrix is also present in some areas. Three identifying features of this facies are highly disturbed bedding (figures 9 and 10), cross-cutting gypsum stringers (which do not occupy interparticle porosity) (figure 10), and weathering into hoodoos.

Monocrystalline quartz is the dominant framework grain (28.7-30.7%) with smaller amounts of coarse polycrystalline quartz (6.3-11%), plagioclase (8.3-10.7%), and K-feldspar (6.3-11.3%) (figures 9B, A7, and A8). Grain contacts are predominantly point and long contacts. Disturbed bedding is observed in thin section as mm to 1cm-scale bands of matrix.

Interpretation - This facies is interpreted to represent the middle intertidal facies. This facies, as well as facies 2 (sabkha), both display disturbed bedding and gypsum. The sabkha facies tends to have more nodules, whereas the middle intertidal facies has more secondary gypsum stringers. This suggests that these facies routinely experienced subaerial exposure and evaporative pumping. It seems these processes were important to the deposition of the middle intertidal and landward facies. Figure 11 illustrates the flat nature of the sabkha and middle intertidal facies.

Yeo and Risk (1981) describe a lower mudflat facies (herein the middle intertidal facies) which fines upward to the upper mudflat (herein the high intertidal facies).

QFL data indicate the tectonic provenance to be the continental block provenance. Point and long contacts indicate a relatively shallow burial depth.

Facies 5 (Storm Facies)

Data - Facies five is light gray to reddish, medium to fine-grained, poorly-sorted, sub-angular to sub-rounded feldspathic arenite with carbonate cement (which is poikilotropic in some areas). The most prominent bedforms are planar bedding (figure 12) and hummocky cross stratification (HCS) (figure 13A). Both are visible in outcrop, but typically one bedform or the other dominates in a given area. Rip-up clasts are also visible near the basal contact of this facies (figure 13B). These deposits typically display a sharp, undulatory, basal contact with the underlying muddy high intertidal facies (figure 14).

Monocrystalline quartz is the dominant framework grain (33.7-44%) within this facies (figures 12, A9, and A10). There is some K-feldspar (5.7-16.3%), and plagioclase is rarely present (1.7-2%). Up to 27% of this sandstone is composed of calcite cement. Some of this cement may have resulted from calcite replacement of detrital matrix. Grain contacts are predominantly long with some point, but concavo-convex contacts are also present.

Interpretation - This facies is interpreted to represent storm deposits, somewhat similar to a washover fan. HCS formed as large waves associated with the storm surge moved landward. Small TCS lenses were observed locally that cross-cut the HCS. These sets likely represent basinward backflow from storm surge waters. In some instances the sand was deposited as a sheet wash from storm surge. This resulted in very low angle to planar lamination.

Schwartz (1982) observed very low-angle planar strata near the outer edges of washover fans.

QFL data indicate the tectonic provenance to be the continental block and recycled orogeny provenances. Long, point, and concavo-convex grain contacts indicate a moderate burial depth.

Facies 6 (Lower Intertidal Channel Facies)

<u>Data</u> - Facies six is characterized by light grayish red, fine-grained (with rare medium grains), well to moderately-sorted, sub-rounded feldspathic arenite with carbonate cement and echinoderm grains. Bedforms include sets of TCS that scour into each other at approximately a 1 m scale. Possible herringbone stratification was also observed (figure 15). This facies consists of individual medium beds. Laterally, the bed may thin and thicken slightly. Basal contacts are slightly scoured.

The dominant framework grain is monocrystalline quartz (39.3-42.7%) with a moderate amount of plagioclase (6-8.7%) and K-feldspar (6.3-7.7%) (figures 15, A11, and A12). . Echinoderm fragments are present within the deposits. Grain contacts are mainly point and long, and there are some concavo-convex contacts.

<u>Interpretation</u> - This facies is interpreted to represent the lower intertidal channel facies. The presence of TCS and small scours supports this interpretation. Flow velocities were high enough in this environment to scour underlying deposits. Using Southard and Boguchwal's (1990) mean flow velocity vs. median grain size graph, the flow velocities in these channels could have ranged from 0.3 to just under 0.6 m/s. Echinoderms were likely carried landward into the channels by tidal currents.

In describing intertidal channels, Fenies and Faugeres (1998) state that the channels are typically filled with well sorted medium sand and contain TCS. Reinson and others (1988) also

describe tidal channel lithology to be fine- to medium-grained sandstone, with planar and trough cross-stratified beds.

QFL data indicate the tectonic provenance to be the continental block provenance. It was buried deep enough that concavo-convex contacts were beginning to form, but point and long contacts dominate this facies.

Facies 7 (Subtidal Ooid-Bearing Shoal and Bar Facies)

Data - Facies seven is a light yellow to greenish, medium-grained, well-sorted, rounded quartz arenite with carbonate cement. The most prominent bedform in this facies is low to high-angle TCS that is up to 1m in height (figure 16).

Monocrystalline quartz is the dominant framework grain (42.3-43.7%) in this facies (figures 16, A13, and A14). Grain contacts are point and long contacts. Calcitic radial ooids (10.3-13.7%) which nucleated around quartz grain are also visible. Rare echinoderm fragments (5-10%) also make this facies distinct.

Interpretation - This facies is interpreted as the subtidal ooid-bearing shoal and bar facies. Bedforms of this scale suggest flow velocities of 0.6 to 0.8 m/s, typical of subtidally influenced flows similar to those observed at Joulter's Cay on the north end of Andros Island, Bahamas (Harris, 1977). The ESRS section must have been located in a high-energy nearshore area which mixed ooids (possibly from a more basinward location) with siliciclastics of the intertidal zone. The calcitic radial ooids indicate deposition in a low-energy environment within a calcite sea (Tucker and Wright, 1990).

Boersma (1969) describes low-angle trough cross stratification in his study of the Westerschelde Estuary in the Netherlands. He explained that low-angle TCS forms a thick bed

near the base of the shoal. Marino (1992) studied these same deposits and identified them as shoals and bars containing ooids.

QFL data indicate the tectonic provenance to be the continental block and recycled orogeny provenances. Point and long contacts and lack of concavo-convex or sutured contacts indicate a relative shallow burial.

Table 1 is a summary of all the key features representing each of the seven facies discussed above.

FACIES ANALYSIS OF THE BITTER SEEP WASH SANDSTONE

Data and Observations

Field Observations **-** The Bitter Seep Wash Sandstone (BSWS) on the west flank of the San Rafael Swell in the Bitter Seep Wash area (figure 2) offers approximately 200,000m^2 (239,000yd^2) of plan-view exposures, as well as approximately 11 km (6.8miles) of outcrop. The area in which the sandstone is presently exposed is approximately 5.9km^2 (2.3mi^2), but the sandstone undoubtedly existed east of present exposures and continues westward into the subsurface. The excellent exposures allow for optimal paleocurrent analysis in two- and three-dimensional views, as well as many outcrops for thickness measurements, photomosaics, and core plug extractions (although core plugs were limited due to the friable nature of the sandstone) (figures 17 & 18). The BSWS has a maximum thickness of 6.4m (21ft) and pinches out to the north and thins to the southwest. It is not present at the WSRS measured section (Appendix F). It is composed of fine to coarse-grained quartz sand and the sandstone displays a single high-angle trough cross set (TCS) (i.e., the bed represents the advance of a single dune). At all locations, the TCS foresets extend from its basal surface to its upper surface (figures 19 and 20). The upper surface of the sandstone is relatively flat and bounded by silty sandstone

beds which weather into hoodoos (middle intertidal deposits). The exposed upper surface also shows many foresets and reactivation surfaces (figure 21). Asymmetrical ripples were found in one location on this upper surface. The base of the sandstone is relatively flat and bounded by mudstones. Although rare, the base shows signs of soft sediment deformation where sandstone blocks sank into the mudstone below (figure 22).

Paleocurrent Data - After plotting 67 paleocurrent measurements on a rose-plot, the prevailing current direction was found to be southward (figure 23).

Grain Size Analysis - Grain size analyses were completed on samples from thick and thin parts of the BSWS. These analyses showed very small-scale bimodal distribution and a tendency to be finely skewed (figures 24, 25, and 26).

Graphical statistical parameters (tables 2 & 3) were calculated using methods from Folk and Ward (1957). The graphical mean was found to be 1.53Φ (lower medium sand) for the thick sandstone sample and 1.21Φ (upper medium sand) for the thin sandstone sample (table 3). The graphic standard deviation for the thick sandstone sample was 0.77 and the thin sandstone sample was 0.92. These values are both equivalent to being moderately sorted (Folk, 1974).

The sandstone was disaggregated by hand and water. This method may have allowed some cement to remain attached to the grains causing them to appear coarser than they really are. It is also possible the cement separated from the grains and caused it to add to the fine tail of the grain size frequency curves.

Petrologic and Petrographic Analysis - The BSWS is a medium-grained (with some fine-grains), moderately sorted, rounded, feldspathic arenite with carbonate cement. The most common grain type is monocrystalline quartz (51.7-50.7%) (figures A1 and A2). Rare radial ooid fragments which nucleated around quartz grains were also observed. It is texturally mature

55

and compositionally mature relative to the other facies. Grain contacts are dominantly point and

long contacts. The average interparticle porosity of 15.8% is lower than porosities calculated

(22.0-30.7% by point count) by Morris and others (2005) of the dune microfacies found within

the erg-margin on the east side of the Jurassic seaway. The petrologic and petrographic data

were collected and then plotted on several ternary diagrams which indicate the dominant tectonic

provenance to be the recycled orogen provenance (Dickinson and Suczec, 1979).

Interpretation of the Bitter Seep Wash Sandstone

The Bitter Seep Wash Sandstone (BSWS) is interpreted to be an eolian deposit that filled

a supratidal sabkha pond. The large high-angle TCS and grain size data suggest deposition by

eolian processes. This sandstone is not as well sorted as other well-known erg deposits such as

the Navajo and Wingate Sandstones. We suggest a close association between these eolian dunes

and foreshore (beach) sands, which could easily explain the difference in sorting. Paleocurrent

analysis indicates a southward wind which concurs with other studies of the Entrada erg

(Kocurek, 1981a; Morris and others, 2005; Dickinson and Gehrels, 2009). The blocks of

sandstone sinking into the underlying mudstone indicate a wet environment on which the dunes

prograded. As sea-level rose, the water table rose with it (Kocurek and others, 2001) and

saturated the eolian sand within the supratidal pond. This allowed the wetted sand to become

cohesive or possibly even cemented which aided in preserving the TCS foresets (Inman and

others, 1966). The sand above the capillary fringe (vadose zone) of the water table continued to

migrate over the pond. After the loose sand migrated away, the wetted/cemented sand remained,

resulting in a flat, upper deflation surface. The flat basal contact eliminates the possibility of this

being an eolian-filled migrating tidal channel because a tidal channel complex should produce a

highly scoured basal contact with rip-up clasts. Rip-up clasts were not observed in this

sandstone. It is possible that the eolian dunes derived their sand most recently from locally exposed foreshore deposits which could account for the rare ooids in the sandstone. Inman and others (1966) demonstrate the close proximity of the foreshore to eolian dunes that are prone to migrate into supratidal sabkha zones.

Figure 27 depicts a modern analogue located in the Gulf of California 30 miles west-northwest of Puerto Penasco, Sonora, Mexico. Figure 28 is a depositional model that incorporates six of the seven facies discussed previously as well as the eolian-filled supratidal sabkha pond facies of the BSWS. Only the erg-margin is not represented in this model.

Kocurek (1981a) claims that coastal Entrada erg deposits are characterized by smaller dunes based upon his study of the Entrada Sandstone in northern Utah and Colorado. Isolated, small dune fields must have existed in the study area as well. They were likely proximal to the shorelines. Thus, we document the first recognized isolated eolian dune fields proximal to the Cordilleran front and on the western edge of the Jurassic seaway. We suggest that the dune fields were localized and not attached to the Entrada erg proper located to the south and east of the seaway.

The tectonic provenance is the recycled orogen provenance which concurs with previous studies of the Entrada Sandstone. Bill Dickinson (personal communication) believes that Entrada sediment was, at least in part, derived from the underlying Carmel Formation and Navajo Sandstone. Dickinson and Gehrels (2009) suggest the Navajo, in turn, was derived from Grenvillian sources within the Alleghanian orogeny, with small additions from the Laurentian Shield and Cordilleran magmatic arc provinces. These interpretations are consistent with the tectonic provenance being a recycled orogeny.

RESERVOIR CHARACTERIZATION

Isopach and Volumetrics of the Bitter Seep Wash Sandstone

The Bitter Seep Wash Sandstone's (BSWS) thickness ranges from 0-6.4m (21ft) thick.

The north edge is located along the west side of South Salt Wash (see figure 29)and thins to the

south-southwest near the intersection of I-70 and the mouth of Bitter Seep Wash. A hand

contoured map is presented as figure 29. Note that the thickness gradually increases from north

to south along the easternmost data points. It thickens toward the west from approximately 2m

to approximately 5m before disappearing into the subsurface. To the southwest it thins and

appears to pinch out near I-70 (figure 30). Rough volumetrics calculated using 5,900,000m^2 of

areal extent (calculated using Google Earth Pro software) (figure 30) and an average thickness of

2.9m give a volume of 17,110,000m^3. When multiplied by the average porosity of 15.8%, this

yields potentially 2,700,000 m^3 of pore space. Assuming the porosity is completely saturated

with hydrocarbons and we extract 100% of the hydrocarbons, this is equivalent to approximately

17 million barrels of oil. However, because the sandstone body has been eroded eastward and

goes into the subsurface westward, the actual volume is likely larger than this calculation.

Interpretation of Isopach Using a Modern Analog - The isopach map reflects the

topography that existed during deposition. This is because the sandstone is flat on top reflecting

the "capture" of sand by the wetted capillary fringe of the water table. The sandstone is broadly

undulatory to flat on the basal contact. There is no observable basal scour. As discussed

previously, the sandstone pinches out to the north and thins to the south, a distance of

approximately 5.5km (3.5miles). This indicates that it was likely deposited in a local depression

such as a supratidal pond (see figures 27 and 28). We envision this supratidal pond getting

wetted during spring tides, and flooded during storm events. Local dune fields migrated over the

supratidal sabkha deposits and filled the pond, resulting in thicker deposits in the deeper areas of

the pond and thinner deposits on the outer edges. These edges may have experienced wave

reworking. As the water table and associated capillary fringe rose due to a rise in sea-level, the

sand within the depression was held in place (Kocurek, 2001). The wind continued to blow the

dry tops of the dunes away, resulting in a flat upper deflation surface of the BSWS.

Comparison of Porosity and Permeability Data from All Facies

We attempted to extract 10 plugs from each facies. However, we analyzed only five

samples from the storm facies (table B1). Twenty-three analyses were completed from four

locations within the BSWS. The plugs of each facies were extracted from the same bed over a

lateral distance of approximately 2 m (6.6 ft). The core plug porosity of all facies ranged from

approximately 4-22% and was dominantly interparticle porosity. Table B1 contains the porosity

and permeability data and figure 31 illustrates the porosity and permeability relationship for each

facies.

Permeability was measured at five different confining pressures: 500, 1000, 1500, 2000,

and 2500 psi. The highest permeability measured from each plug was always at the 500 psi

setting. The plotted permeability was measured at 500 psi and ranged from 0.05 to 900 md. As

the confining pressure was raised the permeability dropped. Interestingly, as pressure increased,

the difference in permeability from one pressure to the next decreased (figure 32). This indicates

that compaction due to confining pressure may have a measurable limit. The decreases in

permeability after the pressure increase from 500 to 2500 psi ranged from 0.1 to 169md.

Typically if the initial permeability at 500 psi was low, then the overall drop was small but the

percent of drop was relatively high. If the initial permeability was large, the overall drop was

typically larger, but the percent of drop was relatively small (i.e. the slope of the line was flatter).

The porosity vs. permeability cross plot indicates that each individual facies defines its own field within the cross plot (figure 31). The erg-margin eolian sandstone facies had the greatest maximum porosity, while the BSWS (eolian-filled supratidal pond facies) had the greatest maximum permeability. Note that the erg-margin samples were taken from the algal-matted portion of the sandstone due to the high friability of the TCS portions of the erg-margin facies. We expect that the algal-matted interdune deposits will exhibit lower porosity and permeability than the TCS dune deposits. Lower quality reservoirs include the storm, sabkha, and middle intertidal facies. The subtidal ooid-bearing shoal and bar facies is somewhat transitional. Although we were unable to extract core plugs from the high intertidal facies (the muddiest of all 7 facies), we would expect it to have the lowest porosity and permeability.

Interpretation of Porosity and Permeability Data from All Facies - Three sandstone facies, including the Bitter Seep Wash Sandstone (BSWS) (eolian-filled supratidal sabkha pond), lower intertidal channel, and erg-margin facies have excellent porosity and permeability (figure 31). This is due to better sorting (i.e. especially the relative lack of matrix), roundness, low amounts of carbonate cement, and lower amounts of plagioclase and K-feldspar. In summary, these three facies were compositionally and texturally more mature than the lower reservoir-quality facies. The subtidal ooid-bearing shoal and bar facies is also compositionally and texturally mature, but contains relatively higher amounts of calcite cement (16.7-18.7%). The calcite cement may explain why both porosity and permeability are lower than the reservoir-quality facies, thus this facies is transitional between high- and low-quality reservoir facies. The storm facies has low porosity and permeability, which is likely caused by large amounts of calcite cement (24-27%) occupying available pore space. This large amount of cement may result, in part, from replacement of detrital matrix.

The muddier sabkha and middle intertidal facies each have very low porosity and permeability. These facies have higher amounts of matrix, plagioclase, and K-feldspars. They are finer-grained (siltstones) and angular to subangular, which lowers the porosity and permeability. The porosity that exists in these two facies is interparticle. The mudstone-rich high intertidal facies would likely display the lowest porosity and permeability. These low porosity and permeability deposits lie above and below many of the higher-quality sandstone facies. Thus, interbedding of these facies could produce excellent traps for hydrocarbon accumulations.

DISCUSSION OF THE DEPOSITIONAL MODEL

The Entrada Sandstone of south-central Utah was deposited largely in an arid, mud-rich, tidally influenced littoral zone. Offshore in the higher energy subtidal environment, the ooid-bearing shoal and bar facies was deposited. Moving landward, lower intertidal channels formed and filled with sand. Inland of the lower intertidal channel facies, the middle intertidal facies was deposited in a wet environment that likely had extended times of subaerial exposure resulting in crystal formation due to evaporative pumping. Over time the buried crystals dissolved, thus disrupting any primary bedding that was present. Landward of the middle intertidal facies, deposition of the high intertidal facies occurred. These deposits are very thinly bedded and fine grained (mudstone-rich) due to lower depositional energy of laterally spreading high-tide flood waters. Inland of the high intertidal facies was the sabkha. The sabkha was subaerially exposed during the majority of the time, with occasional times of wetting. Desiccation produced large polygonal fractures. Supratidal ponds formed within the sabkha facies. Eolian sands, possibly sourced from the foreshore and even subtidal ooid-bearing shoal and bar facies (ooids and echinoderm fragments are found in the eolian-filled supratidal sabkha

pond facies), would sometimes fill these depressions. Lastly, and farthest inland, was the erg-margin dominated by low- and high-angle TCS interbedded with algal matting. The erg-margin facies is prominent on the eastern and southern shoreline of the Jurassic seaway but did not exist on the western (Cordilleran side) of the seaway. Instead, an alluvial plain likely existed from the shoreline to the mountain front. We envision only localized dune fields associated with nearshore facies to have been present on the western shoreline of the Jurassic seaway.

CONCLUSIONS

Eolian Deposits West of the Jurassic Seaway

Eight facies within the mudstone-rich Entrada depositional system of south-central Utah have been identified. Key among those is the first documentation of isolated dune fields on the west side of the Jurassic seaway. Small catchment areas in close proximity to the seaway resulted in deposition of dunes forming immediately landward of the foreshore. We propose that foreshore and subtidal ooid-bearing shoal and bar sands were blown landward, sourcing these isolated dune fields. As these dune fields migrated, north to south, in small flat areas between the Jurassic Cordilleran and Jurassic seaway, they would fill supratidal sabkha ponds with sand. We suggest that these newly documented dune fields were relatively small due to their close proximity to the Cordilleran highland and relative great distance from the Entrada erg sediment source on the east and south edges of the Jurassic seaway. As a result, the dunes were not as pervasive as those observed in the erg-margin facies in the Escalante and East San Rafael Swell areas.

Reservoir and Trap Potential

Our depositional model (figure 28) proposes the Entrada depositional system of south-central Utah to be dominated by mudstones and siltstones. Because of their poor reservoir-quality and associated low economic value, geoscientists have not studied them in detail. However, this study shows that within this mud-rich environment, good to excellent reservoir-quality sandstones do exist in the erg-margin, eolian-filled supratidal sabkha pond, and lower intertidal channel facies. These sandstones are enveloped by low porosity and permeability mudstones and siltstones of the sabkha, high intertidal, and middle intertidal facies which could produce excellent seals. The interbedded relationships of high-quality reservoir facies and mudstone/siltstone seals can result in excellent stratigraphic and combination traps for hydrocarbons. If one of these isolated sandstones was charged with hydrocarbons it could prove to be a hydrocarbon reservoir worthy of noting.

Hydrocarbon Exploration

Our proposed depositional model, presented as figure 28, demonstrates that the Entrada Sandstone in south-central Utah has the potential to create hydrocarbon traps if other key components of the hydrocarbon system exist (source, generation, and migration). This model indicates the area with the greatest hydrocarbon reservoir potential is the supratidal zone where erg, erg-margin, and eolian-filled supratidal pond facies exist. Erg and erg-margin facies have been documented along the eastern and southern shorelines of the Jurassic seaway. These facies cover a relatively large area, reducing exploration risk. Although economic potential also lies in the high reservoir-quality lower intertidal channels, they cover a much smaller area and thus increase exploration risk.

Areas where erg and erg-margin facies do not interbed with mudstone-rich facies, such as along the western margin of the seaway (WSRS area), are less prospective as primary targets

based on rough volumetric calculations. The exploration geologist may need to develop a

strategy wherein eolian-filled supratidal pond facies are vertically stacked in order for this area to

be a primary exploration target. If that strategy cannot be developed, mudstone-rich areas like

the western shoreline may serve as secondary exploration targets.

REFERENCES CITED

Beitler, B., Chan, M.A., and Parry, W.T., 2003, Bleaching of Jurassic Navajo Sandstone on Colorado Plateau Laramide highs-evidence of exhumed hydrocarbon supergiants?: Geology, v. 31, no. 12, p. 1041-1044.

Blakey, R.C., Peterson, F., Caputo, M.V., Geesaman, R.C., and Voorhees, B.J., 1983, Paleogeography of Middle Jurassic continental, shoreline, and shallow marine sedimentation, southern Utah: Rocky Mountain Paleography Symposium, v. 2, p. 77-100.

Blakey, R.C., 1989, Triassic and Jurassic geology of the southern Colorado Plateau: Arizona Geological Society Digest, v. 17, p. 369-396.

Blakey, R.C., and Ranney, W., 2008, Ancient landscapes of the Colorado Plateau: Grand Canyon, Grand Canyon Association, 156 p.

Boersma, J.R., 1969, Internal structure of some tidal mega-ripples on a shoal in the Westerschelde Estuary, the Netherlands Report of a Preliminary Investigation: Geologie En Mijnbouw, v. 48, p. 409-414.

Carr-Crabaugh, M., and Kocurek, G., 1998, Continental sequence stratigraphy of a wet eolian system; a key to relative sea-level change, *in* Shanley, K., and McCabe, P., editors, Relative roles of eustasy, climate, and tectonism in continental rocks: SEPM Special Publications, v. 59, p. 213-228.

Clifton, H.E., 1983, Discrimination between subtidal and intertidal facies in Pleistocene deposits, Willapa Bay, Washington: Journal of Sedimentary Petrology, v. 53, p. 353-369.

Dickinson, W.R., and Suczec, C.A., 1979, Plate Tectonics and Sandstone Compositions: AAPG Bulletin, v.63, p. 2164-2182.

Dickinson, W.R., and Gehrels, G.E., 2009, U-Pb ages of detrital zircons in Jurassic eolian and associated sandstones of the Colorado Plateau: Evidence for transcontinental dispersal and intraregional recycling of sediment: GSA Bulletin, v. 121, p. 408-433.

Dott, R.H., 1964, Wacke, greywacke, and matrix; what approach to immature sandstone classification?: Journal of Sedimentary Research, v. 34, p. 625-632.

Eckels, M.T., Suek, D.H., and Harrison, P.J., 2005, New, old plays in southern Uinta basin get fresh look with 3D seismic technology: Oil & Gas Journal, v. 103, p. 32-40.

Fenies, H., and Faugeres, J.C., 1998, Facies and geometry of tidal channel-fill deposits (Acachon Lagoon, SW France): Marine Geology, v. 150, p. 131-148.

Folk, R.L., and Ward, W.C., 1957, Brazos River bar: A study in significance of grain-size parameters: Journal of Sedimentary Petrology: v. 27, p. 3-26.

Folk, R.L., 1974, Petrology of sedimentary rocks: Hemphill, Austin, Tx., 182.p

Harris, P.M., 1977, Sedimentology of the Joulters Cays Ooid Sand Shoal Great Bahama Bank [Ph.D. dissertation]: Coral Gables, University of Miami, 309.

Hicks, T.C., Morris, T.H., and Fairbanks, M.D., 2010, Facies analysis of the transitions between subtidal, intertidal, and supratidal zones of the Entrada Sandstone, south central Utah: A provisional sequence stratigraphic analysis: UGA Guidebook, v. 39.

Hintze, L.F., and Kowallis, B.J., 2009, Geologic history of Utah: Brigham Young University Geology Studies, Special Publication 9, 225 p.

Inman, D.L., Ewing, G.C., and Corliss, J.B., 1966, Coastal Sand Dunes of Guerrero Negro, Baja California, Mexico: Geological Society of America Bulletin, v. 77, p. 787-802.

Keach, R.W., Morris, T.H., McBride, J.H., Mullen, M., Leetaru, H.E., and O'Neal, R., 2006, Interpretations of the Jurassic Entrada Sandstone play using 3D seismic attribute analysis, Uinta Basin, Utah: Utah Geological Survey, Open File Report 493, 22 p.

Kocurek, G., 1981a, Erg Reconstruction: The Entrada Sandstone (Jurassic) of Northern Utah and Colorado: Palaeogeography, Palaeoclimatology, Palaeoecology, v. 36, p. 125-153.

Kocurek, G., 1981b, Significance of interdune deposits and bounding surfaces in aeolian dune sands: Sedimentology, v. 28, p.753-780.

Kocurek, G., and Dott, R.H., Jr., 1983, Jurassic paleogeography and paleoclimate of the central and southern Rocky Mountains Region: Rocky Mountain Paleography Symposium, p. 101-116.

Kocurek, G. and Havholm, K.G., 1991, Eolian event stratigraphy; a conceptual framework: American Association of Petroleum Geologists Bulletin, v. 75 (3), p. 612.

Kocurek, G., Robinson, N.I., and Sharp Jr., J.M., 2001, The response of the water table in coastal aeolian systems to changes in sea level: Sedimentary Geology, v. 139, p. 1-13.

Marino, J.E., 1992, Erg margin and marginal marine facies analysis of the Entrada Sandstone, San Rafael Swell, Utah: Implications to hydrocarbon entrapment: Provo, Brigham Young University, M.S. thesis, 140 p.

Marino, J.E., and Morris, T.H., 1996, Erg margin and marginal marine facies analysis of the Entrada Sandstone, Utah: Implications to depositional models and hydrocarbon entrapment, *in* Morales, M., editor, The continental Jurassic: Museum of Northern Arizona, Bulletin 60, p. 483-496.

Monn, W.D., 2006, A multidisciplinary approach to reservoir characterization of the coastal Entrada erg-margin gas play: Provo, Brigham Young University, M.S. thesis, 33 p.

Morris, T.H., McBride, J.H., and Monn, W.D., 2005, A multidisciplinary approach to reservoir characteristics of the coastal Entrada erg-margin gas play, Utah: Utah Geological Survey, Open File Report 459, 50p.

Perkes, T. and Morris, T.H., in press, Integrating facies analysis, terrestrial sequence stratigraphy, and the first detrital zircon (U-Pb) ages of the Twist Gulch Formation, Utah, USA: Constraining paleogeography and chronostratigraphy: Provo, Brigham Young University, unpublished M.S. thesis.

Peterson, J.A., and Smith, D.L., 1986, Rocky Mountain paleogeography through geologic time. In: Paleotectonics and sedimentation (Ed. By J.A. Peterson), Mem. Am. Ass. Petrol., 41, 3-19.

Pipiringos, G.N., and O'Sullivan, R.B., 1978, Principal unconformities in Triassic and Jurassic rocks, Western Interior United States; a preliminary survey: U.S. Geological Survey Professional Paper 1035-A, p. 29.

Reinson, G.E., Clark, J.E., and Foscolos, A.E., 1988, Reservoir geology of Crystal Viking Field, Lower Cretaceous estuarine tidal channel-bay complex, South-Central Alberta: AAPG Bulletin, v. 72, p. 1270-1294.

Riggs, N.R., and Blakey, R.C., 1993, Early and Middle Jurassic paleogeography and volcanology of Arizona and adjacent areas. in Dunne, G., and McDougall, K., eds., Mesozoic Paleogeography of the Western United States--II: SEPM, Pacific Section, Book 71, p. 347-375.

Schwartz, R.K., 1982, Bedform and stratification characteristics of some modern small-scale washover sand bodies: Sedimentology, v. 29, p. 835-849.

Selley, R.C., 1998, Elements of Petroleum Geology, 2nd Edition: San Diego, Academic Press, 469 p.

Smith, L.S., 1976, Paleoenvironments of the Upper Entrada Sandstone and the Curtis Formation on the west flank of the San Rafael Swell, Emery County, Utah: Brigham Young University Geology Studies, v. 23, p. 113-171.

Southard, J.B., and Boguchwal, L.A., 1990, Bed configurations in steady unidirectional water flows; Part 2, Synthesis of flume data: Journal of Sedimentary Petrology, v. 60, p. 658-679.

Sprinkel, D.A., 1994, Stratigraphic and time-stratigraphic cross sections: A north-south transect from near the Uinta Mountain axis across the Basin and Range transition zone to the

western margin of the San Rafael Swell: U.S. Geological Survey, Miscellaneous Investigations Series, I-2184-D.

Steiner, M.B., 2003, A cratonic Middle Jurassic paleopole: Callovian-Oxfordian stillstand (J-2 cusp), rotation of the Colorado Plateau, and Jurassic North American Apparent polar wander: Tectonics, v.22, p. 22.

Tanner, W.F., 1965, Upper Jurassic Paleogeography of the Four Corners Region: Journal of Sedimentary Petrology, v. 35, p. 564-574.

Thompson, J., and Meadows N.S., 1997, Clastic sabkhas and diachroneity at the top of the Sherwood Sandstone Group: East Irish Sea Basin: Geological Society, London, Special Publications. v. 124, p. 237-251.

Tucker, M.E., and Wright, V.P., 1990, Carbonate Sedimentology: Oxford, Blackwell Scientific Publications, 482 p.

Wilcox, W.T., and Currie, B.S., 2008, Sequence stratigraphy of the Curtis, Summerville, and Stump Formations, eastern Utah and northwest Colorado. In: Longman, M.A., and Morgan, C.D. eds., Hydrocarbon systems and production in the Uinta Basin, Utah, Rocky Mountain Association of Geologists and Utah Geologic Association Publication 37, p. 9-41.

Yeo, R.K., and Risk, M.J., 1981, The sedimentology, stratigraphy, and preservation of intertidal deposits in the Minas Basin system, Bay of Fundy: Journal of Sedimentary Petrology, v. 51, p. 245-260.

Young, S.W., 1976, Petrographic textures of detrital polycrystalline quartz as an aid to interpreting crystalline source rocks: Journal of Sedimentary Petrology, v. 46, p. 595-603.
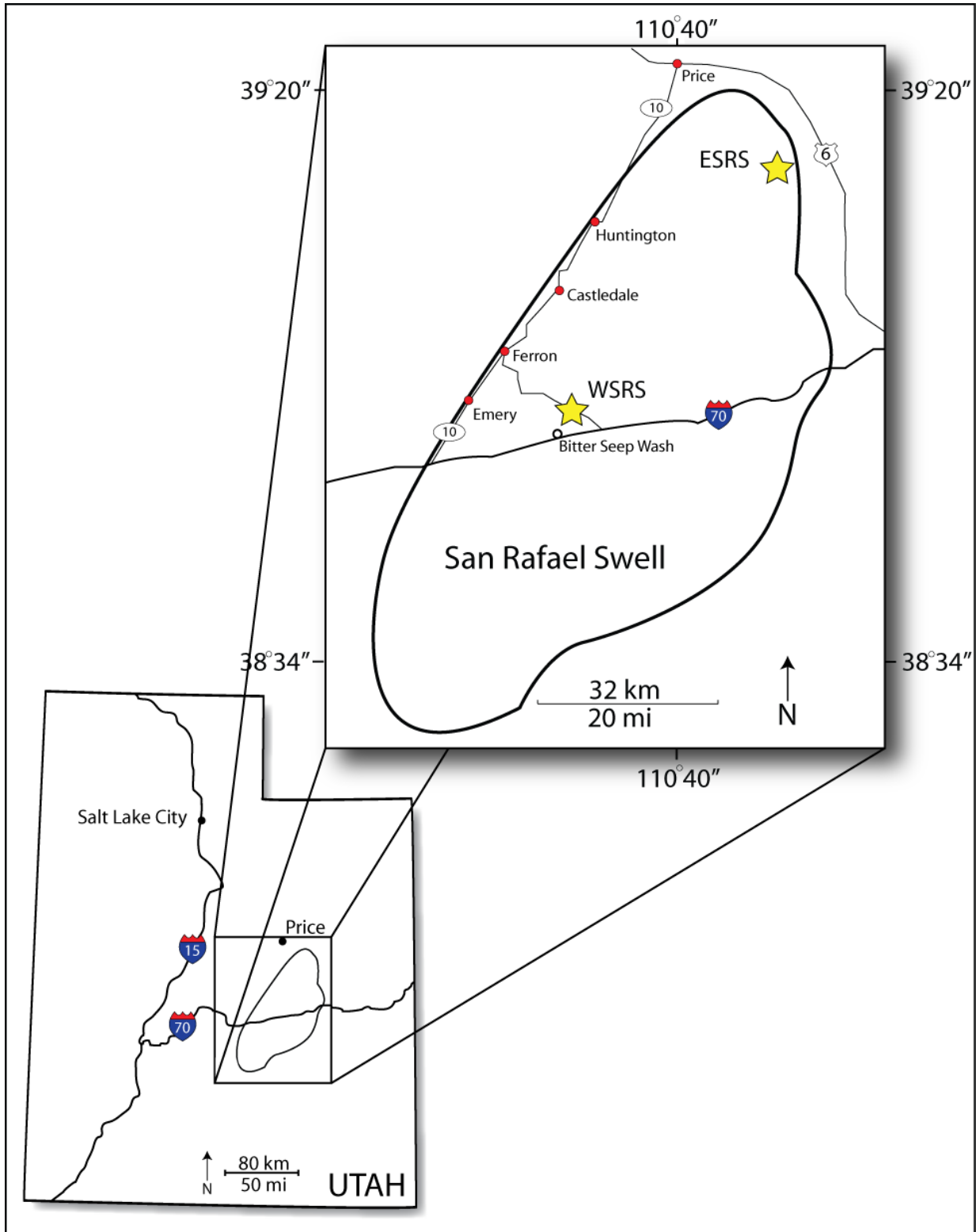
Figure 1: Index map showing the location of the East San Rafael Swell (ESRS) and West San Rafael Swell (WSRS) sections. The location of the Bitter Seep Wash Sandstone is south of the WSRS section in Bitter Seep Wash.
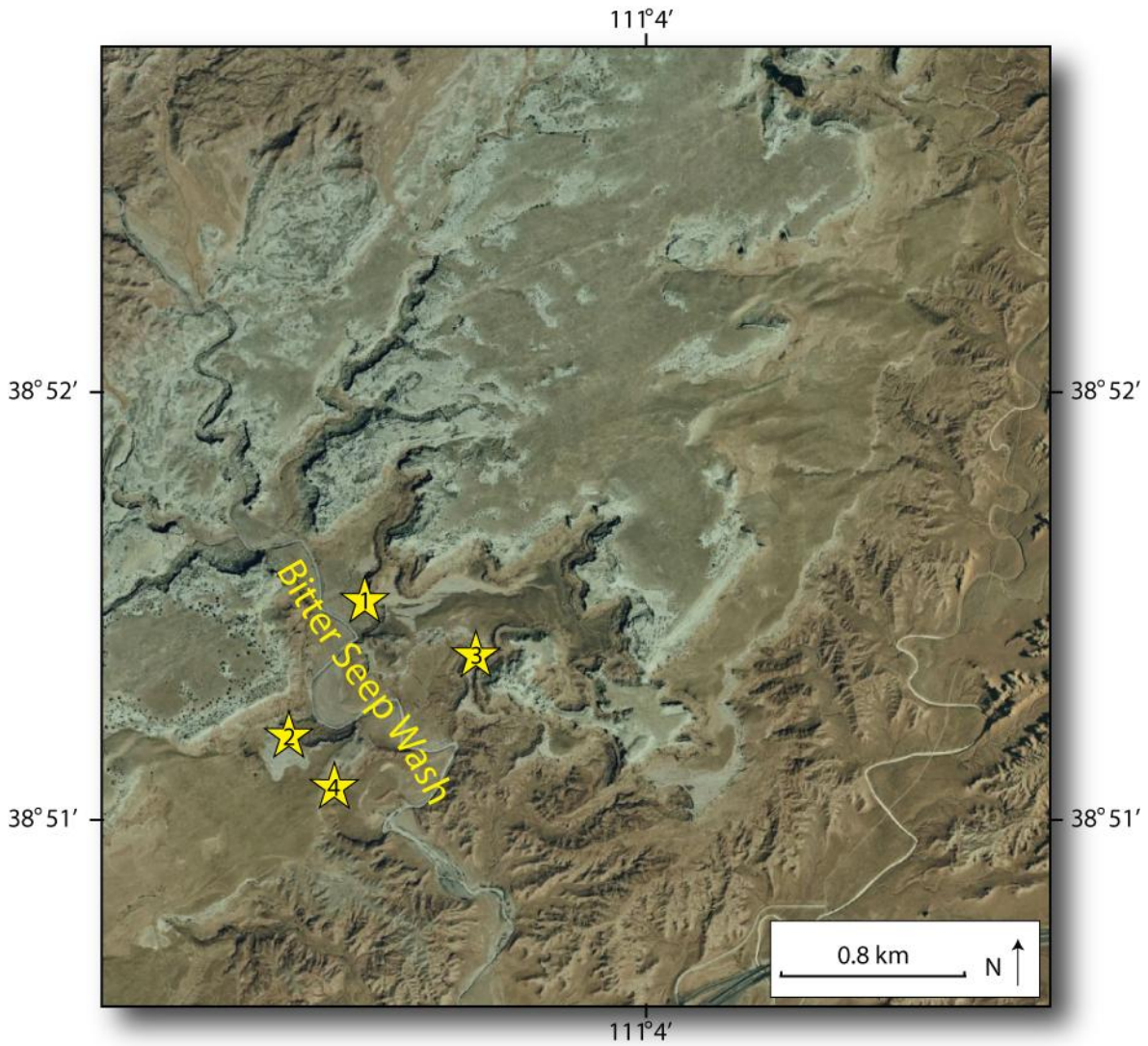
Figure 2: Index map showing the location of core plug extraction sites of the Bitter Seep Wash Sandstone in Bitter Seep Wash. These locations were dependent upon areas where the friability of the sandstone was relatively low. Location 1: 38°51'32.39" N 111°04'50.13' W; Location 2: 38°51'11.54" N 111°05'03.16"W; Location 3: 38°51'23.48" N 111°04'30.53" W; Location 4: 38°51'06.81" N 111°04'56.32" W. (Image from Google Earth Pro-License to Morris).
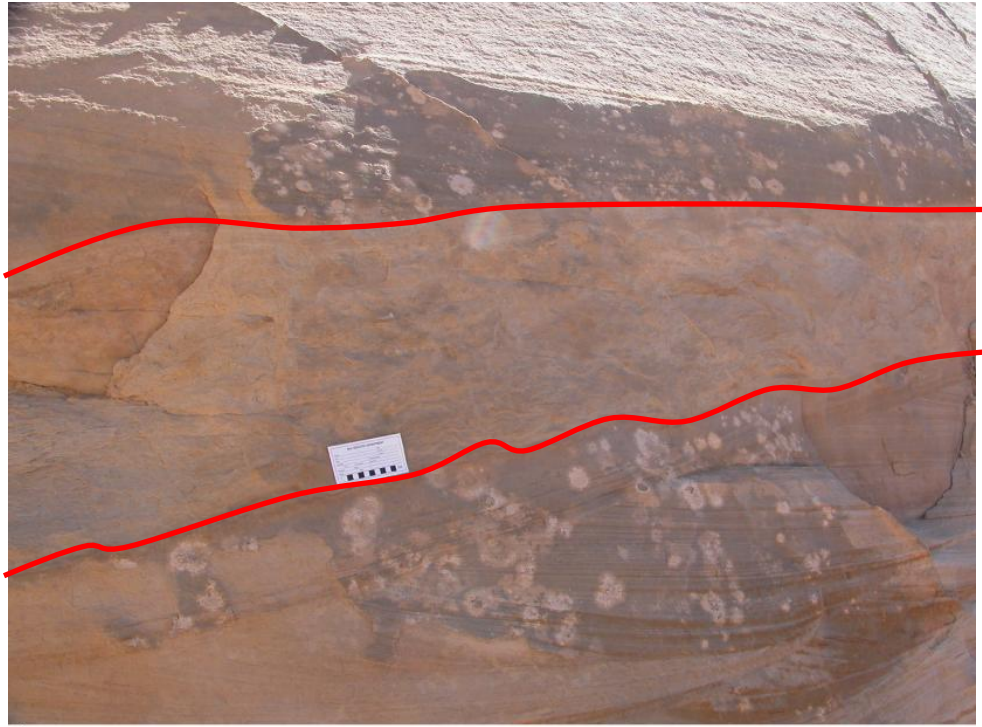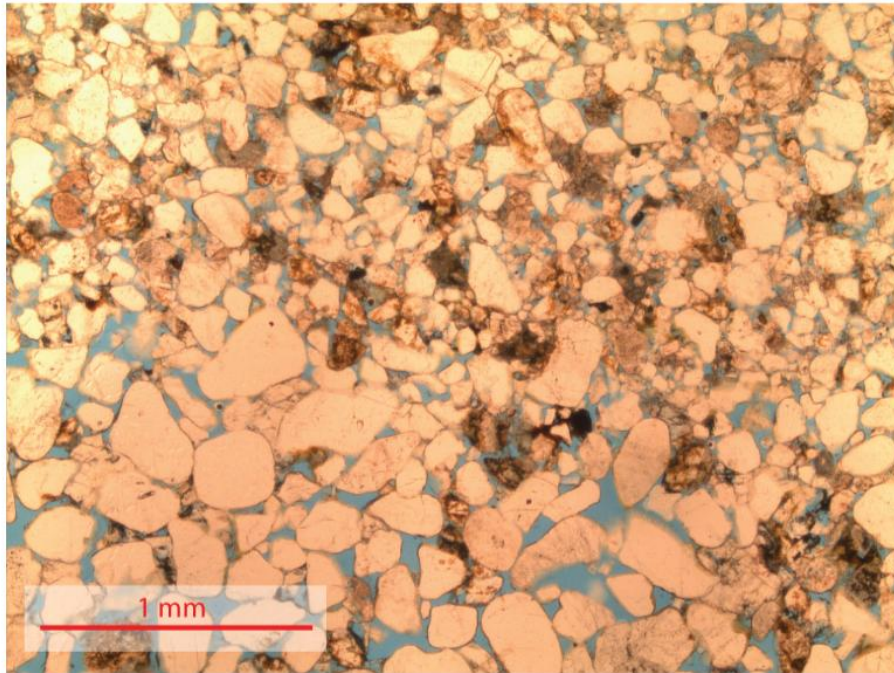
Figure 3: Erg-margin facies at the ESRS section: This is a white to light gray, fine-grained, moderately to well-sorted, sub-rounded to rounded feldspathic arenite with carbonate cement. A-TCS and algal mats of the erg-margin facies as observed in outcrop in the ESRS section. The red lines bound the algal-matted portion of this facies which is interbedded with the TCS. The algal-mat is approximately 50cm thick. B-Photomicrograph of the erg-margin facies, specifically the algal-matted bed. Interparticle porosity ranged from 14-17.7%.

Figure 4: Oblique photograph of TCS present in the erg-margin facies of the Escalante Member of the Entrada Sandstone location south of Escalante, UT adjacent to Hole-in-the-rock Road. Note the numerous reactivation surfaces indicative of a relatively low rate of sediment accumulation. TCS sets are approximately 1m thick.
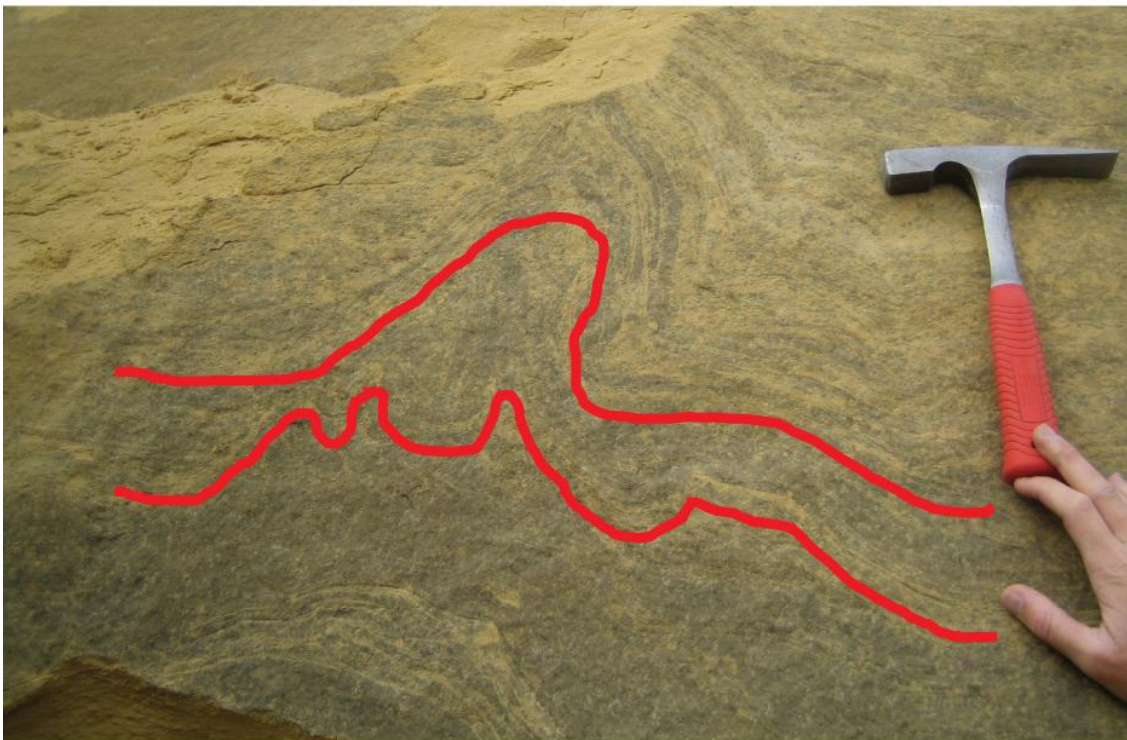
Figure 5: A-Soft sediment deformation present in the erg-margin facies in the Escalante Member of the Entrada Sandstone south of Escalante, UT adjacent to Hole-in-the-rock Road. B-Annotated photograph showing soft sediment deformation.
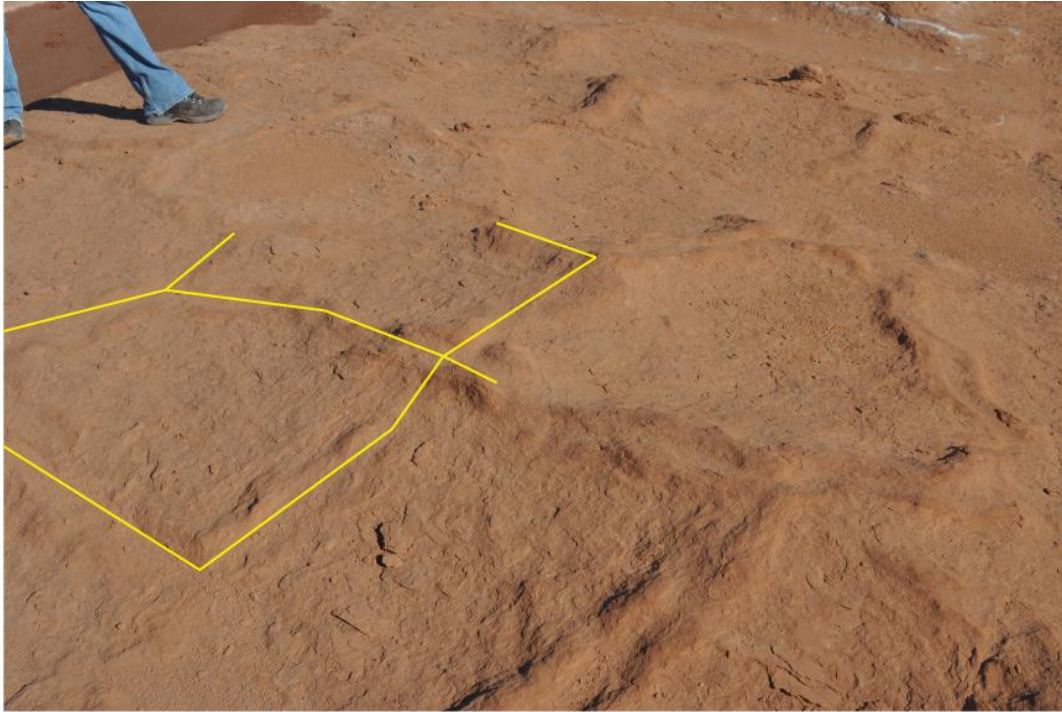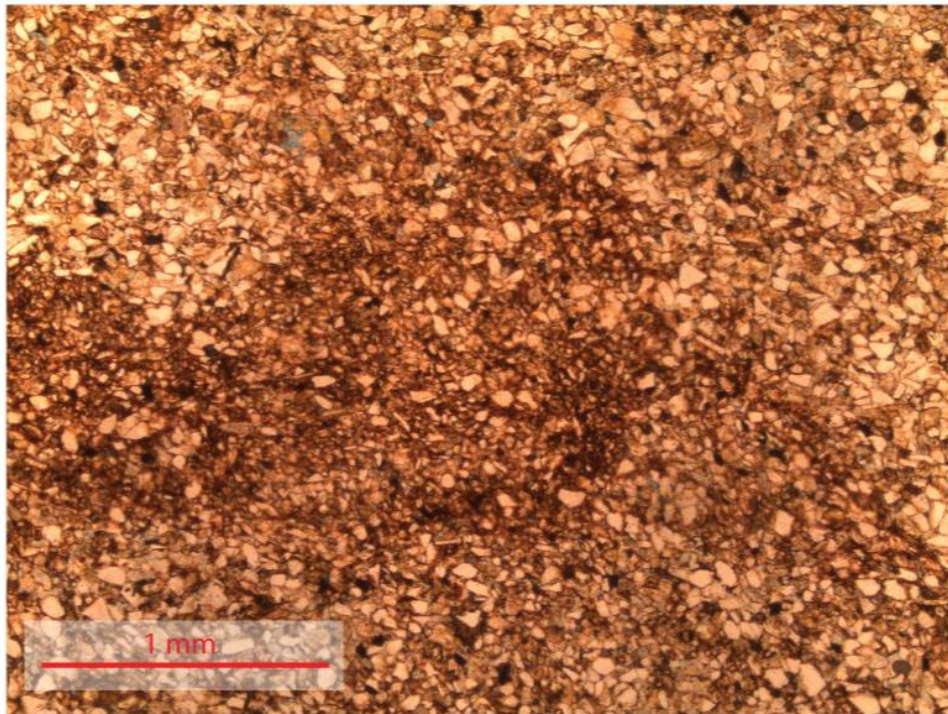
Figure 6: Sabkha facies: This is a light and dark reddish brown, silt-sized, moderately-sorted, sub-angular, feldspathic siltstone with carbonate cement. A-Photograph of desiccation features defined by polygonal ridges present in sabkha facies located at the WSRS section in South Salt Wash. B-Photomicrograph of the sabkha facies. Note the high amount of matrix (7.7-12.3%) (dark brown areas) and the very low porosity (1.3-4%).

Figure 7: Gypsum nodules and disturbed bedding within the sabkha facies of the WSRS section. These features are indicative of subaerial exposure and evaporative pumping.

Figure 8: High intertidal facies: Thinly laminated and muddy strata of the high intertidal facies located at the WSRS section in South Salt Wash. A-Distal view of high intertidal facies. B-Zoomed in view of the high intertidal facies. Note the flat and laterally extensive thin beds of sandstone and siltstone interbedded within the mudstone.
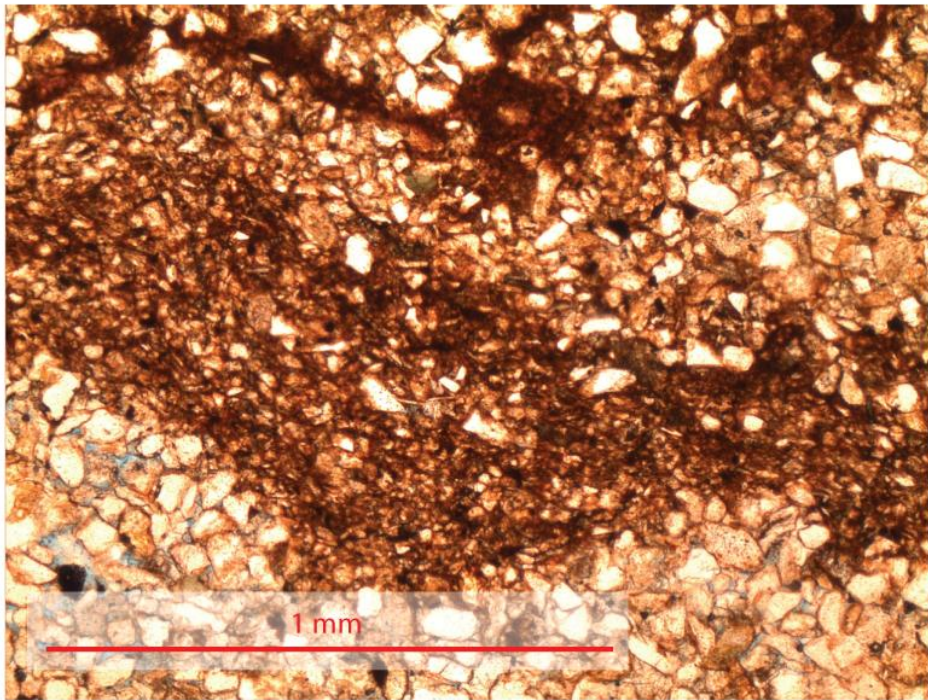
Figure 9: Middle intertidal facies: This is a light reddish-brown, silt-sized with some very fine-grained sand grains, poorly-sorted, angular to sub-angular feldspathic siltstone. A-Photograph of disturbed bedding in the middle intertidal facies located at the ESRS section. Note the mottled and disrupted look of potential bedforms. B-Photomicrograph of the middle intertidal facies. Note the bands of matrix and poor sorting. Although there is some visible porosity in the coarser-grained patches (lower left), the mudstone- and matrix-rich bands produce a very poor reservoir-quality rock.

Figure 10: A-Photograph of disturbed bedding and slope-forming middle intertidal facies located at the WSRS section. B-Cross-cutting gypsum stringers within the middle intertidal facies.
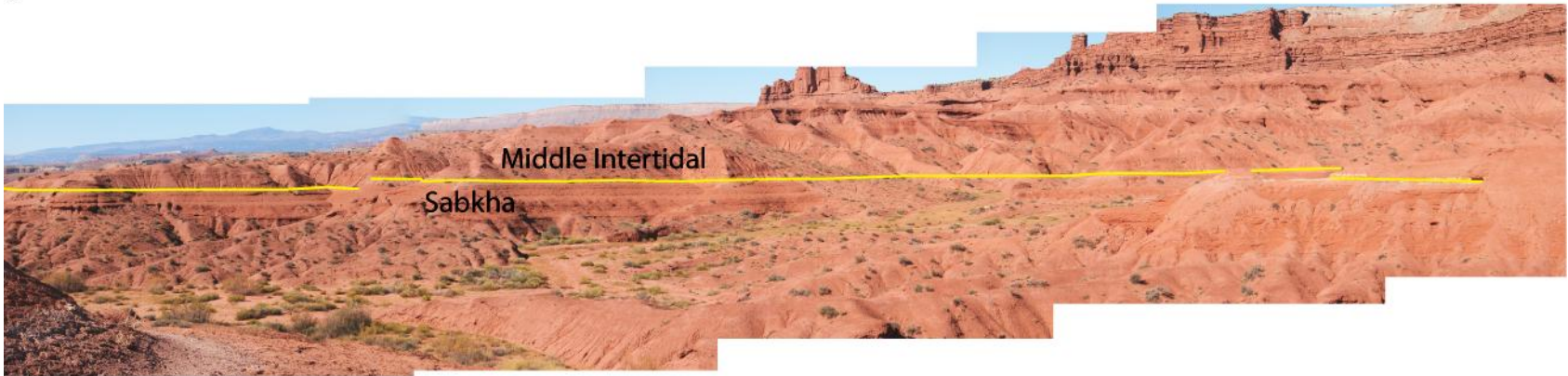
Figure 11: A-Unannotated photograph of an ashbed in the WSRS section. B-Annotated photograph showing the ash bed (yellow) and the facies above and below. Note how flat the ashbed is indicating a very flat depositional environment.
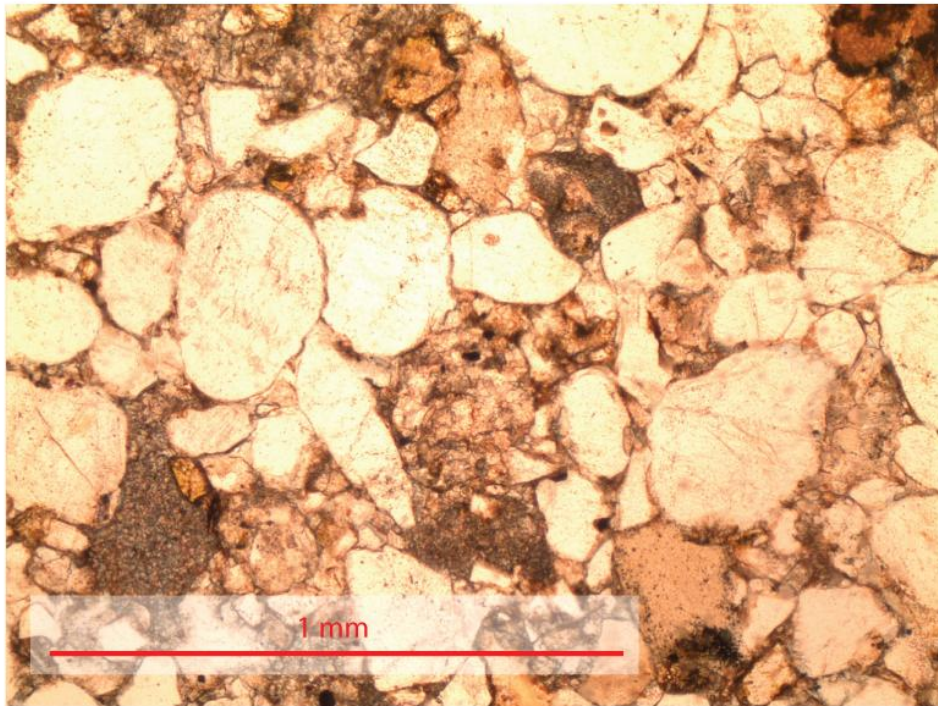
Figure 12: Storm facies: This is a light gray to reddish, medium- to fine-grained, poorly-sorted, sub-angular to sub-rounded feldspathic arenite with carbonate cement which is poikilotropic in some areas. A-Planar lamination of the storm facies located at the WSRS section. B-Photomicrograph of the storm facies. Note the low porosity (0.3%) influenced by poor sorting and compositional immaturity of this facies.
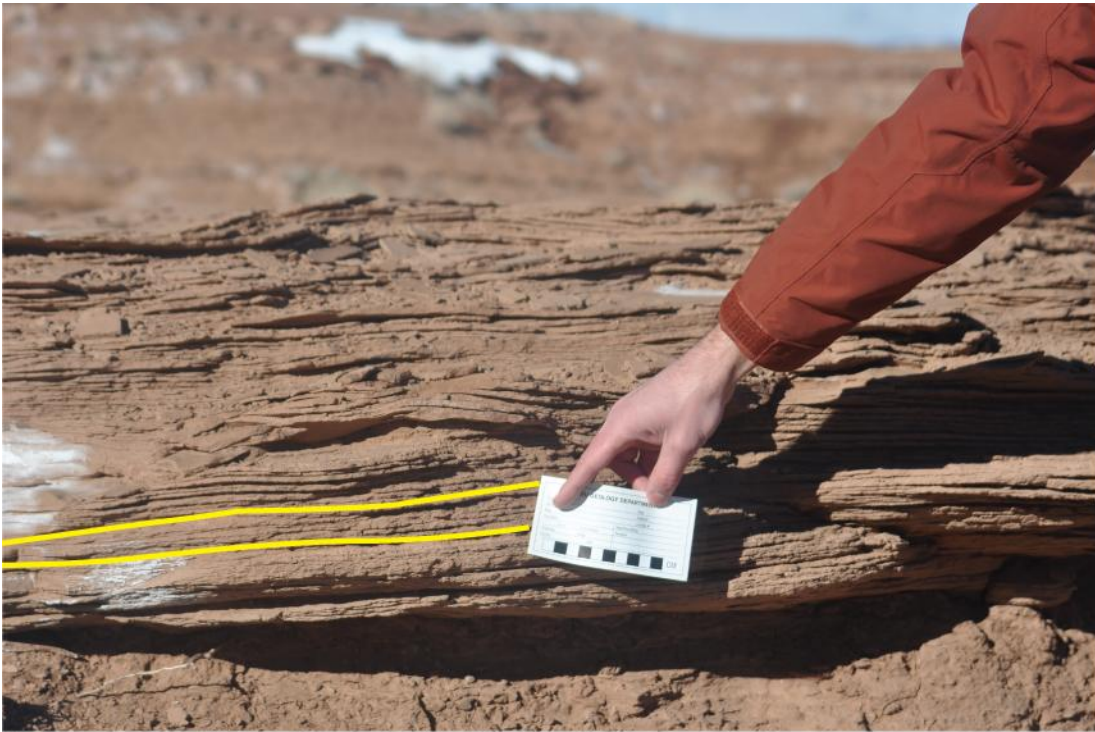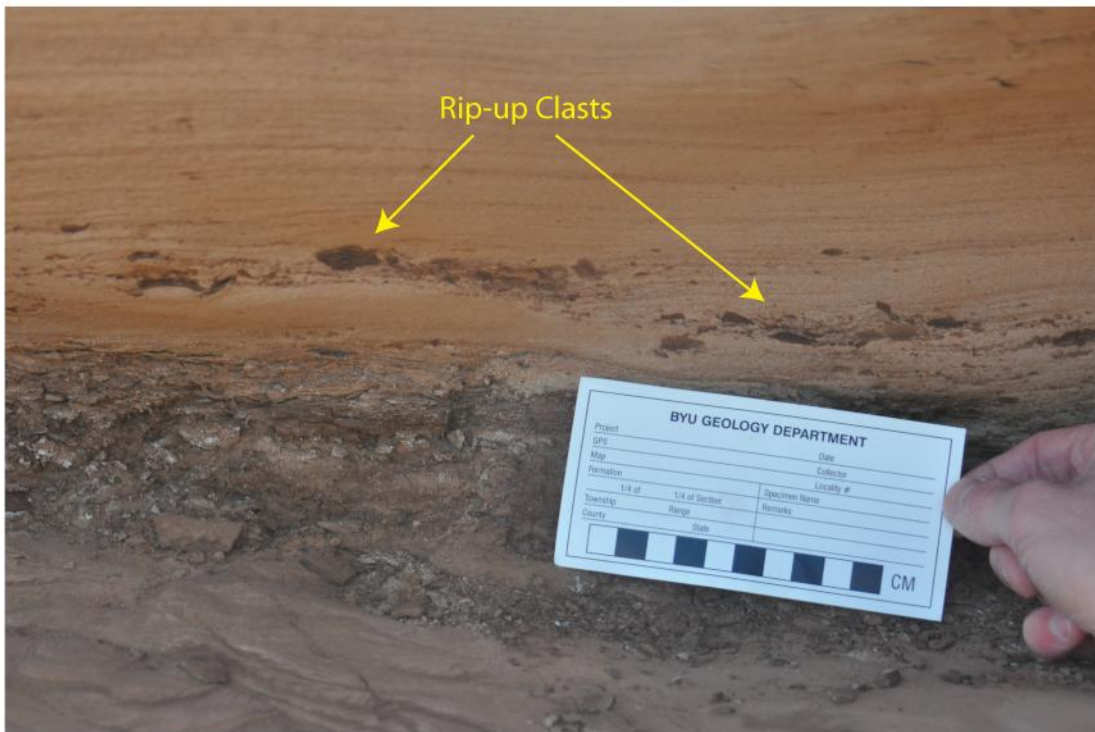
Rip-up Clasts

Figure 13: A-Hummocky cross stratification (HCS) within the storm facies in outcrop at the WSRS section. B-Rip-up clasts found at the base of the storm facies on the WSRS section. HCS is also visible in the upper half of this photograph.

Figure 14: A-Unannotated photograph, looking to the southeast, of the storm facies located at the WSRS section showing its sharp basal contact. B-Annotated photograph illustrating its flat and slightly undulatory basal contact. Here it is approximately 40cm thick.
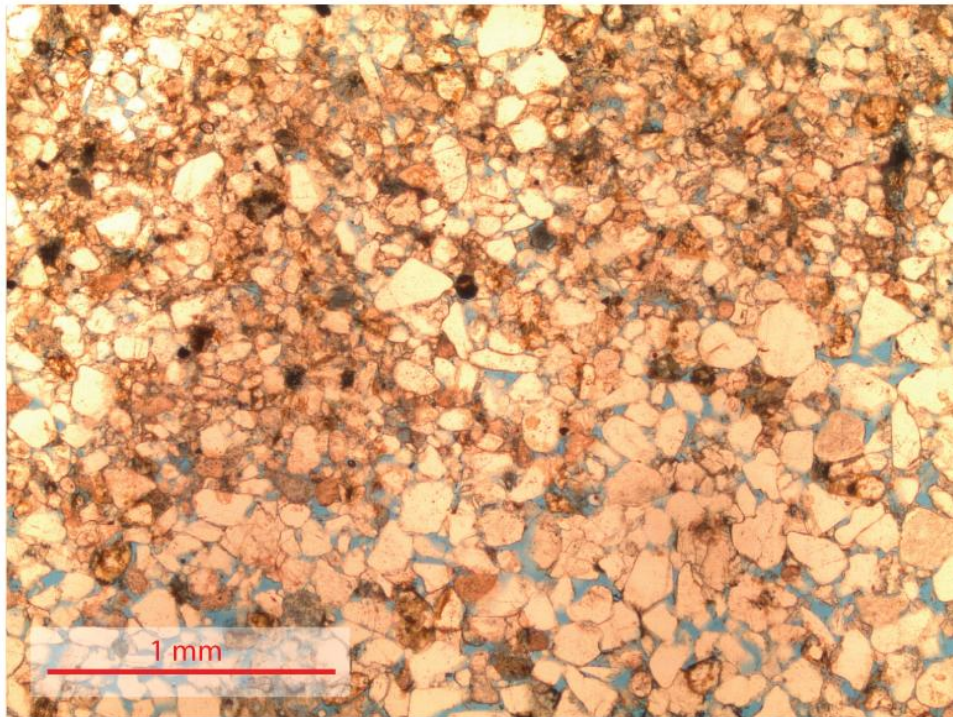
Figure 15: Lower intertidal channel facies located at the ESRS section: This is a light grayish red, fine-grained (with rare medium grains), well to moderately-sorted, sub-rounded feldspathic arenite with carbonate cement. A-Low angle TCS scouring into each other. The presence of possible herringbone stratification indicates different flow directions with ebb and flood tides. B-Photomicrograph of the lower intertidal channel facies. Note the high porosity (17.3-22.3%) among the larger grains and the distinct difference in grain sizes.
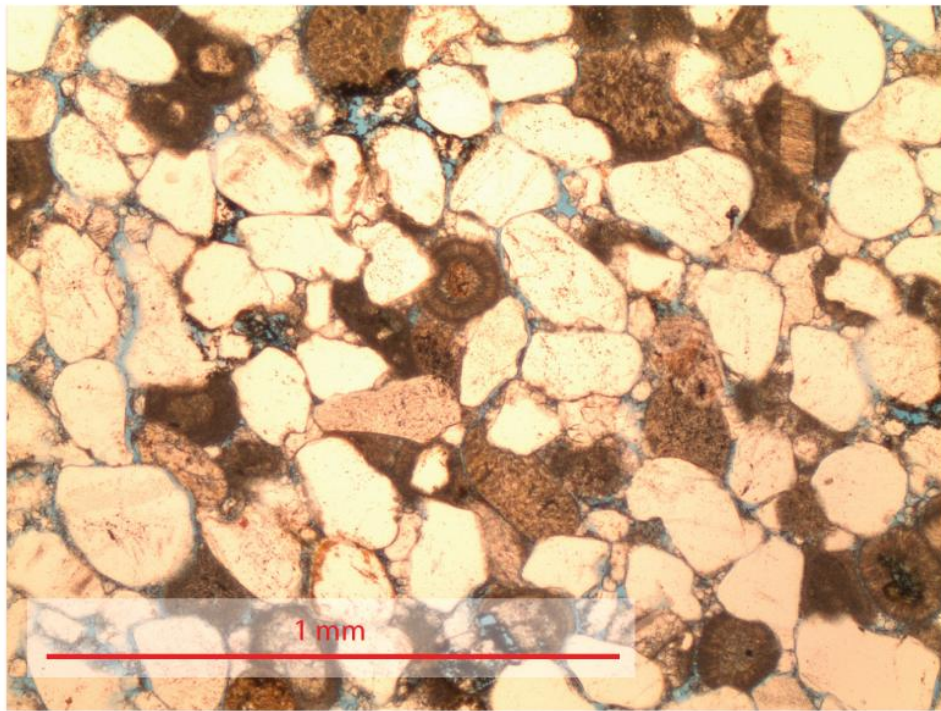
Figure 16: Subtidal ooid‑bearing shoal and bar facies: This is a light yellow to greenish, medium-grained, well-sorted, rounded quartz arenite with carbonate cement. A-A northward photograph of the subtidal ooid‑bearing shoal and bar facies located at the ESRS section. Note the low to high-angle TCS (approx. 1m in height). B-Photomicrograph of the subtidal ooid‑bearing shoal and bar facies. Note the presence of ooids (10.3-13.7%) and the reduced porosity (8.3%).

	Lithology	Identifying Characteristics	Color	Grain-Size	Sorting
Erg-margin (ESRS)	Sandstone (Feldspathic Arenite)	High angle TCS, Interbedded Algal Mats, Soft Sediment Deformation	Light gray to yellowish, at times banded red	Fine sand	Moderate to Well
Sabkha (WSRS)	Siltstone (Feldspathic Siltstone)	Disturbed bedding, polygonal desiccation cracks, and gypsum nodules	Light and dark reddish brown	Silt to very fine sand	Moderate
High Intertidal (WSRS)	Mudstone	Thinly laminated with thin interbedded sandstones	Reddish brown	Silt	Moderate
Middle Intertidal (WSRS)	Sandy Siltstone (Feldspathic Siltstone)	Very disrupted bedding, gypsum stringers/veins, and slope-forming	Light reddish brown	Silt to very fine sand	Poor
Storm Facies (WSRS)	Sandstone (Feldspathic Arenite)	Planar and hummocky lamination. Rip-up clasts visible near the base. Broadly undulatory basal contact.	Light grayish reddish	Medium to fine sand	Poor
Lower Intertidal Channels (ESRS)	Sandstone (Feldspathic Arenite)	Low-angle TCS scouring into each other, low angle herringbone stratification.	Light grayish red	Fine sand	Moderate to Well
Subtidal Ooid-bearing Shoals and Bars (ESRS)	Sandstone (Quartz Arenite)	Low angle TCS, ooids are visible in hand sample (10-13%).	Light yellow to greenish	Medium sand	Well sorted

Table 1: Summary of the major facies observed in the mudstone-rich Entrada Sandstone of south-central Utah. The location of where each facies was described is in parenthese beneath the facies name: East San Rafael Swell(ESRS) and West San Rafael Swell (WSRS).
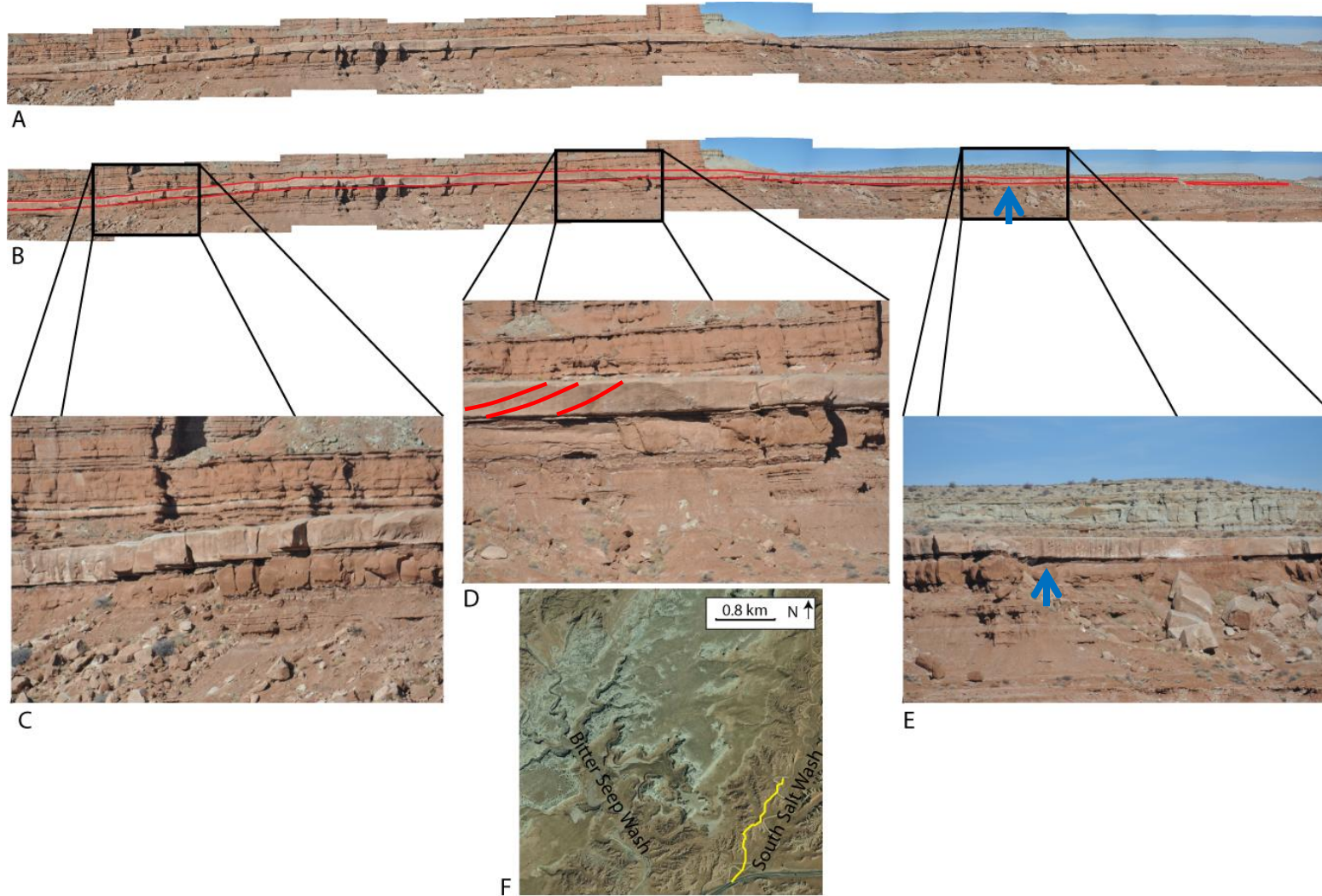
Figure 17: A-Unannotated photomosaic of the Bitter Seep Wash Sandstone (BSWS) looking northwest near the southern end of South Salt Wash. B-Annotated photomosaic of the BSWS. The sandstone ranges from approximately 4m to 1m going from left to right. C, D, and E-Illustrating the continuously flat basal contact of the BSWS. The red lines in D indicate foreset lamination of the BSWS. F-Map showing (in yellow) the location represented by this photomosaic (Image from Google Earth Pro-License to Morris). The blue arrows in A and E show the location of the soft sediment deformation illustrated in figure 22.
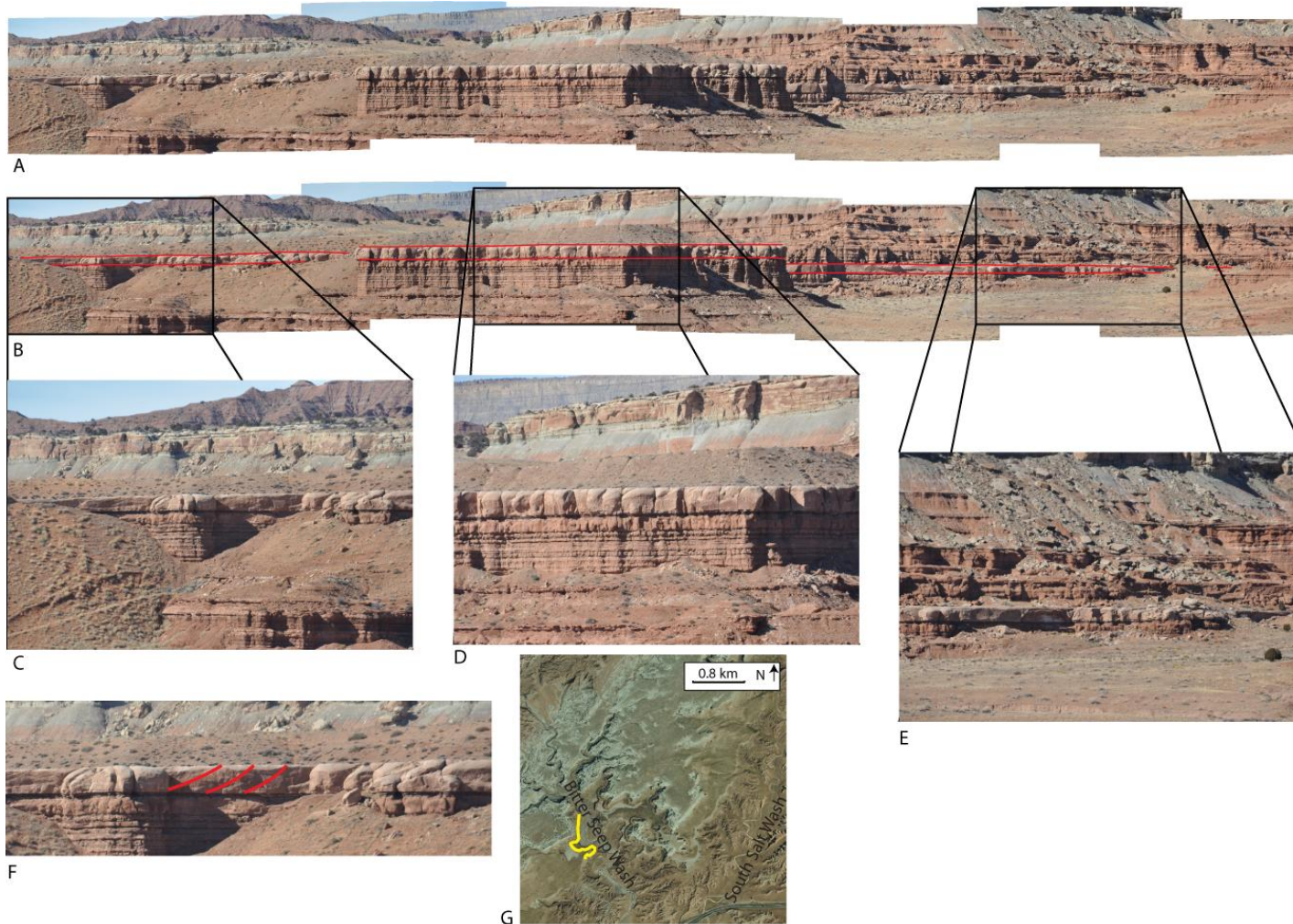
Figure 18: A-Unannotated photomosaic of the Bitter Seep Wash Sandstone (BSWS) in Bitter Seep Wash. B-Annotated photomosaic. The red lines bound the upper and basal surfaces of the BSWS. C, D, and E-Close-up photographs illustrating the flat nature of the upper and basal surfaces. The flat basal contact suggests dune migration into a flat, wet topographic low, such as a supratidal pond wetted during spring tides and storm surges. The flat basal contact argues against this facies being deposited by backshore eolian sands infilling a migrating tidal inlet channel complex because one would expect to see scour at the basal contact and associated rip-up clasts. F-Close-up of C showing the foreset lamination present in the BSWS. G-Map showing the location the photomosaic represents (Image from Google Earth Pro-License to Morris).
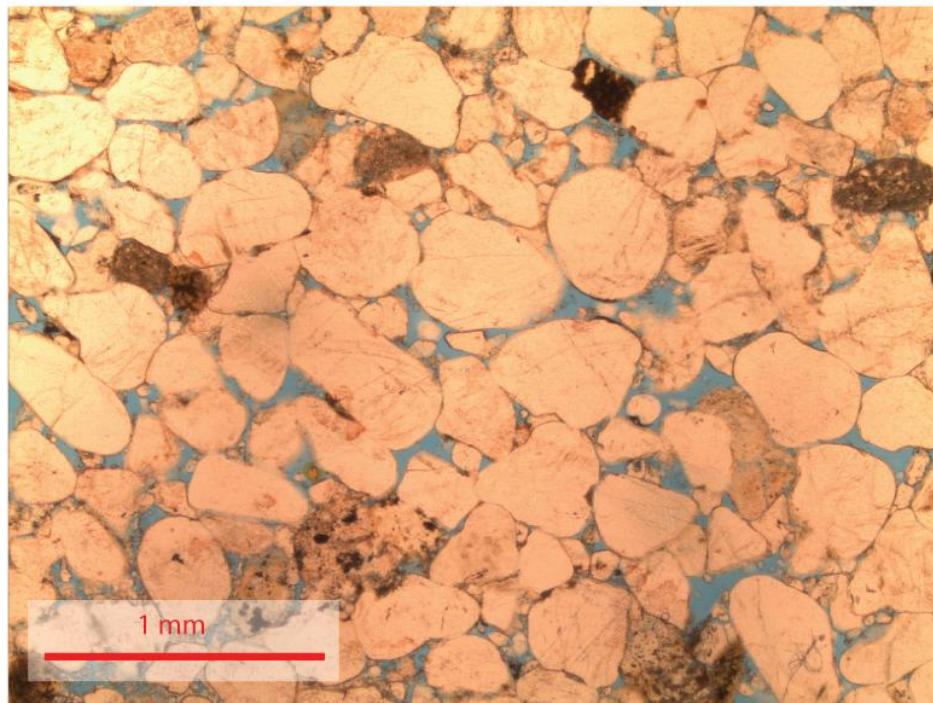
Figure 19: A-TCS of the Bitter Seep Wash Sandstone (BSWS) in South Salt Wash. Bed thickness is approximately 2m. Note how the foreset lamina extend from the basal surface to the upper surface (a thickness of approx. 1m). B-Photomicrograph of the BSWS. The grains are round and moderately-sorted. Porosities reached values of 10.7-17.7%.

Figure 20: A-Photograph of TCS extending from the base to the top of the Bitter Seep Wash Sandstone (approx. 1m). B-Annotated photograph illustrating TCS that is present.

Figure 21: A-Photograph, looking south, of the upper surface of the Bitter Seep Wash Sandstone (BSWS) in Bitter Seep Wash. Sandstone thickness at edge (lower left of photograph) is approximately 4-5m. B-Annotated photograph of the BSWS showing the many foreset laminations and reactivation surfaces visible on its upper surface. These were very useful in determining a strong southward paleocurrent direction. Also note the flatness of this upper surface which we interpret to result from the capillary fringe of the groundwater "capturing" the wetted sand while the upper dune crests were deflated away.

Figure 22: A-Distal photograph of the Bitter Seep Wash Sandstone (BSWS) in South Salt Wash. The thickness of the sandstone here is approximately 1m. Outline of lower photograph is highlighted in red. B-Close-up of the BSWS. Note the block of sand that has sunk into the mud and siltstone below (white arrow). This soft sediment deformation is indicative of a wet environment during deposition of the BSWS. Also note the flatness of the basal contact away from the soft sediment deformation.
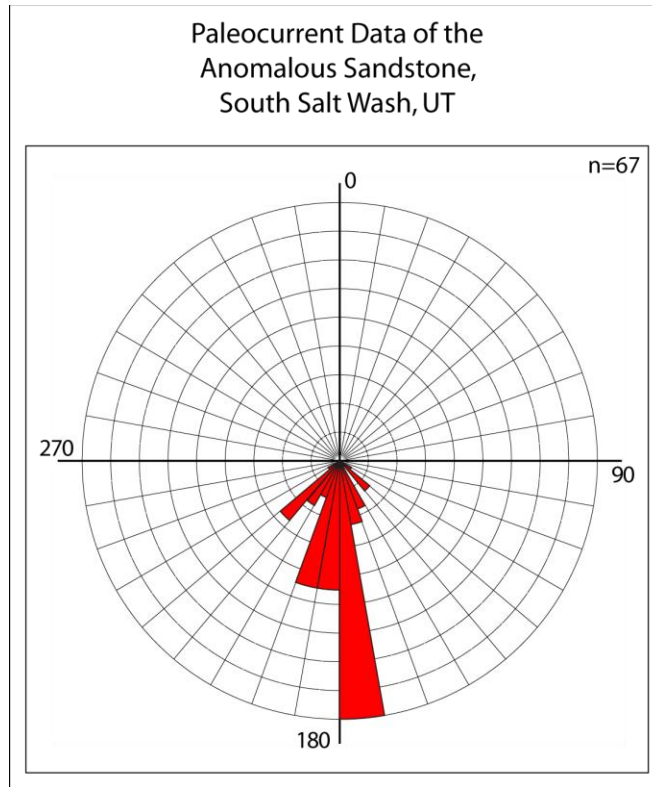
Figure 23: Rose plot showing prevailing modern current direction collected from the Bitter Seep Wash Sandstone. Due to rotation of the Colorado Plateau the actual paleocurrent direction would be 9° counterclockwise from the modern current direction (Steiner, 2003). Each radiating circle represents approximately 2.3 measurements. Petals are in increments of 10 degrees azimuth. 67 measurements were obtained.
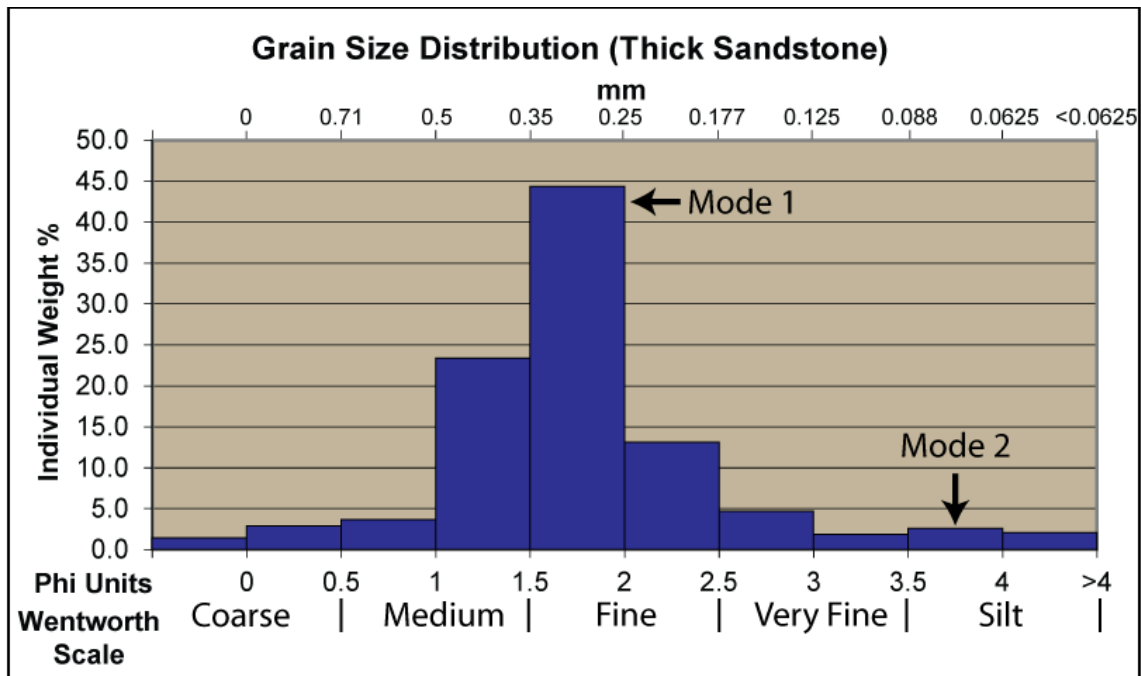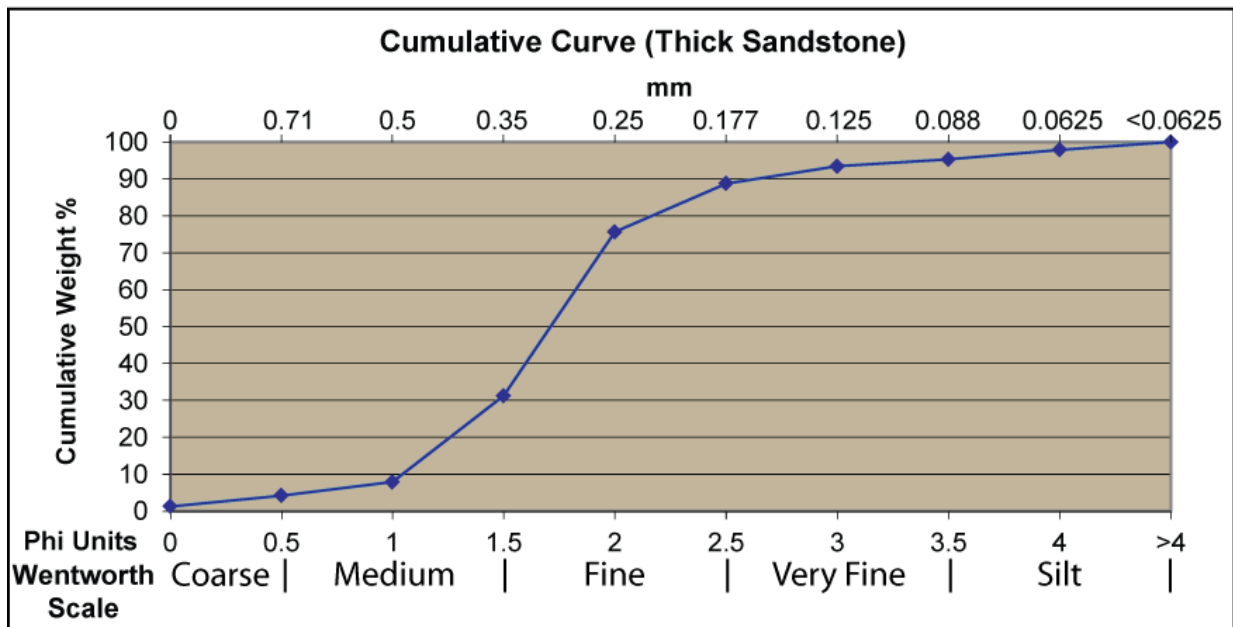
Figure 24: A-Grain size histogram from a thick portion of the Bitter Seep Wash Sandstone. Note the dominant grain sizes to be 1.5 and 2 phi which are equivalent to upper-medium and lower-medium sand, respectively. There is a small increase in very fine sand which by definition would make this sample bimodal. B-Grain size cumulative curve showing the majority of grains to be medium to very-fine sand.
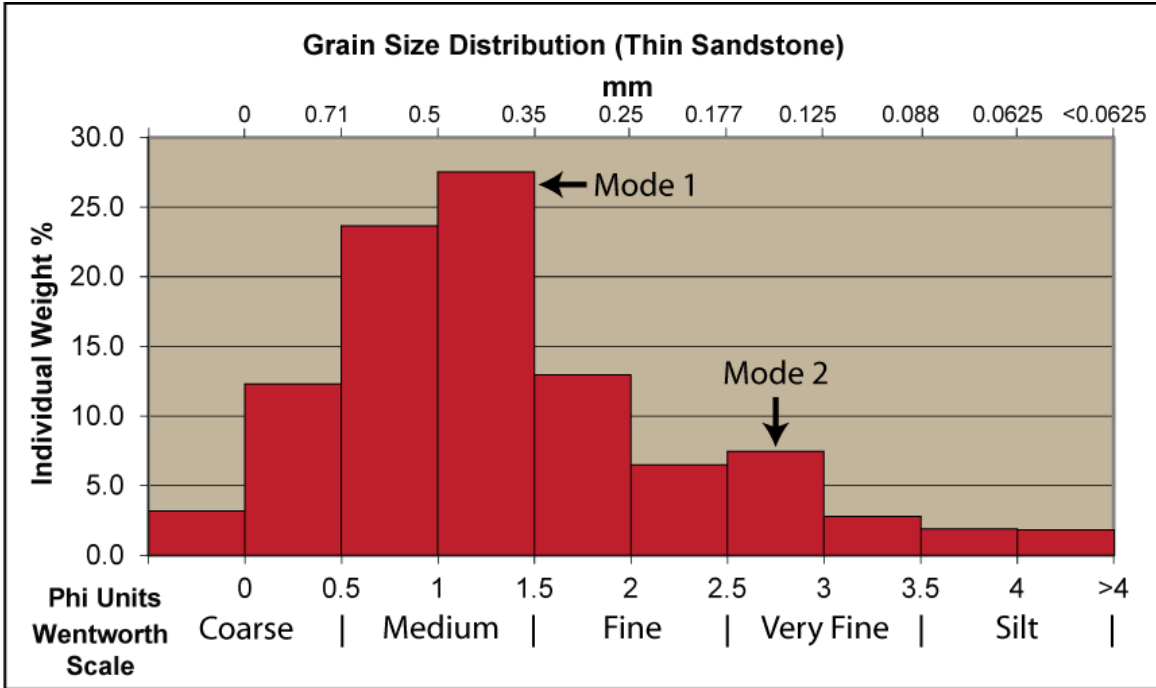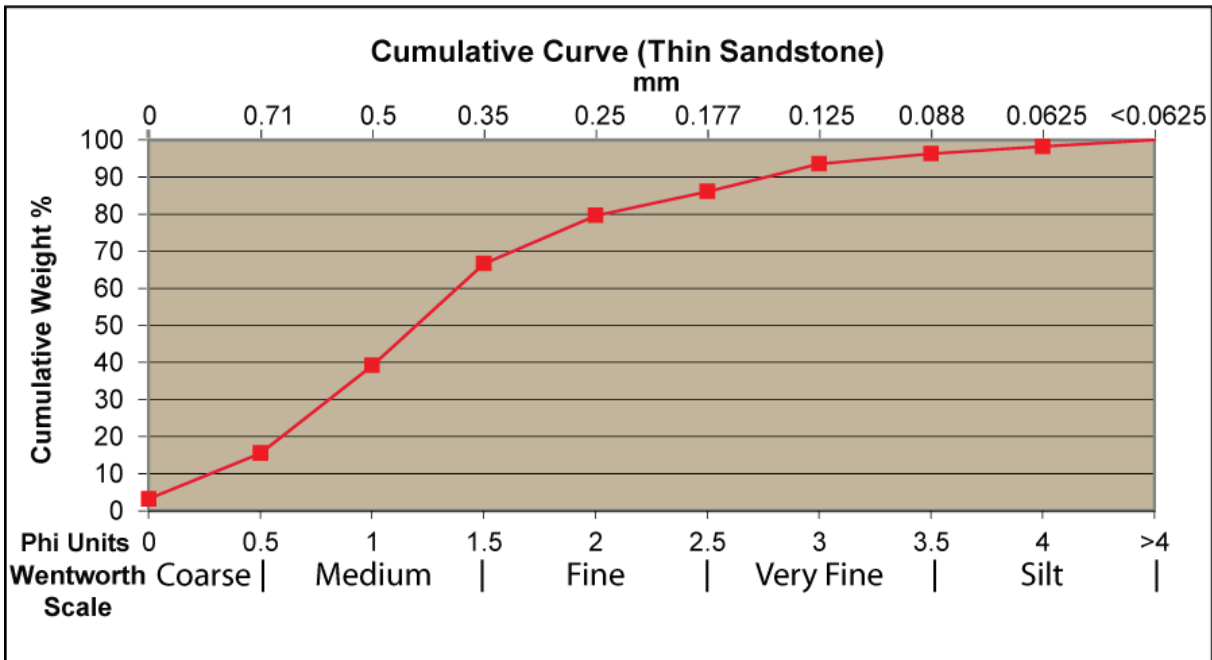
Figure 25: A-Grain size histogram from a thin portion of the Bitter Seep Wash Sandstone. Note the bimodal distribution observed at 1.5 and 3 phi which are equivalent to upper-medium and lower-fine sand. B-Grain size cumulative curve showing the majority of grains to be medium to very-fine sand.
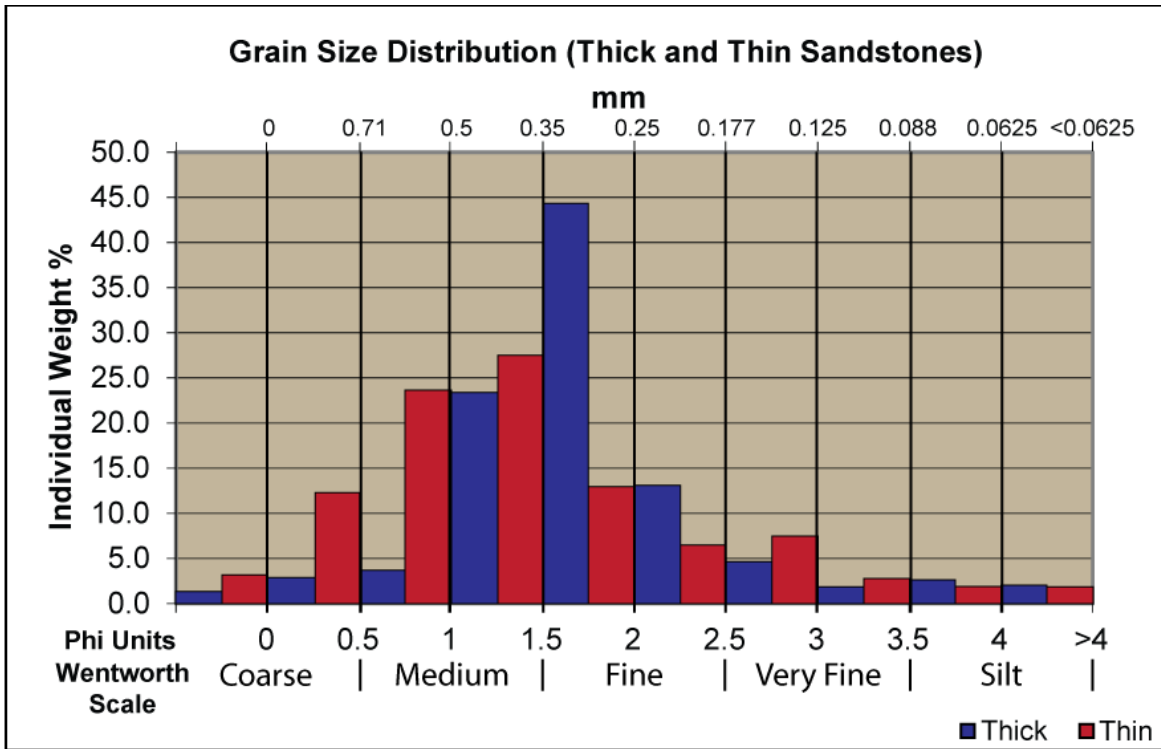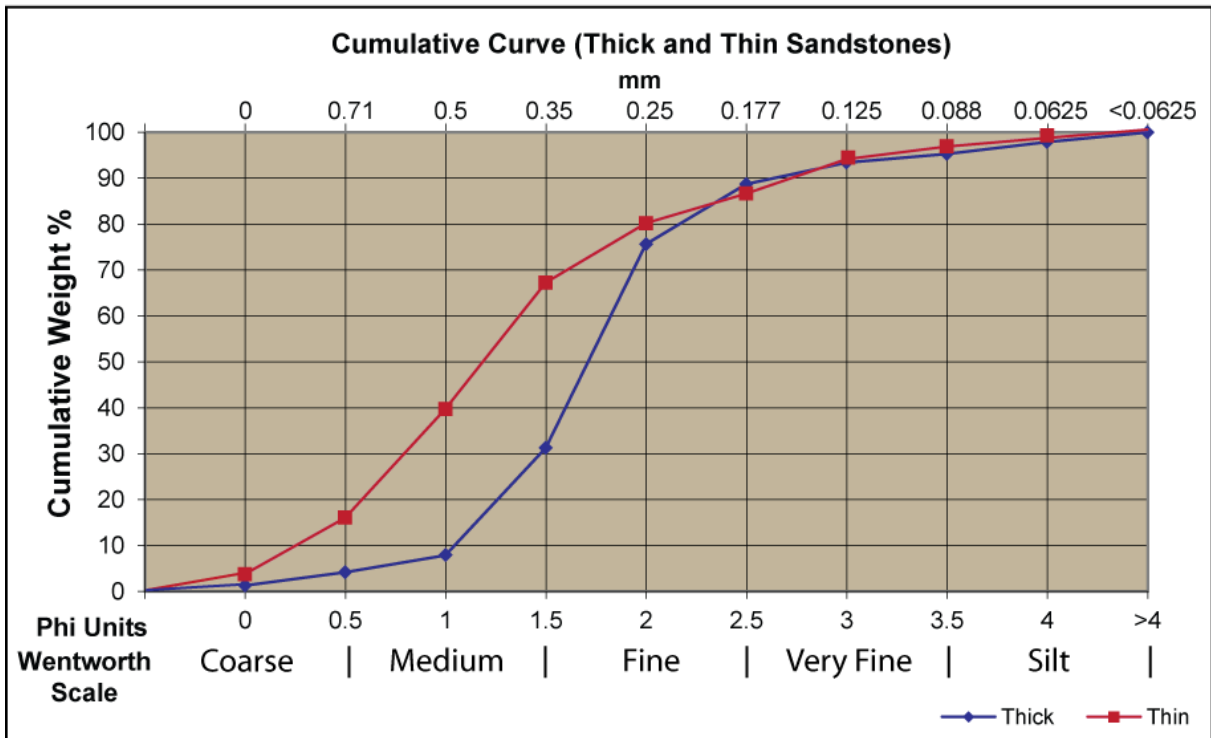
Figure 26: A-Side by side comparison of the grain size histograms from the thick and thin sandstone samples. B-Side by side comparison of the cumulative curves from the thick and thin sandstone samples.

mm	Phi Units	Thick			Thin		
		Weight (g)	Ind. Wt. %	Cum. Wt. %	Weight (g)	Ind. Wt. %	Cum. Wt. %
1	0	86.42	1.3	1.3	265.52	3.2	3.2
0.71	0.5	187.87	2.9	4.2	1029.3	12.3	15.5
0.5	1	239.83	3.7	7.9	1982.2	23.7	39.2
0.35	1.5	1507.6	23.3	31.3	2304.5	27.5	66.7
0.25	2	2864.1	44.4	75.6	1084	12.9	79.6
0.177	2.5	845.17	13.1	88.7	541.87	6.5	86.1
0.125	3	301.85	4.7	93.4	626.16	7.5	93.6
0.088	3.5	120.73	1.9	95.3	230.82	2.8	96.3
0.0625	4	168.92	2.6	97.9	158.35	1.9	98.2
<0.0625	>4	134.2	2.1	100.0	152.82	1.8	100.0
		6456.69			8375.54		

Graphical Statistical Parameter Equations

Graphic Mean:

$$Mz = \frac{\Phi16 + \Phi50 + \Phi84}{3}$$

Inclusive Graphic Standard Deviation:

$$\sigma i = \left(\frac{\Phi84 - \Phi16}{4}\right) + \left(\frac{\Phi95 - \Phi5}{6.6}\right)$$

Inclusive Graphic Skewness:

$$SKt = \frac{\Phi84 + \Phi16 - 2\Phi50}{2(\Phi84 - \Phi16)} + \frac{\Phi95 + \Phi5 + \Phi50}{2(\Phi95 - \Phi5)}$$

Graphic Kurtosis:

$$KG = \frac{\Phi95 - \Phi5}{2.44(\Phi75 - \Phi25)}$$

Table 2: Data collected from the grain size analysis of the thick and thin sandstone samples of the Bitter Seep Wash Sandstone and the equations (Folk and Ward, 1957) used for calculating the grain-size statistical parameters by graphic methods.

		Thick	Thin
Cumulative Weight Percentile	5	0.55	0.07
	16	1.1	0.5
	25	1.3	0.65
	50	1.74	1.18
	75	2	1.81
	84	2.3	2.38
	95	3.65	3.05
Graphic Mean		1.53	1.21
Graphic Standard Deviation		0.77	0.92
Graphic Skewness		1.21	1.06
Graphic Kurtosis		1.81	1.05

Table 3: Statistical parameters calculated by graphical methods for the thick and thin sandstone samples of the Bitter Seep Wash Sandstone.
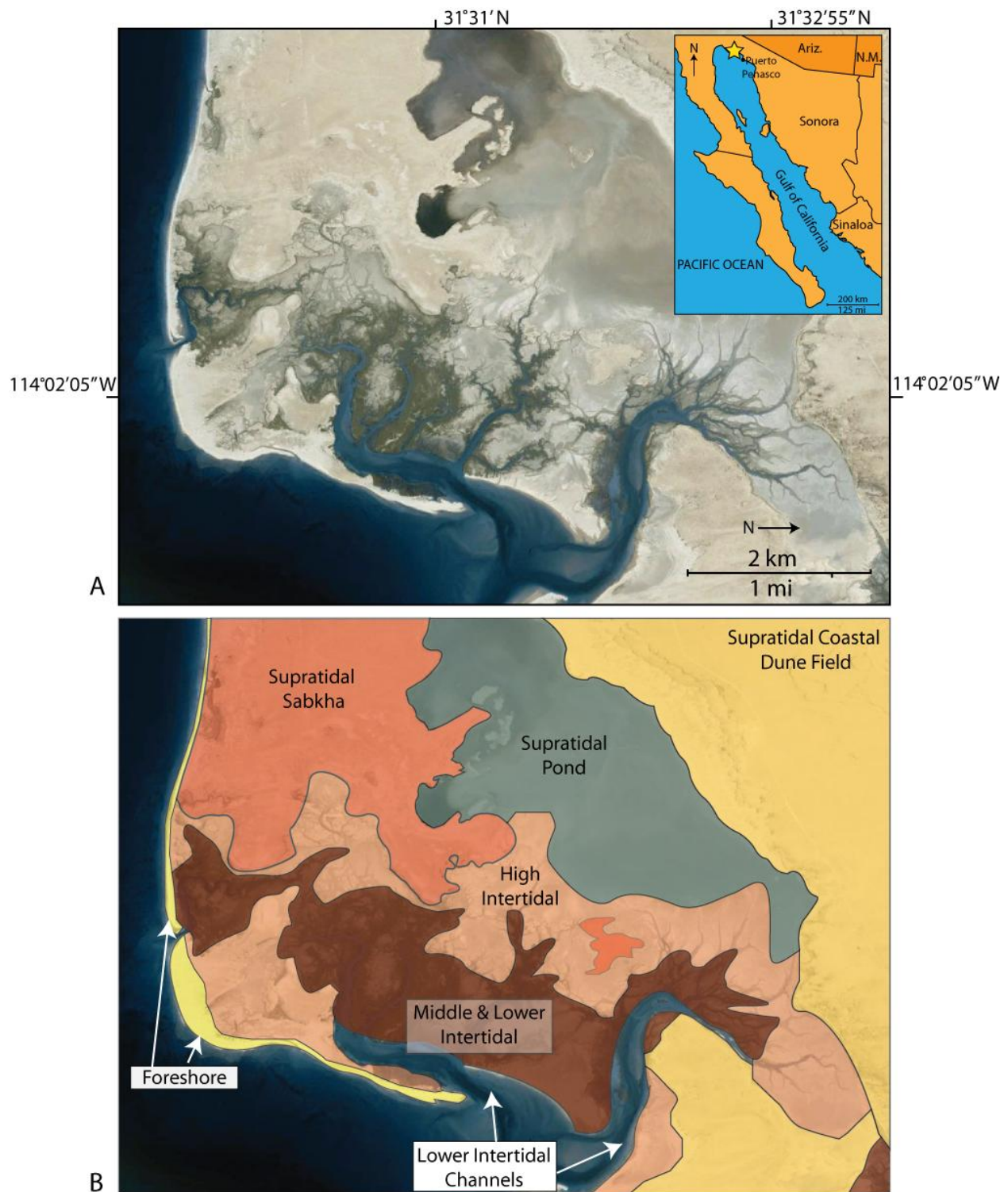
Figure 27: A - Modern analog located at the north end of the Gulf of California (31°31'20.98"N 114°02'22.36"W) 30 miles west-northwest of Puerto Penasco, Sonora, Mexico. B-Annotated photograph of the modern analog showing the facies used in this study. The supratidal pond is approximately 6 km (3.7 mi) long and in places more than 2 km (1.2 mi) wide. (Images from Google Earth Pro-License to Morris)
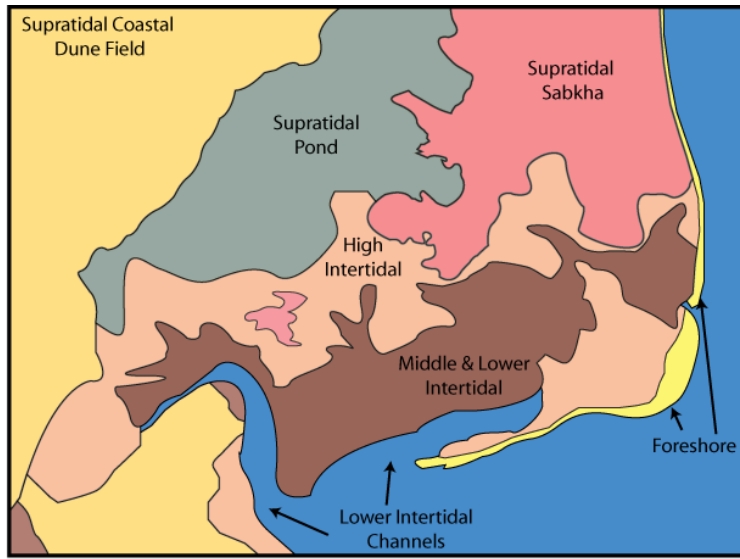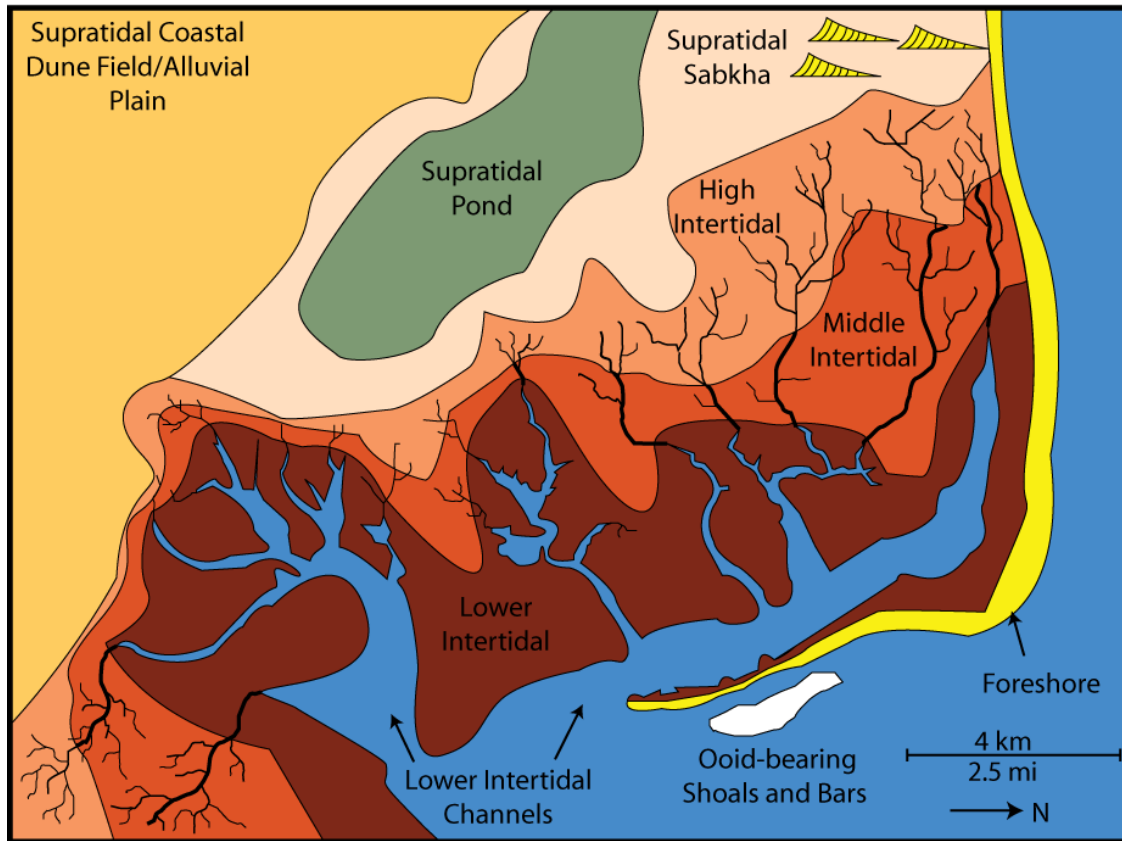
Figure 28: A-A mirror-image of the tidal environment at the north end of the Gulf of California depicted in figure 27. B-Depositional model for the subtidal, intertidal, and supratidal deposits of the Entrada Sandstone of south-central Utah (modified from Hicks and others, 2010). The western side of the seaway lacked well developed coastal dune complexes that are present to the south and east. Instead localized dune fields developed (possibly in association with the foreshore) and migrated into the supratidal pond. The model is scaled to match that of the modern analog in figure 27 and the Bitter Seep Wash Sandstone in South Salt Wash and Bitter Seep Wash.
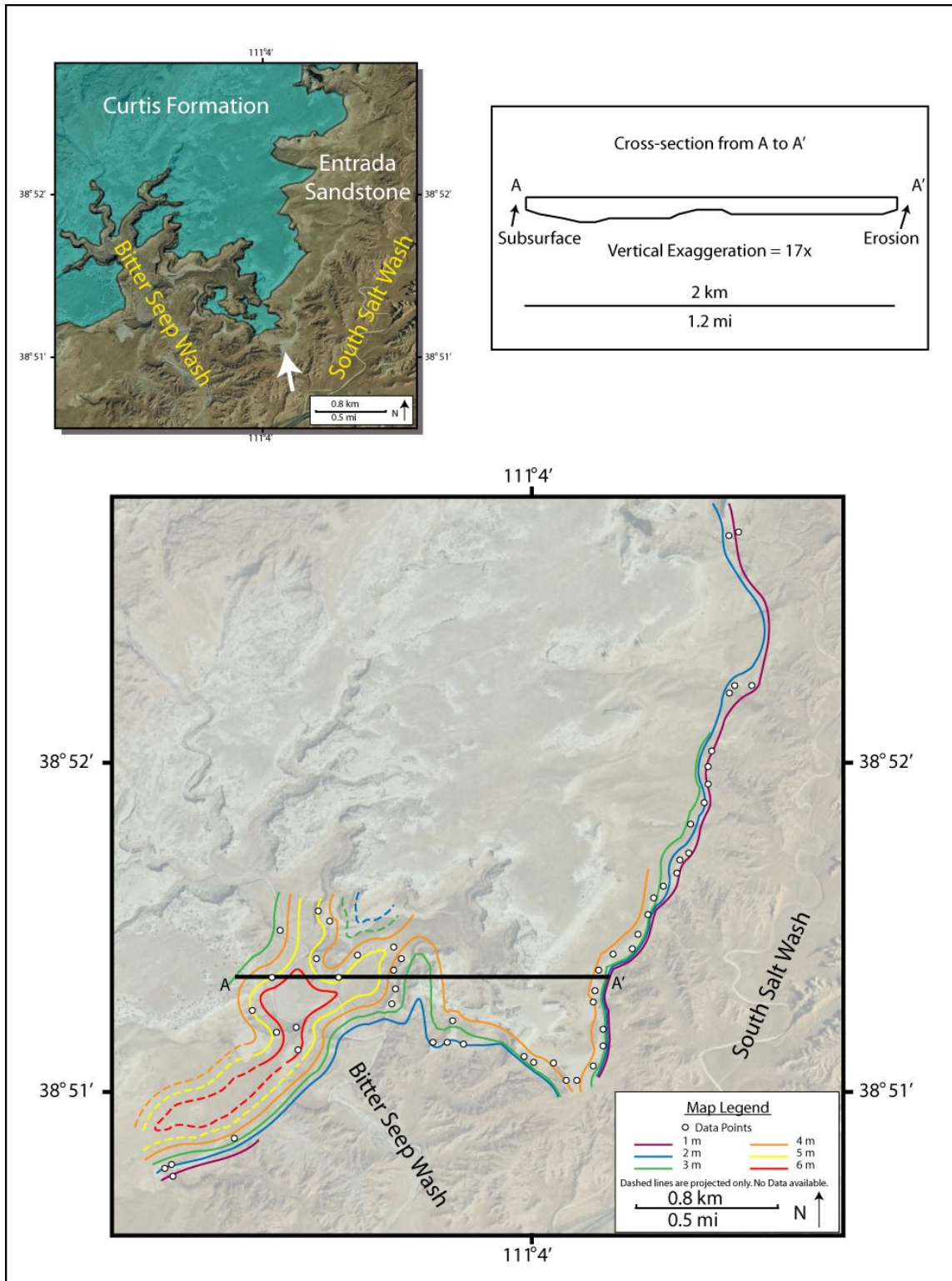
Figure 29: Isopach map overlying an aerial photo of the Bitter Seep Wash Sandstone (BSWS) in Bitter Seep Wash (left side) and South Salt Wash (right side). White arrow in upper left aerial photo points to the outcrop of the BSWS. Blue area in upper left aerial photo illustrates the overlying Curtis Formation. The uncolored area is the Entrada Sandstone. (Aerial images from Google Earth Pro-license to Morris)
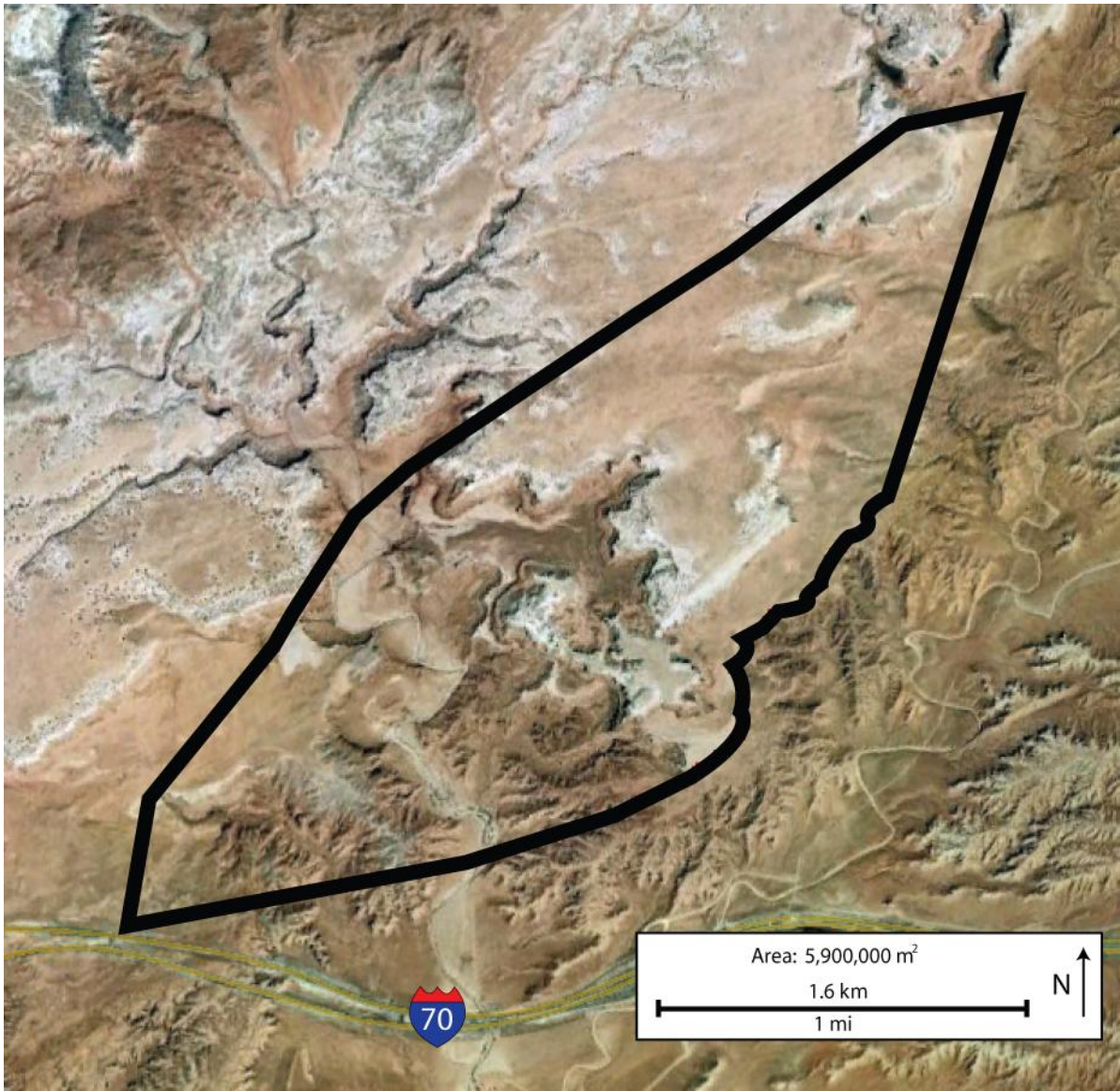
Figure 30: Black outline indicating the area used for the rough volumetric calculations on the Bitter Seep Wash Sandstone. The area was determined by connecting points where outcrop was observed. The volumetric calculation (see text) does not include eroded sandstone to the east or subsurface sandstone to the west. (Aerial image from Google Earth Pro-license to Morris).
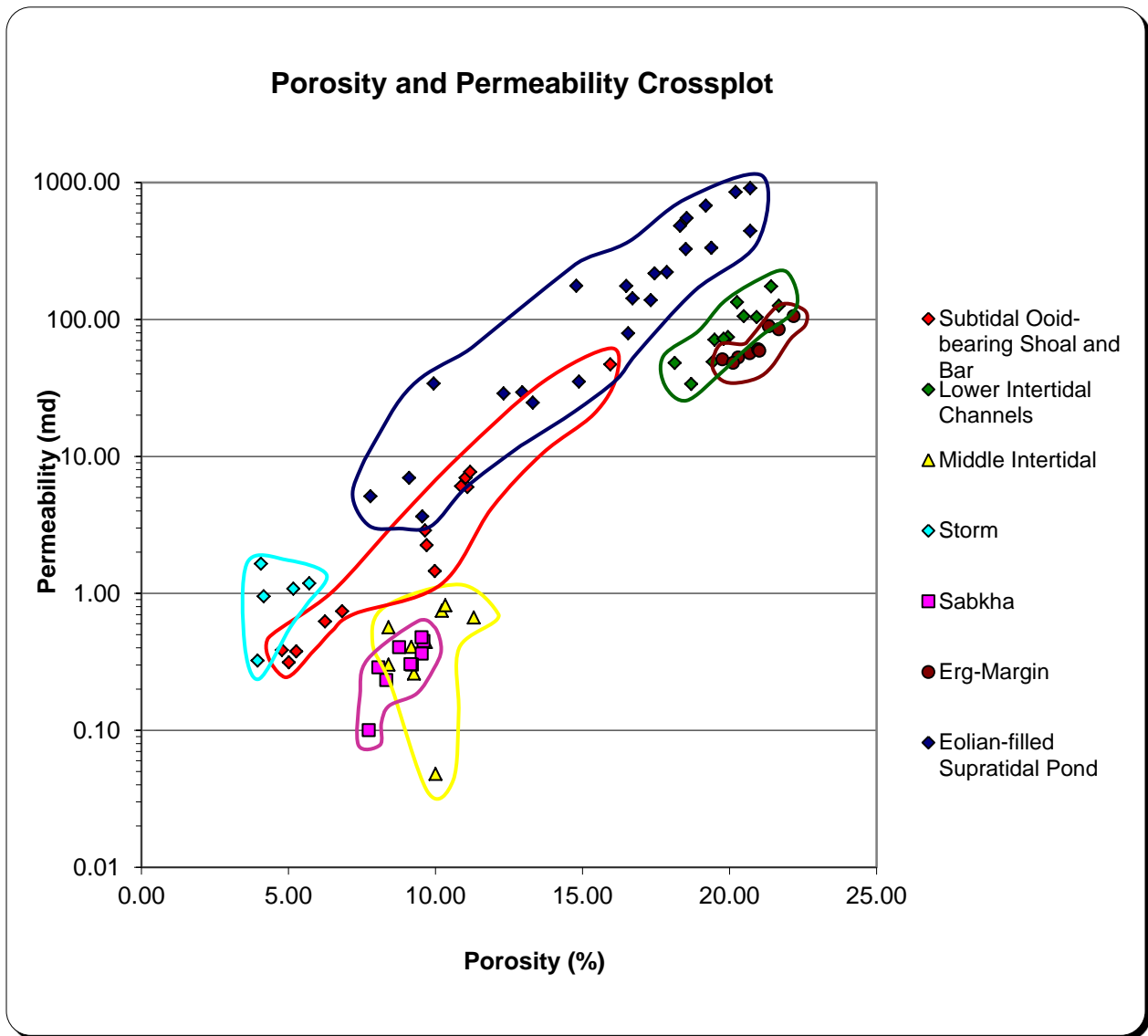
Figure 31: Porosity and permeability (at 500 psi confining pressure) crossplot of facies described in the depositional model. Note the grouping of each facies. The three best reservoir facies are the eolian-filled supratidal sabkha pond, lower intertidal channel, and the erg-margin facies. The subtidal ooid-bearing shoal and bar facies is transitional between good and poor quality reservoirs.
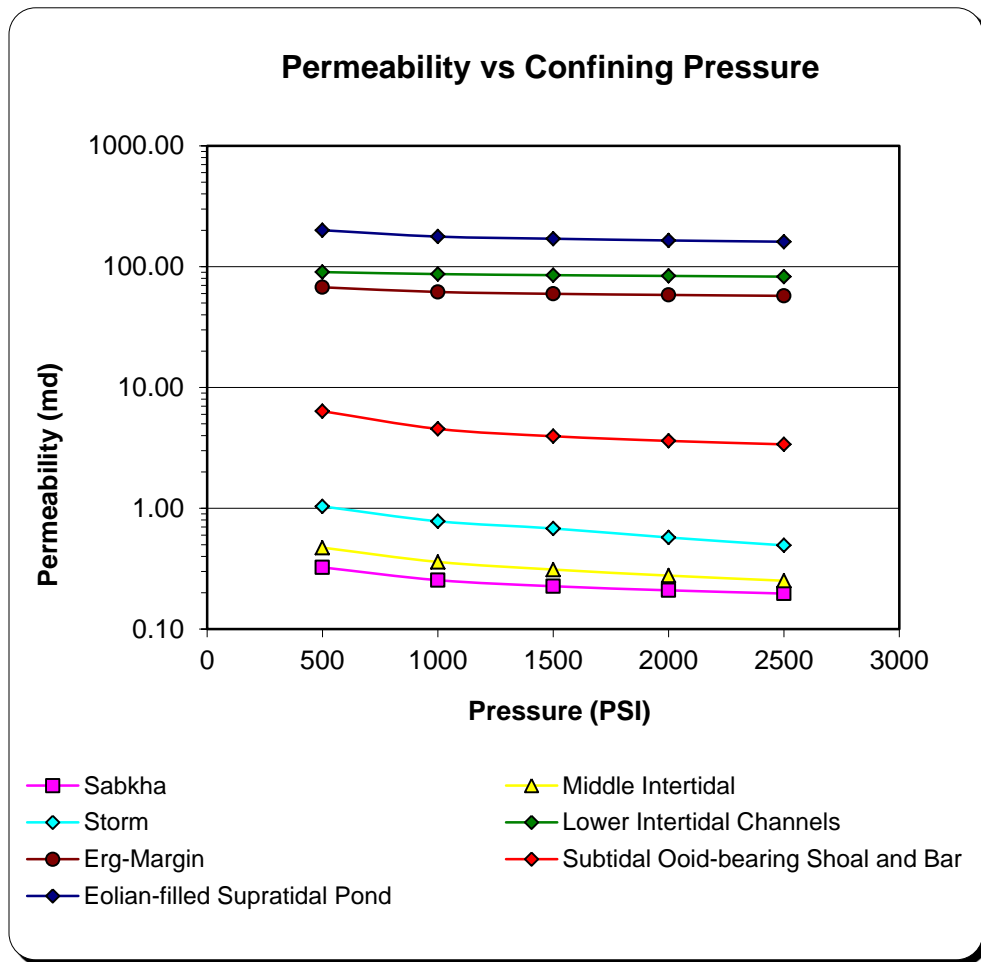
Figure 32: Graph showing the relationship between permeability and increases in pressure. Note that the slope of the line tends to decrease with each increase in pressure. This indicates that the rock likely has a limit to how much it can be compressed.

APPENDIX A
TECTONIC PROVENANCE AND THIN SECTION ANALYSIS

Appendix A includes ternary diagrams and photomicrographs for each analyzed plug. The ternary diagrams were modified from Dickinson (1979) and Dott (1964). A 300-point count was completed for each sample and that data can be found in Appendices D, E, and F.

The heading of each figure is the sample number which corresponds to the porosity and permeability data, and the point count data in Appendices C, D, E, and F.

Each ternary diagram represents different counts of different minerals. Q represents all quartzose grains including monocrystalline quartz grains (Qm), and polycrystalline quartz grains (Qp). F represents plagioclase and K-feldspar grains. P represents plagioclase. K represents K-feldspar. L represents sedimentary, metamorphic, and igneous lithics. Lt represents lithic fragments (L) and polycrystalline quartz grains (Qp).

Below the ternary diagrams are photomicrographs. There are two of each photomicrograph, one is crossed Nicols, the other is uncrossed Nicols.

The provenances are divided into three separate groups as described by Dickinson and Suczec (1979). The continental block provenance indicates sediment sources to be the shields, platforms, or faulted basement blocks. The recycled orogen provenance indicates sediment sources to be from deformed and uplifted stratal sections in subduction zones, collision orogens, or foreland fold-thrust belts. The magmatic arc provenance indicates sediments sources within active arc orogens of island arcs or active continental margins.

Sample 2-9
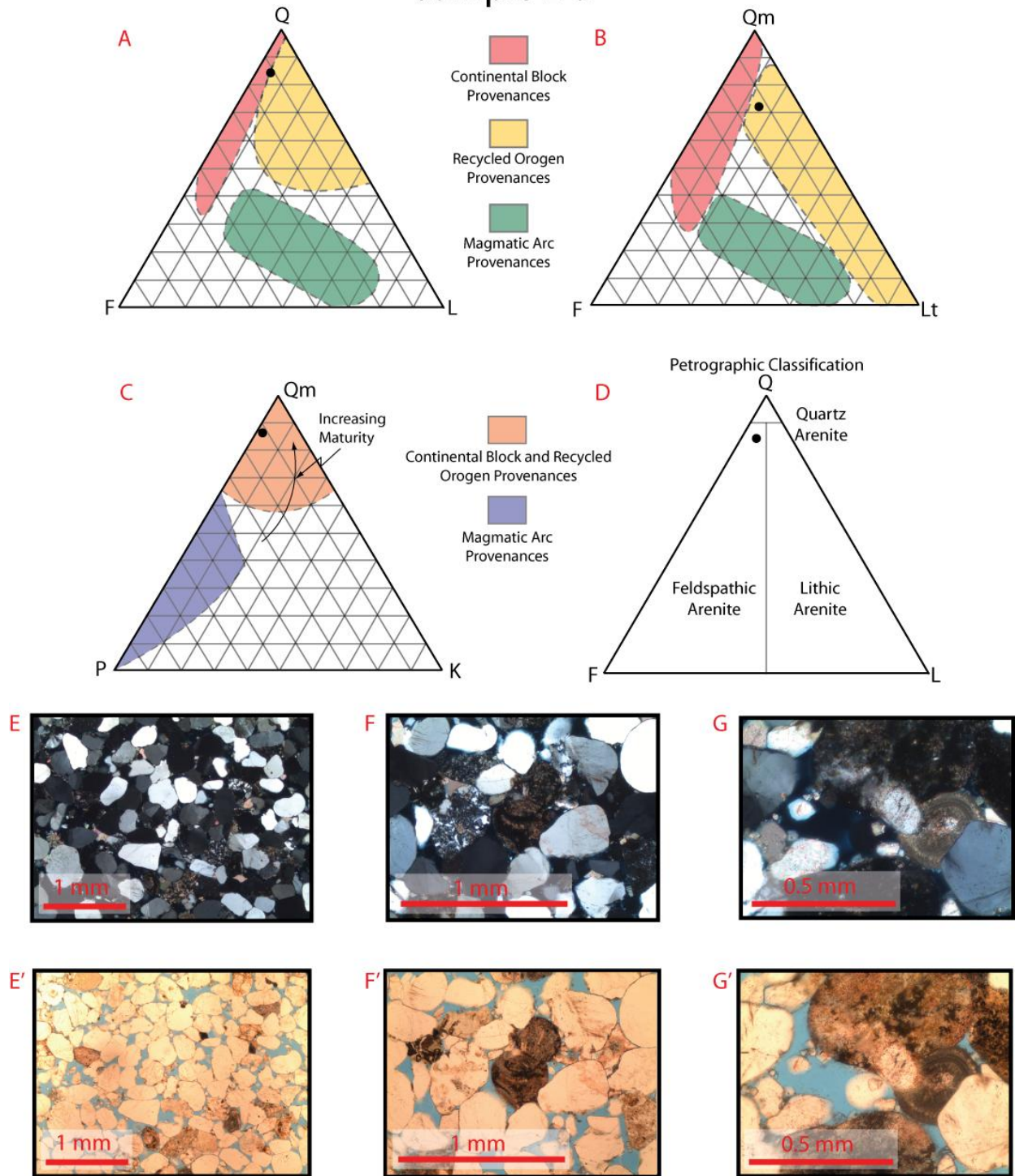
Figure A1: This figure represents the Bitter Seep Wash Sandstone found in South Salt Wash on the west flank of the San Rafael Swell. It is compositionally and texturally mature. Note the rare presence of ooid fragments (F, F', G, and G'). Also note the high porosity (17.7%). The ternary diagrams indicate the tectonic provenance to be the recycled orogen provenance.

Sample 4-4
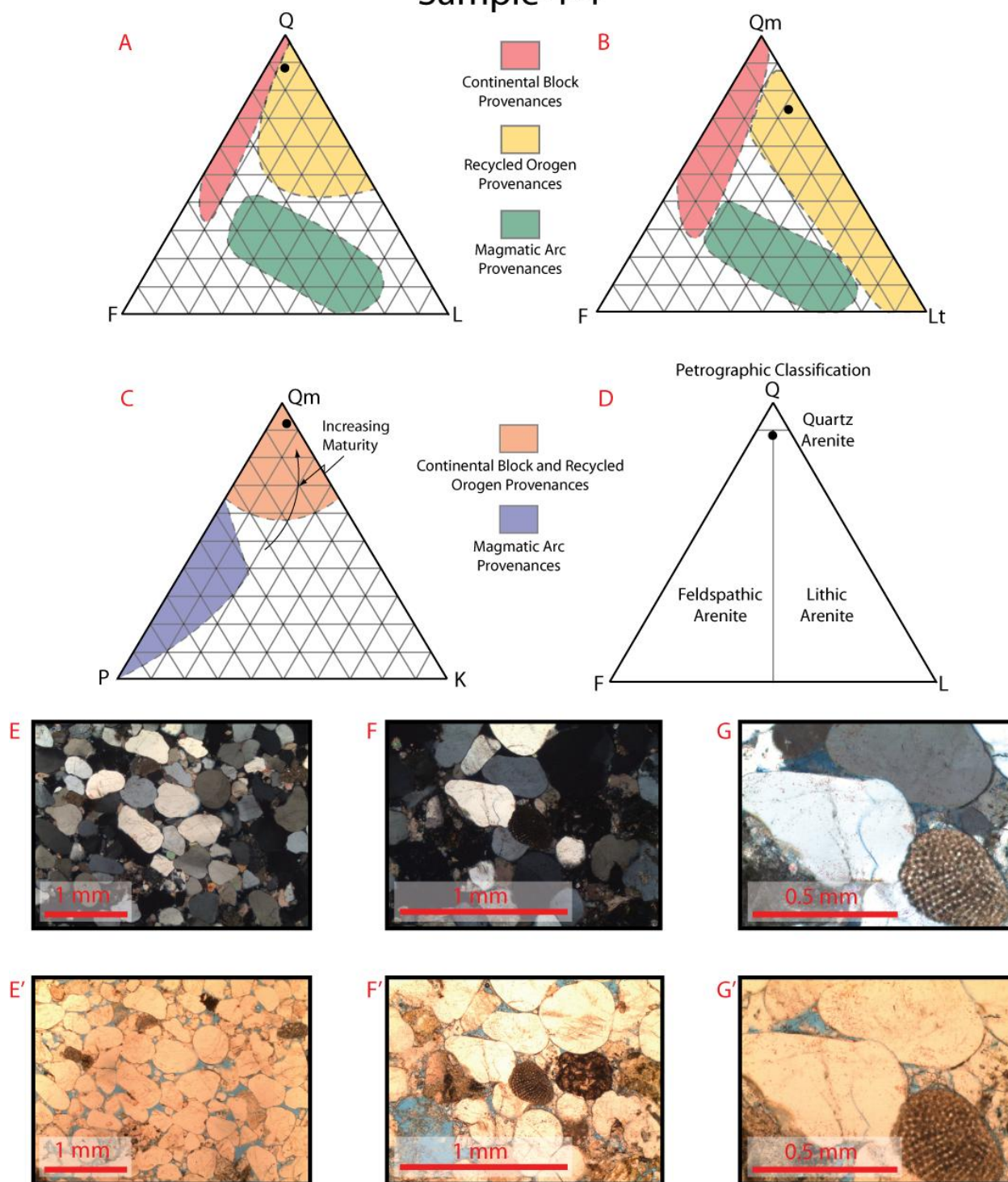
Figure A2: This figure represents the Bitter Seep Wash Sandstone found in South Salt Wash on the west flank of the San Rafael Swell. It is compositionally and texturally mature. Note the rare occurrence of echinoderm fragments (F, F', G', and G'). Again notice the high porosity (10.7%) of this facies. The ternary diagrams indicate the tectonic provenance to be the recycled orogen provenance.

Sample 9-1E
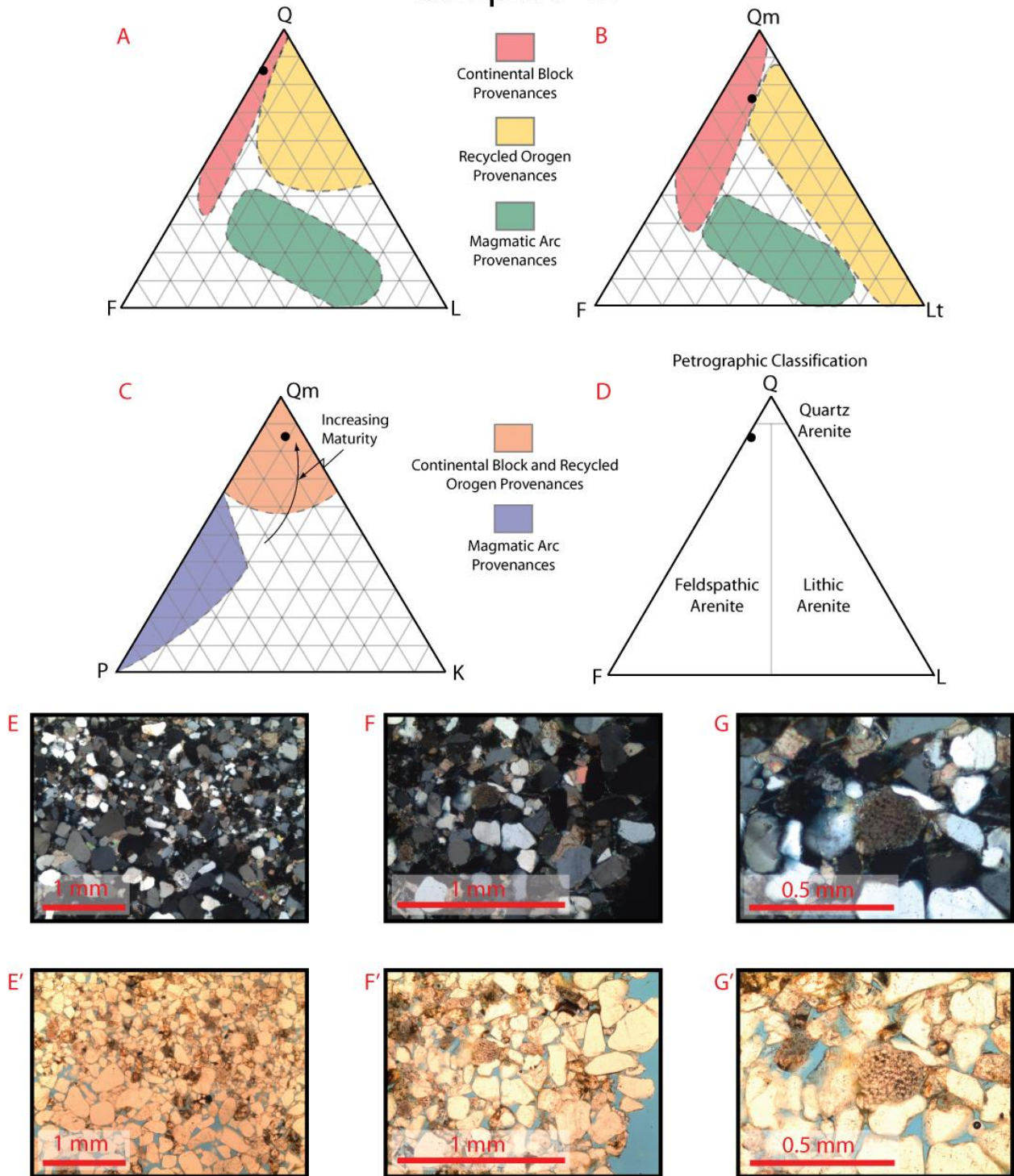
Figure A3: This sample represents the erg-margin facies. It is compositionally and texturally mature. Note the amount of porosity (14%) (E' and F'), and the rare occurrence of echinoderm fragments (G and G'). The ternary diagrams indicate the tectonic provenance to be the continental block provenance.

Sample 9-1I
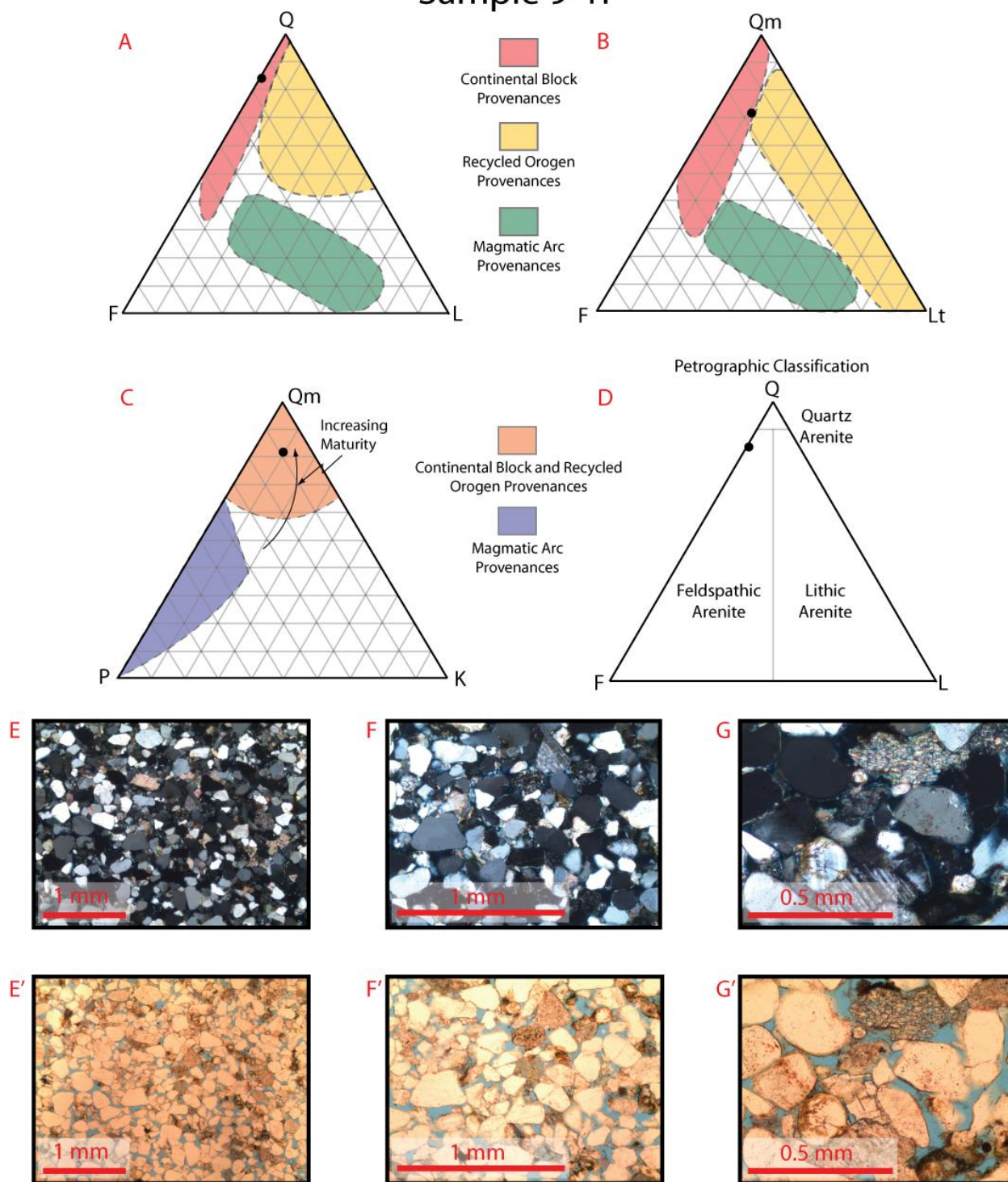
Figure A4: This sample represents the erg-margin facies. It is compositionally mature and texturally submature to mature. Note the high porosity (17.7%) (E', F', and G'), and the carbonate fragments (G and G'). The ternary diagrams indicate the tectonic provenance to be the continental block provenance.

Sample 5-1A1
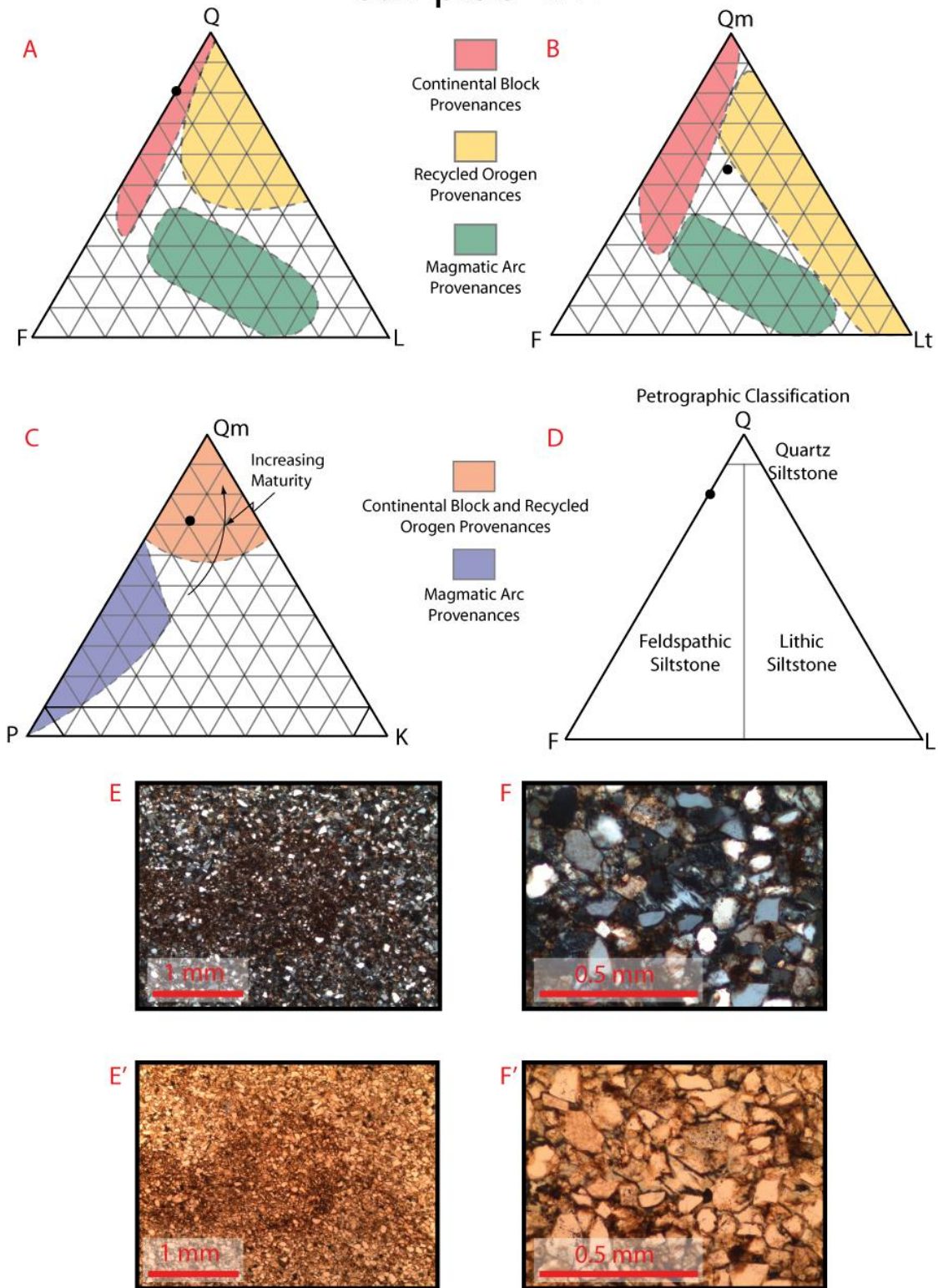
Figure A5: This sample represents the sabkha facies. This rock is compositionally immature and texturally submature. Note the dark brown area of matrix (5.7-12.3%) (E') indicative of disturbed bedding. Porosity was 1.3%. The ternary diagrams indicate the tectonic provenance to be the continental block provenance.

Sample 5-1B1
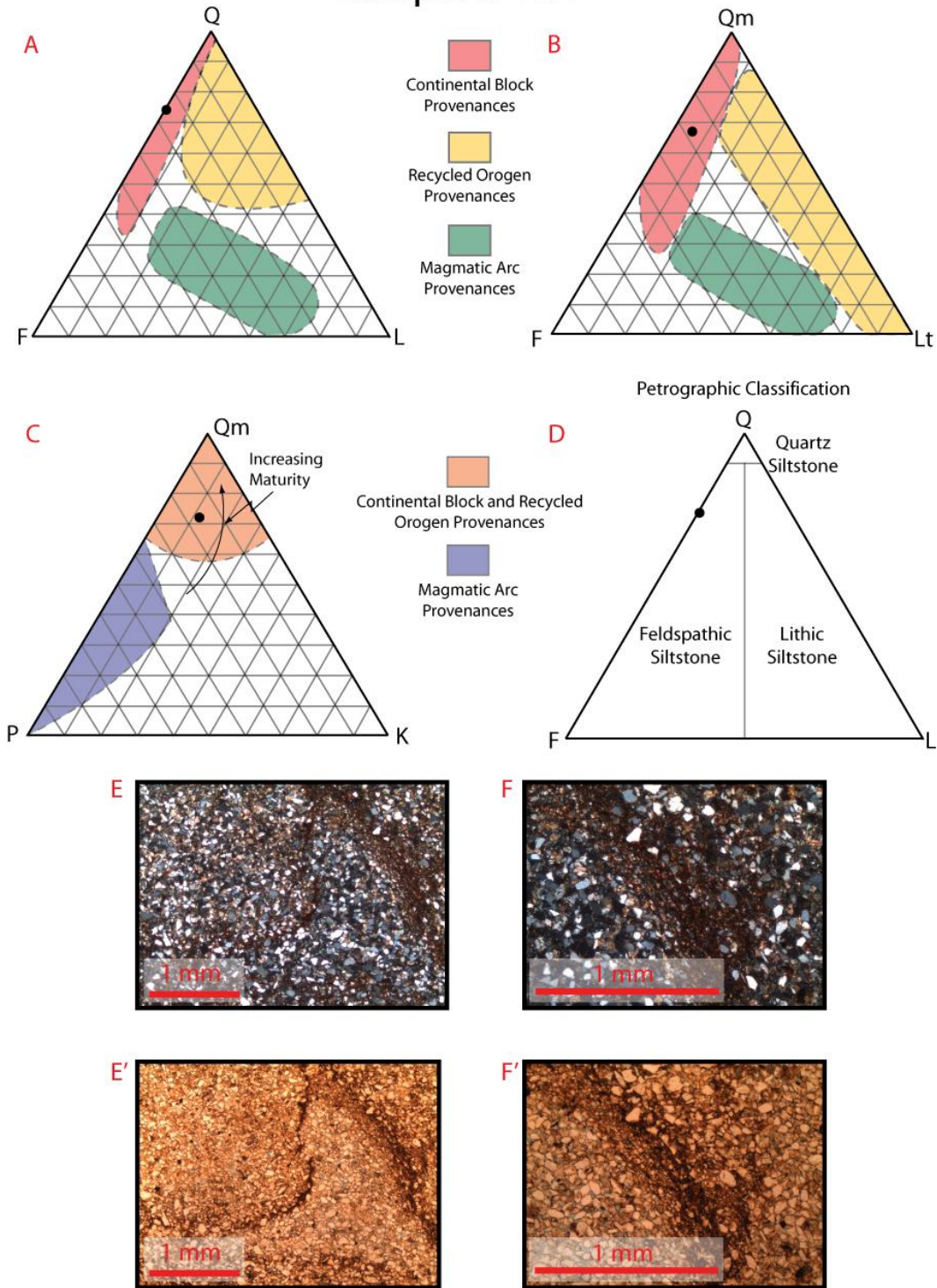
Figure A6: This sample represents the sabkha facies. This rock is compositionally immature and texturally submature. Note again the bands of matrix (E' and F') and sharp variations in grain size (F and F') that reveal disturbed bedding. Porosity was 4%. The ternary diagrams indicate the tectonic provenance to be the continental block provenance.

Sample 6-1B1
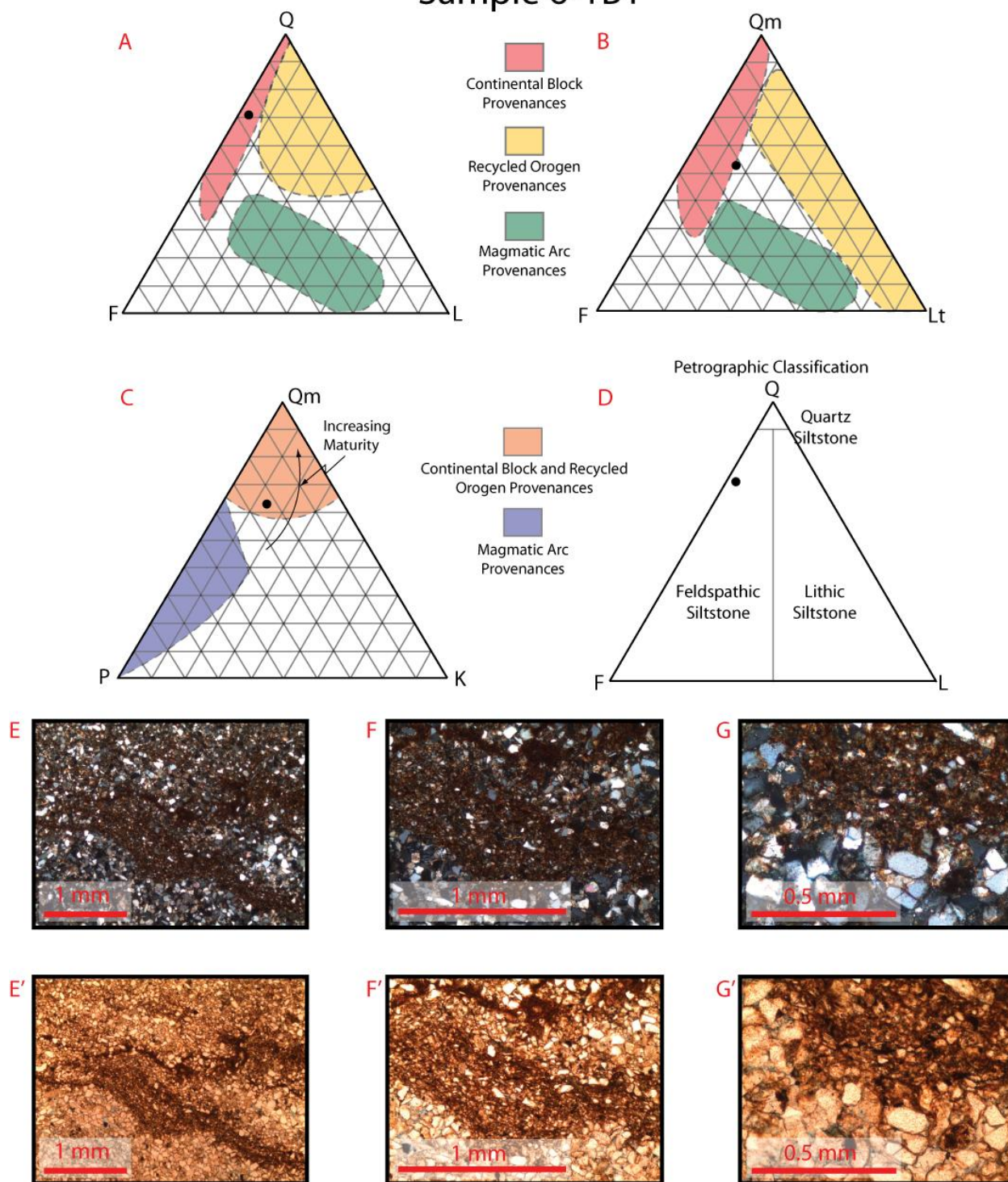
Figure A7: This sample represents the middle intertidal facies. It is compositionally immature and texturally submature. Note the bands of matrix (E' and F') revealing disturbed bedding. There are also sharp variations in grain size (G and G'). Porosity was 2.3%. The ternary diagrams indicate the tectonic provenance to be the continental block provenance.

111

Sample 6-1E2

A — Q / F / L ternary diagram with Continental Block Provenances, Recycled Orogen Provenances, and Magmatic Arc Provenances fields.

B — Qm / F / Lt ternary diagram.

Legend:
- Continental Block Provenances
- Recycled Orogen Provenances
- Magmatic Arc Provenances

C — Qm / P / K ternary diagram. Increasing Maturity.
- Continental Block and Recycled Orogen Provenances
- Magmatic Arc Provenances

D — Petrographic Classification. Q / F / L ternary diagram. Quartz Siltstone, Feldspathic Siltstone, Lithic Siltstone.

E — 1 mm

F — 1 mm

G — 0.5 mm

E' — 1 mm

F' — 1 mm

G' — 0.5 mm

Figure A8: This sample represents the middle intertidal facies. It is compositionally immature and texturally submature. Note again the bands of matrix (E' and F'). High birefringence biotite is present within the matrix bands (F and G). Porosity was 1.3%. The ternary diagrams indicate the tectonic provenance to be the continental block provenance.

112

Sample 7-1B
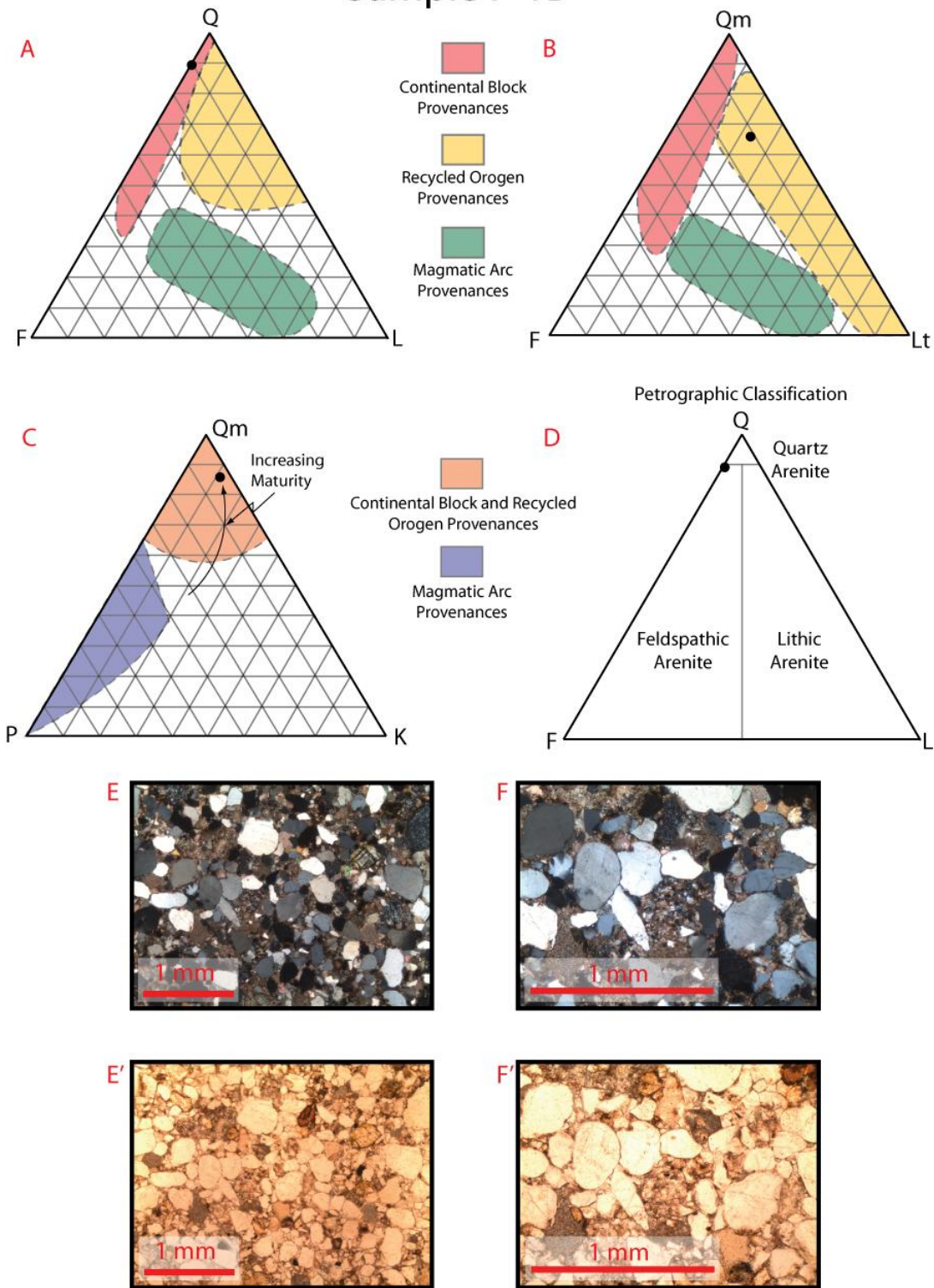
Figure A9: This sample represents the storm facies. It is compositionally mature and texturally submature. Note the low porosity (4.3%) and poor sorting (E, E', F, and F'). The ternary diagrams indicate the tectonic provenance to be either the continental block or recycled orogen provenances.

Sample 7-1E
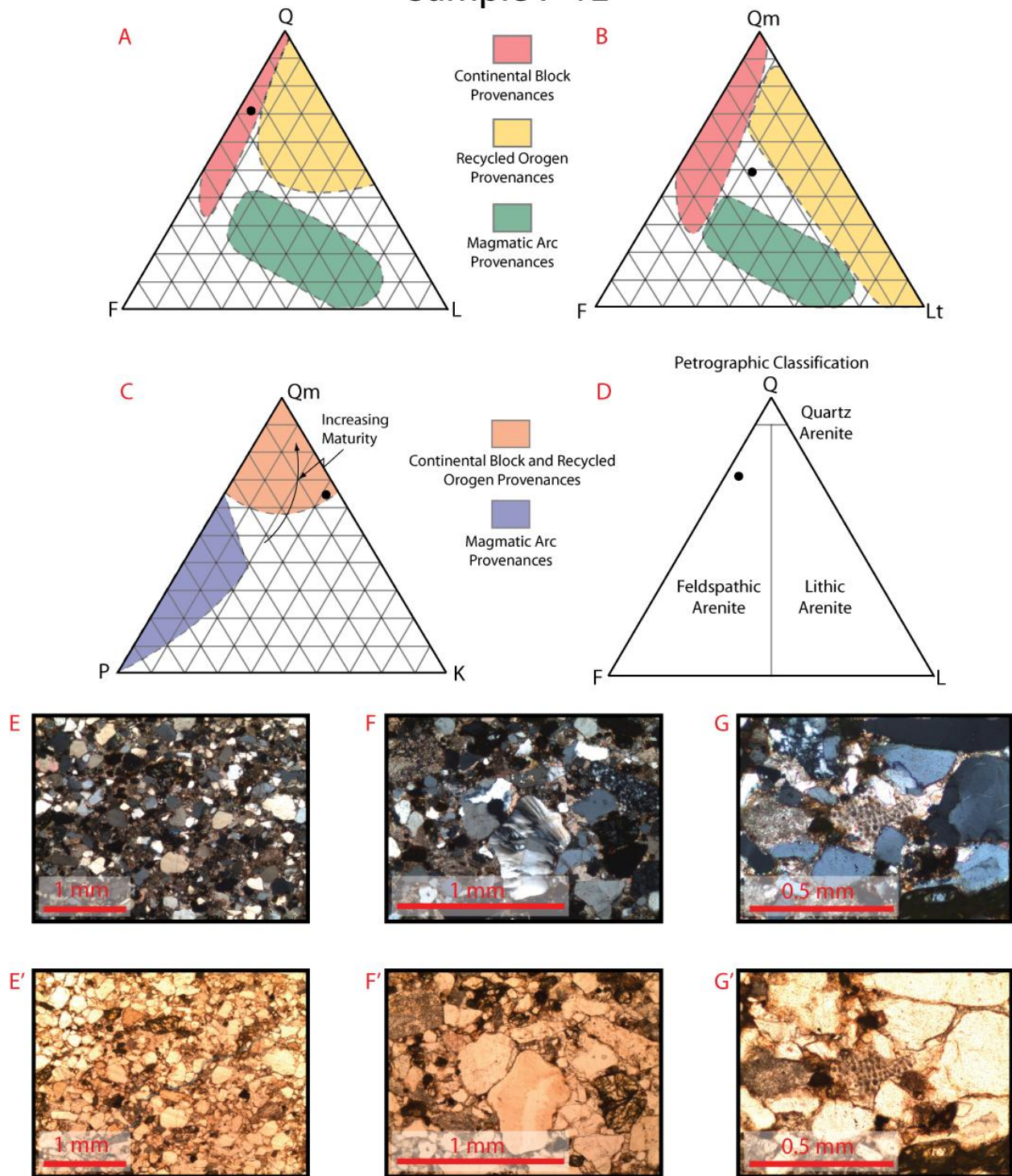
Figure A10: This sample represents the storm facies. It is compositionally mature and texturally submature. Rare echinoderm fragments are present (G and G'). Note the polycrystalline quartz (F and F') displaying deformation bands indicative of low to medium grade metamorphism (Young, 1976). The ternary diagrams indicate the tectonic provenance to be the continental block provenance.

Sample 8-1F
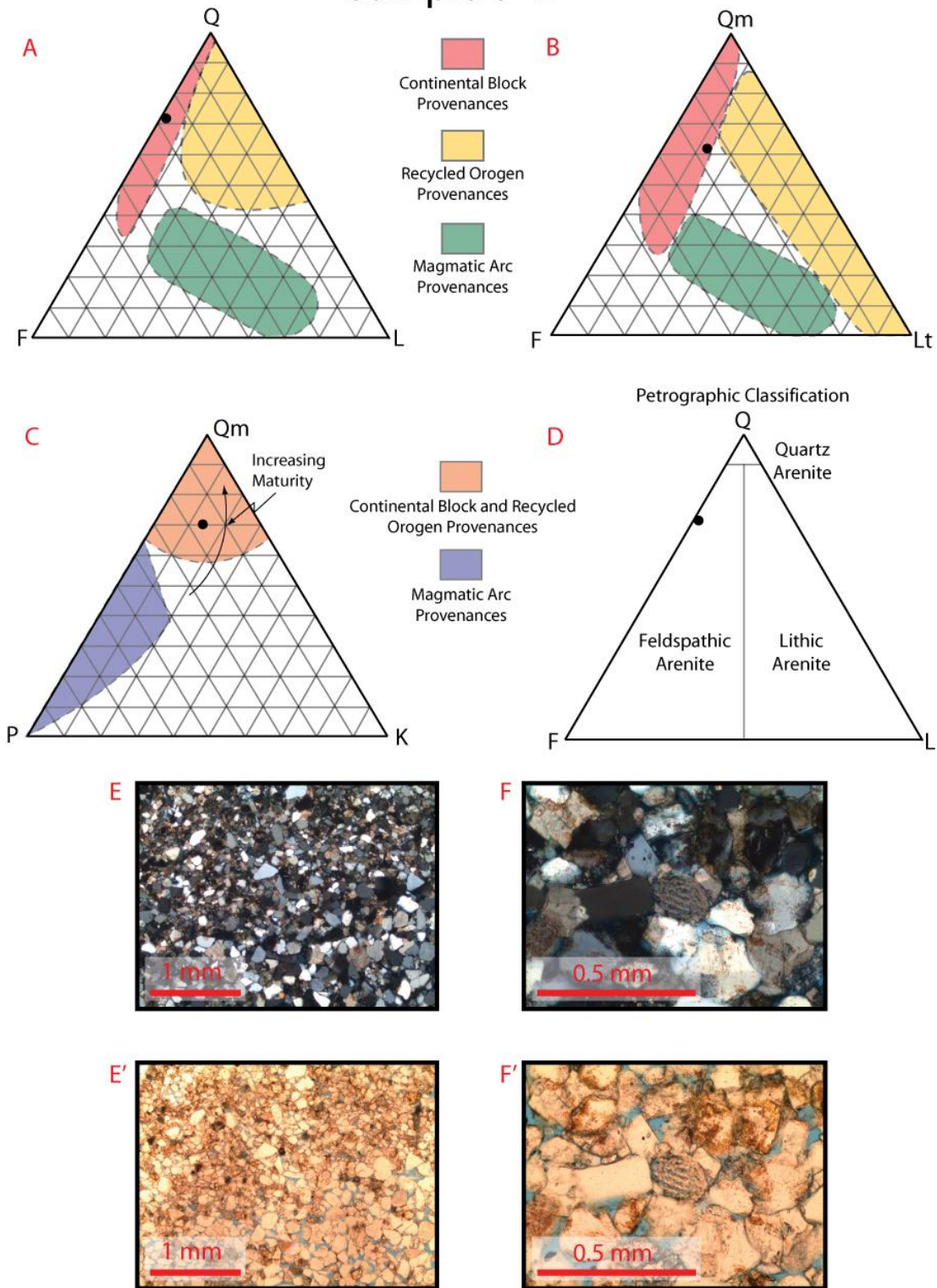
Figure A11: This sample represents the lower intertidal channel facies. It is compositionally mature and texturally submature. Rare echinoderm fragments are present (F and F'). Note the difference in grain size (E and E'). Porosity was 17.3%. The ternary diagrams indicate the tectonic provenance to be the continental block provenance.

115

Sample 8-1G2
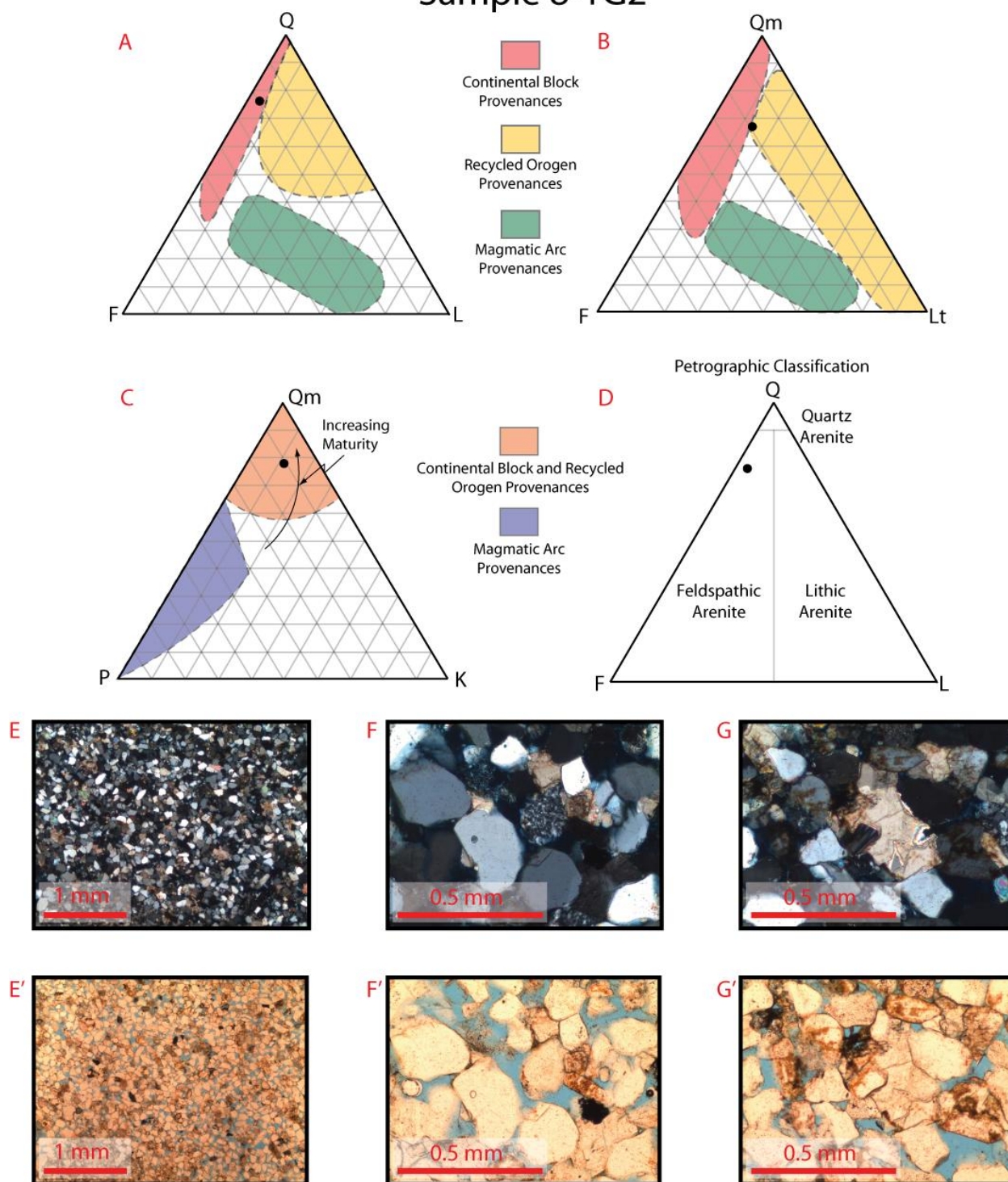
Figure A12: This sample represents the lower intertidal channel facies. It is compositionally and texturally mature. Note the calcite crystal growth (G and G') and the high amount of porosity (22.3%) (E' and F'). The ternary diagrams indicate the tectonic provenance to be the continental block provenance.

Sample 10-1A
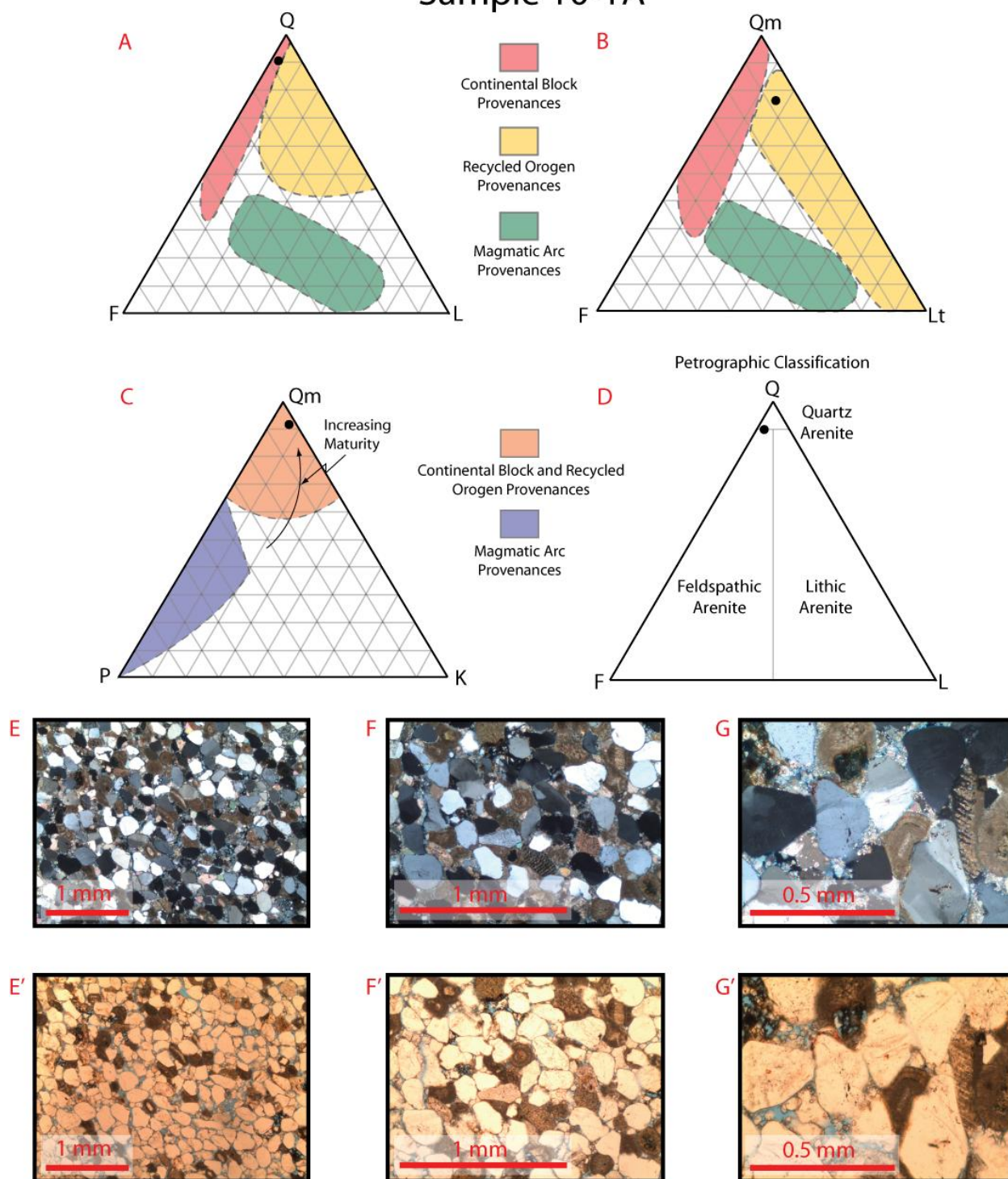
Figure A13: This sample represents the subtidal ooid-bearing shoal and bar facies. It is compositionally and texturally mature. Note the large amount of ooids (10.3%) (F and F') and rare echinoderm fragments (G, and G'). Also note the calcite growths within the interparticle porosity (F and G). Porosity was 8.3%. The ternary diagrams indicate the tectonic provenance to likely be the recycled orogen provenance.

Sample 10-1C2
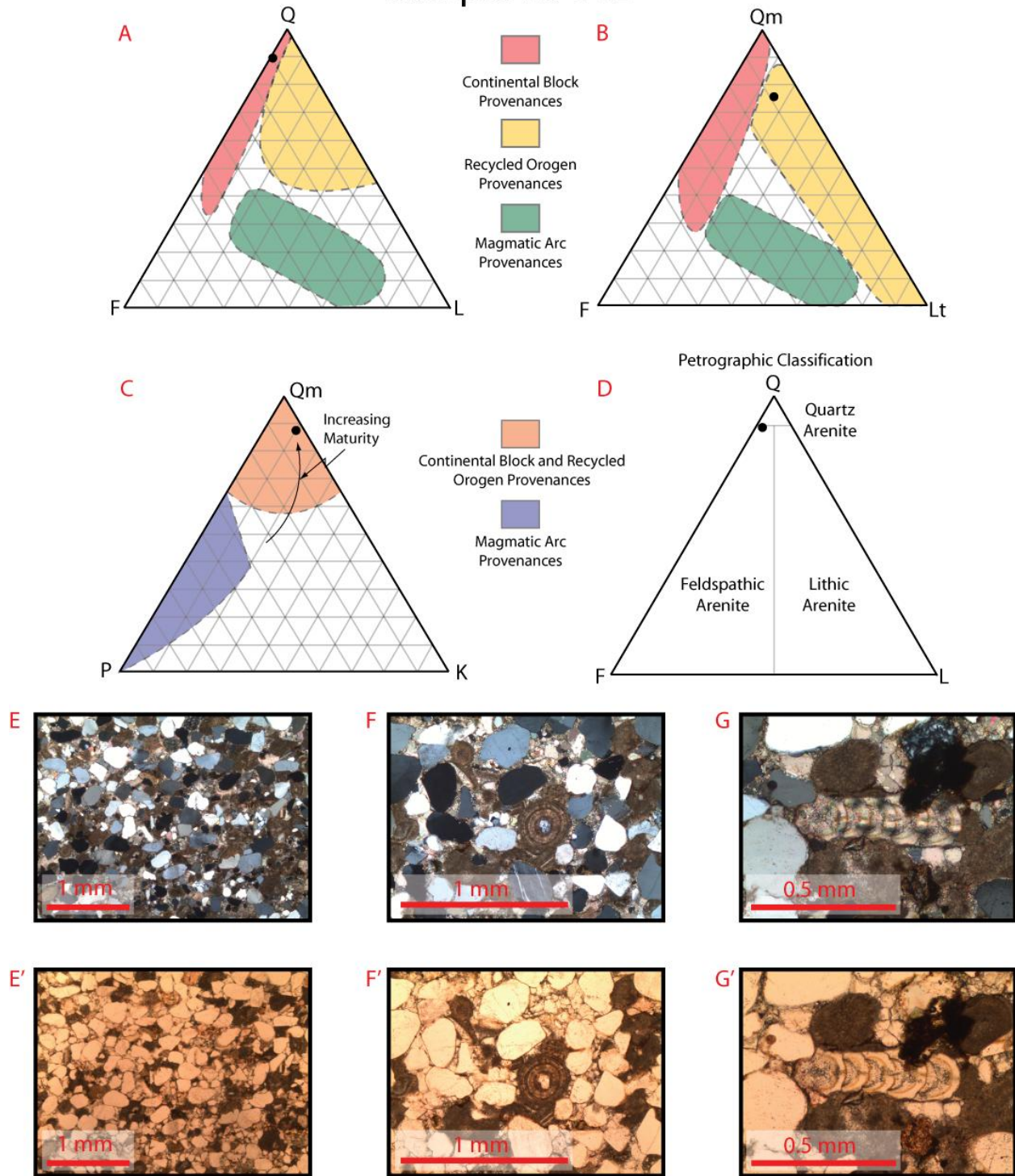
Figure A14: This sample represents the subtidal ooid-bearing shoal and bar facies. It is compositionally and texturally mature. Note the ooids (13.7%) (F and F'), uniserial foram (G and G'), and the relatively low porosity (0%). The ternary diagrams indicate the tectonic provenance to be either the continental block provenance or the recycled orogen provenance.

APPENDIX B
POROSITY AND PERMEABILITY DATA

Table B1: Porosity and permeability data collected from the seven facies identified in the Entrada Sandstone.

Facies	Sample	Avg. Perm (md) 500 PSI	1000 PSI	1500 PSI	2000 PSI	2500 PSI	Average Porosity (%)	
	1-2	3.65	2.93	2.66	2.51	2.41	9.55	
	1-4	175.50	145.50	135	129.00	124.50	16.49	
	1-5	910.20	860.00	826.5	807.00	789.00	20.71	
	1-7	222.00	166.50	213.5	202.50	195.00	17.87	
	1-12	217.00	175.50	164.5	160.00	156.00	17.45	
	1-13	79.30	56.80	49.45	45.70	43.00	16.55	
	Location 1 Avg.	**267.94**	**234.54**	**231.94**	**224.45**	**218.32**	**16.44**	
	2-3	34.10	30.35	28.65	27.60	26.80	9.94	
	2-4	176.00	168.00	156.5	150.00	146.00	14.79	
	2-6	333.67	284.00	262.5	252.00	244.50	19.38	
	2-7	550.67	491.50	466.5	452.50	441.00	18.55	
	2-8B	677.33	595.50	565	545.50	533.00	19.19	
Bitter Seep Wash Sandstone	2-9	443.00	394.50	374	362.50	355.50	20.71	*
	2-12	852.67	760.00	722	700.50	683.50	20.21	
	2-13	327.00	294.00	280.5	272.50	266.00	18.51	
	2-14	482.67	421.50	396.5	383.50	373.50	18.32	
	Location 2 Avg.	**430.79**	**382.15**	**361.35**	**349.62**	**341.09**	**17.73**	
	3-2	29.37	27.45	26.6	26.10	25.65	12.95	
	3-3	28.80	26.40	25.3	24.60	23.95	12.32	
	3-4	142.67	133.00	127	123.50	120.00	16.70	
	3-7	35.13	27.10	23.85	22.15	27.65	14.88	
	Location 3 Avg.	**58.99**	**53.49**	**50.69**	**49.09**	**49.31**	**14.21**	
	4-1	5.12	4.22	3.87	3.67	3.53	7.79	
	4-2	6.96	6.23	5.57	5.06	4.66	9.10	
	4-4	24.67	19.30	17.05	15.80	14.95	13.31	*
	4-6	138.33	129.00	124	120.50	117.00	17.32	
	Location 4 Avg.	**43.77**	**39.69**	**37.62**	**36.26**	**35.03**	**11.88**	
	5-1A1	0.10	0.06	0.0445	0.03	0.03	7.73	*
	5-1A2	0.36	0.27	0.2295	0.21	0.19	9.54	
Sabkha	5-1B1	0.45	0.37	0.346	0.32	0.30	9.60	*
	5-1C	0.40	0.32	0.2765	0.25	0.23	8.77	
	5-1D	0.23	0.18	0.1555	0.15	0.14	8.33	

Sabkha	5-1E	0.48	0.40	0.3705	0.35	0.34	9.53
	5-1F	0.29	0.23	0.204	0.19	0.18	8.06
	5-1G1	0.30	0.22	0.1965	0.18	0.17	9.21
	5-1G2	0.30	0.24	0.2155	0.20	0.19	9.15
	Sabkha Avg.	**0.32**	**0.25**	**0.23**	**0.21**	**0.20**	**8.88**
Middle Intertidal	6-1A1	0.41	0.24	0.1775	0.15	0.12	9.18	
	6-1A2	0.26	0.16	0.132	0.11	0.10	9.27	
	6-1B1	0.57	0.46	0.414	0.39	0.36	8.41	*
	6-1B2	0.30	0.21	0.1675	0.15	0.13	8.41	
	6-1D	0.75	0.61	0.554	0.50	0.45	10.22	
	6-1E1	0.82	0.66	0.591	0.53	0.48	10.34	
	6-1E2	0.67	0.55	0.4765	0.43	0.39	11.31	*
	6-1F1	0.44	0.31	0.261	0.23	0.209	9.67	
	6-1F2	0.05	0.033	0.0275	0.0245	0.0225	10.00	
	Middle Intertidal Avg.	**0.47**	**0.36**	**0.31**	**0.28**	**0.25**	**9.64**	
Storm Facies	7-1B	1.18	0.669	0.7675	0.611	0.506	5.71	*
	7-1D	1.08	1.085	0.794	0.6415	0.521	5.17	
	7-1E	0.32	0.213	0.1605	0.132	0.113	3.95	*
	7-1F1	0.95	0.8305	0.74	0.6695	0.613	4.16	
	7-1F2	1.65	1.11	0.943	0.8135	0.716	4.07	
	Storm Avg.	**1.04**	**0.78**	**0.68**	**0.57**	**0.49**	**4.61**	
Lower-intertidal Channels	8-1A	49.10	47.15	46.15	45.45	44.75	19.43	
	8-1B	104.00	97.55	95.3	93.75	92.5	20.92	
	8-1C1	126.00	121	118	117	115.5	21.68	
	8-1C2	105.67	102	100	99	97.85	20.48	
	8-1D1	74.37	72.3	70.75	69.55	68.6	19.95	
	8-1D2	71.23	68.45	66.95	65.85	65	19.49	
	8-1E1	133.67	126.5	124	122	120	20.26	
	8-1F	48.13	45.9	44.85	44.15	43.55	18.14	*
	8-1G1	33.80	32.05	32	30.8	30.4	18.70	
	8-1G2	174.33	174	171	169	167	21.41	*
	8-1H	72.20	68.4	66.85	65.75	64.95	19.80	
	Lower Intertidal Channel Avg.	**90.23**	**86.85**	**85.08**	**83.85**	**82.74**	**20.02**	
Erg-Margin	9-1A	52.70	47.9	45.85	44.4	43.25	20.30	
	9-1B	56.57	51.6	49.75	48.6	48	20.69	

Erg-Margin	9-1C	89.10	83.85	82.5	81.2	80	21.34	
	9-1D	60.57	53.9	51.5	50.25	49.65	20.98	
	9-1E	51.13	46.2	44.3	43.2	42.3	19.76	*
	9-1F	48.10	42.85	40.9	39.55	38.65	20.12	
	9-1H	84.80	79.75	77.9	77.55	76.75	21.68	
	9-1I	105.67	95.95	91.75	89.1	87	22.18	*
	9-1J	59.10	53.8	52.1	51.35	50.7	21.02	
	Erg-Margin Avg.	**67.53**	**61.76**	**59.62**	**58.36**	**57.37**	**20.90**	
Subtidal Ooid-bearing Shoal and Bar	10-1A	46.98	28.75	22.85	19.55	17.3	15.95	*
	10-1C1	0.62	0.348	0.2825	0.2505	0.2255	6.25	
	10-1C2	0.39	0.2525	0.2135	0.189	0.1705	4.78	*
	10-1D	0.38	0.2605	0.2235	0.201	0.186	5.27	
	10-1E	0.31	0.222	0.1925	0.1715	0.159	5.01	
	10-1F	5.98	5.11	4.815	4.66	4.545	11.09	
	10-1G	2.25	1.865	1.81	1.75	1.685	9.70	
	10-1I	1.46	1.245	1.18	1.12	1.195	9.98	
	10-1J1	2.88	2.465	2.285	2.195	2.1	9.64	
	10-1J2	6.99	6.295	6.04	5.885	5.765	11.03	
	10-1K1	6.06	4.98	4.65	4.47	4.35	10.87	
	10-1K2	7.72	6.63	6.19	5.94	5.735	11.18	
	10-1M	0.74	0.6515	0.6185	0.6005	0.5855	6.83	
	Subtidal Ooid - bearing Shoal and Bar Avg.	**6.36**	**4.54**	**3.95**	**3.61**	**3.38**	**9.04**	

* indicates thin sectioned plug

APPENDIX C
POINT COUNT DATA FOR QFL TERNARY DIAGRAMS

       To properly classify and understand the tectonic provenance 300-point counts were completed on each thin section (two from each facies). Q represents all quartzose grains including monocrystalline quartz grains (Qm), and polycrystalline quartz grains (Qp). F represents plagioclase and K-feldspar grains. L represents sedimentary, metamorphic, and igneous lithics.

Table C1: Point count data collected for QFL ternary plots for each of the studied facies.

2-9 (Bitter Seep Wash Sandstone)			4-4 (Bitter Seep Wash Sandstone)			5-1A1 (Sabkha)		
Mineral	Counts	% Tot.	Mineral	Counts	% Tot.	Mineral	Counts	% Tot.
Mono	155	51.7	Mono	152	50.7	Mono	98	32.7
Coarse Poly	25	8.3	Coarse Poly	17	5.7	Coarse Poly	36	12.0
Fine Poly	3	1.0	Fine Poly	9	3.0	Fine Poly		0.0
Microcrystalline			Microcrystalline	6	2.0	Microcrystalline	2	0.7
Undulose	8	2.7	Undulose	20	6.7	Undulose	33	11.0
Plagioclase	21	7.0	Plagioclase	4	1.3	Plagioclase	26	8.7
K-Feldspar	5	1.7	K-Feldspar	9	3.0	K-Feldspar	14	4.7
Calcite Cement	4	1.3	Calcite Cement	24	8.0	Calcite Cement	28	9.3
Quartz Cement	2	0.7	Quartz Cement			Quartz Cement		
Poikilotropic Cement			Poikilotropic Cement			Poikilotropic Cement		
Interpartical Porosity	53	17.7	Interpartical Porosity	32	10.7	Interpartical Porosity	4	1.3
Intrapartical Porosity	3	1.0	Intrapartical Porosity			Intrapartical Porosity		
Igneous Lithic			Igneous Lithic	6	2.0	Igneous Lithic		
Sedimentary Lithic	7	2.3	Sedimentary Lithic	7	2.3	Sedimentary Lithic		
Metamorphic Lithic			Metamorphic Lithic			Metamorphic Lithic		
Calcite	13	4.3	Calcite	10	3.3	Calcite	18	6.0
Fe Oxide	1	0.3	Fe Oxide	2	0.7	Fe Oxide	5	1.7
						Gypsum	13	4.3
Clay Rims			Clay Rims			Clay Rims		
Matrix			Matrix	2	0.7	Matrix	23	7.7
Total Counts	300		Total Counts	300		Total Counts	300	
Total Quartz	191		Total Quartz	204		Total Quartz	169	
Total Feldspars	26		Total Feldspars	13		Total Feldspars	40	
Total Lithics	7		Total Lithics	13		Total Lithics	0	
Total	224		Total	230		Total	209	
Norm. Qtz	85.3		Norm. Qtz	88.7		Norm. Qtz	80.9	
Norm. Feldspars	11.6		Norm. Feldspars	5.7		Norm. Feldspars	19.1	
Norm. Lithics	3.1		Norm. Lithics	5.7		Norm. Lithics	0.0	

5-1B1 (Sabkha)		
Mineral	Counts	% Tot.
Mono	117	39.0
Coarse Poly	9	3.0
Fine Poly	1	0.3
Microcrystalline	1	0.3
Undulose	12	4.0
Plagioclase	28	9.3
K-Feldspar	19	6.3
Calcite Cement	49	16.3
Quartz Cement		
Poikilotropic Cement		
Interpartical Porosity	12	4.0
Intrapartical Porosity		
Igneous Lithic		
Sedimentary Lithic		
Metamorphic Lithic		
Calcite	5	1.7
Fe Oxide	7	2.3
Gypsum	3	1.0
Clay Rims		
Matrix	37	12.3
Total Counts	300	
Total Quartz	140	
Total Feldspars	47	
Total Lithics	0	
Total	187	
Norm. Qtz	74.9	
Norm. Feldspars	25.1	
Norm. Lithics	0.0	

6-1B1 (Middle Intertidal)		
Mineral	Counts	% Tot.
Mono	86	28.7
Coarse Poly	19	6.3
Fine Poly	7	2.3
Microcrystalline	1	0.3
Undulose	19	6.3
Plagioclase	32	10.7
K-Feldspar	19	6.3
Calcite Cement	63	21.0
Quartz Cement		
Poikilotropic Cement		
Interpartical Porosity	7	2.3
Intrapartical Porosity		
Igneous Lithic		
Sedimentary Lithic		
Metamorphic Lithic		
Calcite	4	1.3
Fe Oxide	6	2.0
Gypsum	2	0.7
Clay Rims		
Matrix	35	11.7
Total Counts	300	
Total Quartz	132	
Total Feldspars	51	
Total Lithics	0	
Total	183	
Norm. Qtz	72.1	
Norm. Feldspars	27.9	
Norm. Lithics	0.0	

6-1E2 (Middle Intertidal)		
Mineral	Counts	% Tot.
Mono	92	30.7
Coarse Poly	33	11.0
Fine Poly	4	1.3
Microcrystalline	1	0.3
Undulose	2	0.7
Plagioclase	25	8.3
K-Feldspar	34	11.3
Calcite Cement	38	12.7
Quartz Cement		
Poikilotropic Cement		
Interpartical Porosity	4	1.3
Intrapartical Porosity		
Igneous Lithic		
Sedimentary Lithic		
Metamorphic Lithic		
Calcite		
Fe Oxide	5	1.7
Clay Rims		
Matrix	62	20.7
Total Counts	300	
Total Quartz	132	
Total Feldspars	59	
Total Lithics	0	
Total	191	
Norm. Qtz	69.1	
Norm. Feldspars	30.9	
Norm. Lithics	0.0	

7-1B (Storm)		
Mineral	Counts	% Tot.
Mono	132	44.0
Coarse Poly	24	8.0
Fine Poly	4	1.3
Microcrystalline	15	5.0
Undulose	7	2.3
Plagioclase	5	1.7
K-Feldspar	17	5.7
Calcite Cement	81	27.0
Quartz Cement		
Poikilotropic Cement	13	4.3
Interpartical Porosity	1	0.3
Intrapartical Porosity		
Igneous Lithic		
Sedimentary Lithic		
Metamorphic Lithic		
Calcite		
Fe Oxide	1	0.3
Clay Rims		
Matrix		
Total Counts	300	
Total Quartz	182	
Total Feldspars	22	
Total Lithics	0	
Total	204	
Norm. Qtz	89.2	
Norm. Feldspars	10.8	
Norm. Lithics	0.0	

7-1E (Storm)		
Mineral	Counts	% Tot.
Mono	101	33.7
Coarse Poly	25	8.3
Fine Poly	9	3.0
Microcrystalline	12	4.0
Undulose	7	2.3
Plagioclase	6	2.0
K-Feldspar	49	16.3
Calcite Cement	73	24.3
Quartz Cement		
Poikilotropic Cement	14	4.7
Interpartical Porosity		
Intrapartical Porosity		
Igneous Lithic	2	0.7
Sedimentary Lithic		
Metamorphic Lithic		
Calcite		
Fe Oxide	2	0.7
Clay Rims		
Matrix		
Total Counts	300	
Total Quartz	154	
Total Feldspars	55	
Total Lithics	2	
Total	211	
Norm. Qtz	73.0	
Norm. Feldspars	26.1	
Norm. Lithics	0.9	

8-1F (Lower Intertidal Channels)		
Mineral	Counts	% Tot.
Mono	118	39.3
Coarse Poly	20	6.7
Fine Poly	1	0.3
Microcrystalline		
Undulose	2	0.7
Plagioclase	26	8.7
K-Feldspar	23	7.7
Calcite Cement	52	17.3
Quartz Cement		
Poikilotropic Cement		
Interpartical Porosity	52	17.3
Intrapartical Porosity		
Igneous Lithic	4	1.3
Sedimentary Lithic		
Metamorphic Lithic		
Calcite	1	0.3
Fe Oxide		
Clay Rims	1	0.3
Matrix		
Total Counts	300	
Total Quartz	141	
Total Feldspars	49	
Total Lithics	4	
Total	194	
Norm. Qtz	72.7	
Norm. Feldspars	25.3	
Norm. Lithics	2.1	

8-1G2 (Lower Intertidal Channels)		
Mineral	Counts	% Tot.
Mono	128	42.7
Coarse Poly	15	5.0
Fine Poly	4	1.3
Microcrystalline	1	0.3
Undulose	3	1.0
Plagioclase	18	6.0
K-Feldspar	19	6.3
Calcite Cement	38	12.7
Quartz Cement		
Poikilotropic Cement		
Interpartical Porosity	67	22.3
Intrapartical Porosity		
Igneous Lithic	7	2.3
Sedimentary Lithic		
Metamorphic Lithic		
Calcite		
Fe Oxide		
Clay Rims		
Matrix		
Total Counts	300	
Total Quartz	151	
Total Feldspars	37	
Total Lithics	7	
Total	195	
Norm. Qtz	77.4	
Norm. Feldspars	19.0	
Norm. Lithics	3.6	

9-1E (Erg-margin)		
Mineral	Counts	% Tot.
Mono	159	53.0
Coarse Poly	14	4.7
Fine Poly	4	1.3
Microcrystalline	1	0.3
Undulose	1	0.3
Plagioclase	11	3.7
K-Feldspar	18	6.0
Calcite Cement	44	14.7
Quartz Cement		
Poikilotropic Cement		
Interpartical Porosity	42	14.0
Intrapartical Porosity	1	0.3
Igneous Lithic	4	1.3
Sedimentary Lithic		
Metamorphic Lithic		
Calcite		
Fe Oxide		
Clay Rims		
Matrix	1	0.3
Total Counts	300	
Total Quartz	179	
Total Feldspars	29	
Total Lithics	4	
Total	212	
Norm. Qtz	84.4	
Norm. Feldspars	13.7	
Norm. Lithics	1.9	

9-1I (Erg-margin)		
Mineral	Counts	% Tot.
Mono	145	48.3
Coarse Poly	17	5.7
Fine Poly	3	1.0
Microcrystalline	3	1.0
Undulose	18	6.0
Plagioclase	17	5.7
K-Feldspar	18	6.0
Calcite Cement	21	7.0
Quartz Cement		
Poikilotropic Cement		
Interpartical Porosity	53	17.7
Intrapartical Porosity	3	1.0
Igneous Lithic	1	0.3
Sedimentary Lithic		
Metamorphic Lithic		
Calcite	1	0.3
Fe Oxide		
Clay Rims		
Matrix		
Total Counts	300	
Total Quartz	186	
Total Feldspars	35	
Total Lithics	1	
Total	222	
Norm. Qtz	83.8	
Norm. Feldspars	15.8	
Norm. Lithics	0.5	

10-1A (Subtidal Ooid-bearing Shoals & Bars)		
Mineral	Counts	% Tot.
Mono	131	43.7
Coarse Poly	22	7.3
Fine Poly	1	0.3
Microcrystalline	2	0.7
Undulose	7	2.3
Plagioclase	3	1.0
K-Feldspar	10	3.3
Calcite Cement	50	16.7
Quartz Cement		
Poikilotropic Cement		
Interpartical Porosity	25	8.3
Intrapartical Porosity		
Igneous Lithic	1	0.3
Sedimentary Lithic	2	0.7
Metamorphic Lithic		
Calcite		
Ooids	31	10.3
Carbonate Fossils	15	5.0
Clay Rims		
Matrix		
Total Counts	300	
Total Quartz	163	
Total Feldspars	13	
Total Lithics	3	
Total	179	
Norm. Qtz	91.1	
Norm. Feldspars	7.3	
Norm. Lithics	1.7	

10-1C2 (Subtidal Ooid-bearing Shoals & Bars)		
Mineral	Counts	% Tot.
Mono	127	42.3
Coarse Poly	21	7.0
Fine Poly	4	1.3
Microcrystalline	1	0.3
Undulose	3	1.0
Plagioclase	2	0.7
K-Feldspar	15	5.0
Calcite Cement	56	18.7
Quartz Cement		
Poikilotropic Cement		
Interpartical Porosity		
Intrapartical Porosity		
Igneous Lithic		
Sedimentary Lithic		
Metamorphic Lithic		
Calcite		
Ooids	41	13.7
Carbonate Fossils	30	10.0
Clay Rims		
Matrix		
Total Counts	300	
Total Quartz	156	
Total Feldspars	17	
Total Lithics	0	
Total	173	
Norm. Qtz	90.2	
Norm. Feldspars	9.8	
Norm. Lithics	0.0	

APPENDIX D
POINT COUNT DATA FOR QmFLt TERNARY DIAGRAMS

To understand the tectonic provenance of each facies, 300-point count was completed on each thin section (two from each facies). Qm represents monocrystalline quartz. F represents plagioclase and K-feldspar grains. Lt represents lithic fragments (L) and polycrystalline quartz grains (Qp).

Table D1: Point count data collected for QmFLt plots for each of the studied facies.

2-9 (Bitter Seep Wash Sandstone)		
Mineral	Counts	% Tot.
Mono	155	51.7
Coarse Poly	25	8.3
Fine Poly	3	1.0
Microcrystalline		
Undulose	8	2.7
Plagioclase	21	7.0
K-Feldspar	5	1.7
Calcite Cement	4	1.3
Quartz Cement	2	0.7
Poikilotropic Cement		
Interpartical Porosity	53	17.7
Intrapartical Porosity	3	1.0
Igneous Lithic		
Sedimentary Lithic	7	2.3
Metamorphic Lithic		
Calcite	13	4.3
Fe Oxide	1	0.3
Clay Rims		
Matrix		
Total Counts	300	
Total Mono Quartz	155	
Total Feldspars	26	
Total Lithics	35	
Total	216	
Norm. Mono Qtz	71.8	
Norm. Feldspars	12.0	
Norm. Lithics	16.2	

4-4 (Bitter Seep Wash Sandstone)		
Mineral	Counts	% Tot.
Mono	152	50.7
Coarse Poly	17	5.7
Fine Poly	9	3.0
Microcrystalline	6	2.0
Undulose	20	6.7
Plagioclase	4	1.3
K-Feldspar	9	3.0
Calcite Cement	24	8.0
Quartz Cement		
Poikilotropic Cement		
Interpartical Porosity	32	10.7
Intrapartical Porosity		
Igneous Lithic	6	2.0
Sedimentary Lithic	7	2.3
Metamorphic Lithic		
Calcite	10	3.3
Fe Oxide	2	0.7
Clay Rims		
Matrix	2	0.7
Total Counts	300	
Total Mono Quartz	152	
Total Feldspars	13	
Total Lithics	45	
Total	210	
Norm. Mono Qtz	72.4	
Norm. Feldspars	6.2	
Norm. Lithics	21.4	

5-1A1 (Sabkha)		
Mineral	Counts	% Tot.
Mono	98	32.7
Coarse Poly	36	12.0
Fine Poly		
Microcrystalline	2	0.7
Undulose	33	11.0
Plagioclase	26	8.7
K-Feldspar	14	4.7
Calcite Cement	28	9.3
Quartz Cement		
Poikilotropic Cement		
Interpartical Porosity	4	1.3
Intrapartical Porosity		
Igneous Lithic		
Sedimentary Lithic		
Metamorphic Lithic		
Calcite	18	6.0
Fe Oxide	5	1.7
Gypsum	13	4.3
Clay Rims		
Matrix	23	7.7
Total Counts	300	
Total Mono Quartz	98	
Total Feldspars	40	
Total Lithics	38	
Total	176	
Norm. Mono Qtz	55.7	
Norm. Feldspars	22.7	
Norm. Lithics	21.6	

5-1B1 (Sabkha)		
Mineral	Counts	% Tot.
Mono	117	39.0
Coarse Poly	9	3.0
Fine Poly	1	0.3
Microcrystalline	1	0.3
Undulose	12	4.0
Plagioclase	28	9.3
K-Feldspar	19	6.3
Calcite Cement	49	16.3
Quartz Cement		
Poikilotropic Cement		
Interpartical Porosity	12	4.0
Intrapartical Porosity		
Igneous Lithic		
Sedimentary Lithic		
Metamorphic Lithic		
Calcite	5	1.7
Fe Oxide	7	2.3
Gypsum	3	1.0
Clay Rims		
Matrix	37	12.3
Total Counts	300	
Total Mono Quartz	117	
Total Feldspars	47	
Total Lithics	11	
Total	175	
Norm. Mono Qtz	66.9	
Norm. Feldspars	26.9	
Norm. Lithics	6.3	

6-1B1 (Middle Intertidal)		
Mineral	Counts	% Tot.
Mono	86	28.7
Coarse Poly	19	6.3
Fine Poly	7	2.3
Microcrystalline	1	0.3
Undulose	19	6.3
Plagioclase	32	10.7
K-Feldspar	19	6.3
Calcite Cement	63	21.0
Quartz Cement		
Poikilotropic Cement		
Interpartical Porosity	7	2.3
Intrapartical Porosity		
Igneous Lithic		
Sedimentary Lithic		
Metamorphic Lithic		
Calcite	4	1.3
Fe Oxide	6	2.0
Gypsum	2	0.7
Clay Rims		
Matrix	35	11.7
Total Counts	300	
Total Mono Quartz	86	
Total Feldspar	51	
Total Lithics	27	
Total	164	
Norm. Mono Qtz	52.4	
Norm. Feldspars	31.1	
Norm. Lithics	16.5	

6-1E2 (Middle Intertidal)		
Mineral	Counts	% Tot.
Mono	92	30.7
Coarse Poly	33	11.0
Fine Poly	4	1.3
Microcrystalline	1	0.3
Undulose	2	0.7
Plagioclase	25	8.3
K-Feldspar	34	11.3
Calcite Cement	38	12.7
Quartz Cement		
Poikilotropic Cement		
Interpartical Porosity	4	1.3
Intrapartical Porosity		
Igneous Lithic		
Sedimentary Lithic		
Metamorphic Lithic		
Calcite		
Fe Oxide	5	1.7
Clay Rims		
Matrix	62	20.7
Total Counts	300	
Total Mono Quartz	92	
Total Feldspars	59	
Total Lithics	38	
Total	189	
Norm. Mono Qtz	48.7	
Norm. Feldspars	31.2	
Norm. Lithics	20.1	

7-1B (Storm)		%
Mineral	Counts	Tot.
Mono	132	44.0
Coarse Poly	24	8.0
Fine Poly	4	1.3
Microcrystalline	15	5.0
Undulose	7	2.3
Plagioclase	5	1.7
K-Feldspar	17	5.7
Calcite Cement	81	27.0
Quartz Cement		
Poikilotropic Cement	13	4.3
Interpartical Porosity	1	0.3
Intrapartical Porosity		
Igneous Lithic		
Sedimentary Lithic		
Metamorphic Lithic		
Calcite		
Fe Oxide	1	0.3
Clay Rims		
Matrix		
Total Counts	300	
Total Mono Quartz	132	
Total Feldspars	22	
Total Lithics	43	
Total	197	
Norm. Mono Qtz	67.0	
Norm. Feldspars	11.2	
Norm. Lithics	21.8	

7-1E (Storm)		%
Mineral	Counts	Tot.
Mono	101	33.7
Coarse Poly	25	8.3
Fine Poly	9	3.0
Microcrystalline	12	4.0
Undulose	7	2.3
Plagioclase	6	2.0
K-Feldspar	49	16.3
Calcite Cement	73	24.3
Quartz Cement		
Poikilotropic Cement	14	4.7
Interpartical Porosity		
Intrapartical Porosity		
Igneous Lithic	2	0.7
Sedimentary Lithic		
Metamorphic Lithic		
Calcite		
Fe Oxide	2	0.7
Clay Rims		
Matrix		
Total Counts	300	
Total Mono Quartz	101	
Total Feldspars	55	
Total Lithics	48	
Total	204	
Norm. Mono Qtz	49.5	
Norm. Feldspars	27.0	
Norm. Lithics	23.5	

8-1F (Lower Intertidal Channels)		%
Mineral	Counts	Tot.
Mono	118	39.3
Coarse Poly	20	6.7
Fine Poly	1	0.3
Microcrystalline		
Undulose	2	0.7
Plagioclase	26	8.7
K-Feldspar	23	7.7
Calcite Cement	52	17.3
Quartz Cement		
Poikilotropic Cement		
Interpartical Porosity	52	17.3
Intrapartical Porosity		
Igneous Lithic	4	1.3
Sedimentary Lithic		
Metamorphic Lithic		
Calcite	1	0.3
Fe Oxide		
Clay Rims	1	0.3
Matrix		
Total Counts	300	
Total Mono Quartz	118	
Total Feldspars	49	
Total Lithics	25	
Total	192	
Norm. Mono Qtz	61.5	
Norm. Feldspars	25.5	
Norm. Lithics	13.0	

8-1G2 (Lower Intertidal Channels)		
Mineral	Counts	% Tot.
Mono	128	42.7
Coarse Poly	15	5.0
Fine Poly	4	1.3
Microcrystalline	1	0.3
Undulose	3	1.0
Plagioclase	18	6.0
K-Feldspar	19	6.3
Calcite Cement	38	12.7
Quartz Cement		
Poikilotropic Cement		
Interpartical Porosity	67	22.3
Intrapartical Porosity		
Igneous Lithic	7	2.3
Sedimentary Lithic		
Metamorphic Lithic		
Calcite		
Fe Oxide		
Clay Rims		
Matrix		
Total Counts	300	
Total Mono Quartz	128	
Total Feldspars	37	
Total Lithics	27	
Total	192	
Norm. Mono Qtz	66.7	
Norm. Feldspars	19.3	
Norm. Lithics	14.1	

9-1E (Erg-margin)		
Mineral	Counts	% Tot.
Mono	159	53.0
Coarse Poly	14	4.7
Fine Poly	4	1.3
Microcrystalline	1	0.3
Undulose	1	0.3
Plagioclase	11	3.7
K-Feldspar	18	6.0
Calcite Cement	44	14.7
Quartz Cement		
Poikilotropic Cement		
Interpartical Porosity	42	14.0
Intrapartical Porosity	1	0.3
Igneous Lithic	4	1.3
Sedimentary Lithic		
Metamorphic Lithic		
Calcite		
Fe Oxide		
Clay Rims		
Matrix	1	0.3
Total Counts	300	
Total Mono Quartz	159	
Total Feldspars	29	
Total Lithics	23	
Total	211	
Norm. Mono Qtz	75.4	
Norm. Feldspars	13.7	
Norm. Lithics	10.9	

9-1I (Erg-margin)		
Mineral	Counts	% Tot.
Mono	145	48.3
Coarse Poly	17	5.7
Fine Poly	3	1.0
Microcrystalline	3	1.0
Undulose	18	6.0
Plagioclase	17	5.7
K-Feldspar	18	6.0
Calcite Cement	21	7.0
Quartz Cement		
Poikilotropic Cement		
Interpartical Porosity	53	17.7
Intrapartical Porosity	3	1.0
Igneous Lithic	1	0.3
Sedimentary Lithic		
Metamorphic Lithic		
Calcite	1	0.3
Fe Oxide		
Clay Rims		
Matrix		
Total Counts	300	
Total Mono Quartz	145	
Total Feldspars	35	
Total Lithics	24	
Total	204	
Norm. Mono Qtz	71.1	
Norm. Feldspars	17.2	
Norm. Lithics	11.8	

10-1A (Subtidal Ooid-bearing Shoals & Bars)			10-1C2 (Subtidal Ooid-bearing Shoals & Bars)		
Mineral	Counts	% Tot.	Mineral	Counts	% Tot.
Mono	131	43.7	Mono	127	42.3
Coarse Poly	22	7.3	Coarse Poly	21	7.0
Fine Poly	1	0.3	Fine Poly	4	1.3
Microcrystalline	2	0.7	Microcrystalline	1	0.3
Undulose	7	2.3	Undulose	3	1.0
Plagioclase	3	1.0	Plagioclase	2	0.7
K-Feldspar	10	3.3	K-Feldspar	15	5.0
Calcite Cement	50	16.7	Calcite Cement	56	18.7
Quartz Cement			Quartz Cement		
Poikilotropic Cement			Poikilotropic Cement		
Interpartical Porosity	25	8.3	Interpartical Porosity		
Intrapartical Porosity			Intrapartical Porosity		
Igneous Lithic	1	0.3	Igneous Lithic		
Sedimentary Lithic	2	0.7	Sedimentary Lithic		
Metamorphic Lithic			Metamorphic Lithic		
Calcite			Calcite		
Ooids	31	10.3	Ooids	41	13.7
Carbonate Fossils	15	5.0	Carbonate Fossils	30	10.0
Clay Rims			Clay Rims		
Matrix			Matrix		
Total Counts	300		Total Counts	300	
Total Mono Quartz	131		Total Mono Quartz	127	
Total Feldspars	13		Total Feldspars	17	
Total Lithics	28		Total Lithics	26	
Total	172		Total	170	
Norm. Mono Qtz	76.2		Norm. Mono Qtz	74.7	
Norm. Feldspars	7.6		Norm. Feldspars	10.0	
Norm. Lithics	16.3		Norm. Lithics	15.3	

APPENDIX E
POINT COUNT DATA FOR QmPK TERNARY DIAGRAMS

To understand the tectonic provenance of each facies, 300-point count was completed on each thin section (two from each facies). Qm represents monocrystalline quartz. P represents plagioclase and K represents K-feldspar grains.

Table E1: Point count data collected for QmPK plots for each of the studied facies.

2-9 (Bitter Seep Wash Sandstone)				4-4 (Bitter Seep Wash Sandstone)				5-1A1 (Sabkha)		
Mineral	Counts	% Tot.		Mineral	Counts	% Tot.		Mineral	Counts	% Tot.
Mono	155	51.7		Mono	152	50.7		Mono	98	32.7
Coarse Poly	25	8.3		Coarse Poly	17	5.7		Coarse Poly	36	12.0
Fine Poly	3	1.0		Fine Poly	9	3.0		Fine Poly		
Microcrystalline				Microcrystalline	6	2.0		Microcrystalline	2	0.7
Undulose	8	2.7		Undulose	20	6.7		Undulose	33	11.0
Plagioclase	21	7.0		Plagioclase	4	1.3		Plagioclase	26	8.7
K-Feldspar	5	1.7		K-Feldspar	9	3.0		K-Feldspar	14	4.7
Calcite Cement	4	1.3		Calcite Cement	24	8.0		Calcite Cement	28	9.3
Quartz Cement	2	0.7		Quartz Cement				Quartz Cement		
Poikilotropic Cement				Poikilotropic Cement				Poikilotropic Cement		
Interpartical Porosity	53	17.7		Interpartical Porosity	32	10.7		Interpartical Porosity	4	1.3
Intrapartical Porosity	3	1.0		Intrapartical Porosity				Intrapartical Porosity		
Igneous Lithic		0.0		Igneous Lithic	6	2.0		Igneous Lithic		
Sedimentary Lithic	7	2.3		Sedimentary Lithic	7	2.3		Sedimentary Lithic		
Metamorphic Lithic				Metamorphic Lithic				Metamorphic Lithic		
Calcite	13	4.3		Calcite	10	3.3		Calcite	18	6.0
Fe Oxide	1	0.3		Fe Oxide	2	0.7		Fe Oxide	5	1.7
								Gypsum	13	4.3
Clay Rims				Clay Rims				Clay Rims		
Matrix				Matrix	2	0.7		Matrix	23	7.7
Total Counts	300			Total Counts	300			Total Counts	300	
Total Mono Quartz	155			Total Mono Quartz	152			Total Mono Quartz	98	
Total K-Feldspar	5			Total K-Feldspar	9			Total K-Feldspar	14	
Total Plagioclase	21			Total Plagioclase	4			Total Plagioclase	26	
Total	181			Total	165			Total	138	
Norm. Mono Qtz	85.6			Norm. Mono Qtz	92.1			Norm. Mono Qtz	71.0	
Norm. K-Feldspar	2.8			Norm. K-Feldspar	5.5			Norm. K-Feldspar	10.1	
Norm. Plagioclase	11.6			Norm. Plagioclase	2.4			Norm. Plagioclase	18.8	

5-1B1 (Sabkha)		
Mineral	Counts	% Tot.
Mono	117	39.0
Coarse Poly	9	3.0
Fine Poly	1	0.3
Microcrystalline	1	0.3
Undulose	12	4.0
Plagioclase	28	9.3
K-Feldspar	19	6.3
Calcite Cement	49	16.3
Quartz Cement		
Poikilotropic Cement		
Interpartical Porosity	12	4.0
Intrapartical Porosity		
Igneous Lithic		
Sedimentary Lithic		
Metamorphic Lithic		
Calcite	5	1.7
Fe Oxide	7	2.3
Gypsum	3	1.0
Clay Rims		
Matrix	37	12.3
Total Counts	300	
Total Mono Quartz	117	
Total K-Feldspar	19	
Total Plagioclase	28	
Total	164	
Norm. Mono Qtz	71.3	
Norm. K-Feldspar	11.6	
Norm. Plagioclase	17.1	

6-1B1 (Middle Intertidal)		
Mineral	Counts	% Tot.
Mono	86	28.7
Coarse Poly	19	6.3
Fine Poly	7	2.3
Microcrystalline	1	0.3
Undulose	19	6.3
Plagioclase	32	10.7
K-Feldspar	19	6.3
Calcite Cement	63	21.0
Quartz Cement		
Poikilotropic Cement		
Interpartical Porosity	7	2.3
Intrapartical Porosity		
Igneous Lithic		
Sedimentary Lithic		
Metamorphic Lithic		
Calcite	4	1.3
Fe Oxide	6	2.0
Gypsum	2	0.7
Clay Rims		
Matrix	35	11.7
Total Counts	300	
Total Mono Quartz	86	
Total K-Feldspar	19	
Total Plagioclase	32	
Total	137	
Norm. Mono Qtz	62.8	
Norm. K-Feldspar	13.9	
Norm. Plagioclase	23.4	

6-1E2 (Middle Intertidal)		
Mineral	Counts	% Tot.
Mono	92	30.7
Coarse Poly	33	11.0
Fine Poly	4	1.3
Microcrystalline	1	0.3
Undulose	2	0.7
Plagioclase	25	8.3
K-Feldspar	34	11.3
Calcite Cement	38	12.7
Quartz Cement		
Poikilotropic Cement		
Interpartical Porosity	4	1.3
Intrapartical Porosity		
Igneous Lithic		
Sedimentary Lithic		
Metamorphic Lithic		
Calcite		
Fe Oxide	5	1.7
Clay Rims		
Matrix	62	20.7
Total Counts	300	
Total Mono Quartz	92	
Total K-Feldspar	34	
Total Plagioclase	25	
Total	151	
Norm. Mono Qtz	60.9	
Norm. K-Feldspar	22.5	
Norm. Plagioclase	16.6	

7-1B (Storm)		%
Mineral	Counts	Tot.
Mono	132	44.0
Coarse Poly	24	8.0
Fine Poly	4	1.3
Microcrystalline	15	5.0
Undulose	7	2.3
Plagioclase	5	1.7
K-Feldspar	17	5.7
Calcite Cement	81	27.0
Quartz Cement		
Poikilotropic Cement	13	4.3
Interpartical Porosity	1	0.3
Intrapartical Porosity		
Igneous Lithic		
Sedimentary Lithic		
Metamorphic Lithic		
Calcite		
Fe Oxide	1	0.3
Clay Rims		
Matrix		
Total Counts	300	
Total Mono Quartz	132	
Total K-Feldspar	17	
Total Plagioclase	5	
Total	154	
Norm. Mono Qtz	85.7	
Norm. K-Feldspar	11.0	
Norm. Plagioclase	3.2	

7-1E (Storm)		%
Mineral	Counts	Tot.
Mono	101	33.7
Coarse Poly	25	8.3
Fine Poly	9	3.0
Microcrystalline	12	4.0
Undulose	7	2.3
Plagioclase	6	2.0
K-Feldspar	49	16.3
Calcite Cement	73	24.3
Quartz Cement		
Poikilotropic Cement	14	4.7
Interpartical Porosity		
Intrapartical Porosity		
Igneous Lithic	2	0.7
Sedimentary Lithic		
Metamorphic Lithic		
Calcite		
Fe Oxide	2	0.7
Clay Rims		
Matrix		
Total Counts	300	
Total Mono Quartz	101	
Total K-Feldspar	49	
Total Plagioclase	6	
Total	156	
Norm. Mono Qtz	64.7	
Norm. K-Feldspar	31.4	
Norm. Plagioclase	3.8	

8-1F (Lower Intertidal Channels)		%
Mineral	Counts	Tot.
Mono	118	39.3
Coarse Poly	20	6.7
Fine Poly	1	0.3
Microcrystalline		
Undulose	2	0.7
Plagioclase	26	8.7
K-Feldspar	23	7.7
Calcite Cement	52	17.3
Quartz Cement		
Poikilotropic Cement		
Interpartical Porosity	52	17.3
Intrapartical Porosity		
Igneous Lithic	4	1.3
Sedimentary Lithic		
Metamorphic Lithic		
Calcite	1	0.3
Fe Oxide		
Clay Rims	1	0.3
Matrix		
Total Counts	300	
Total Mono Quartz	118	
Total K-Feldspar	23	
Total Plagioclase	26	
Total	167	
Norm. Mono Qtz	70.7	
Norm. K-Feldspar	13.8	
Norm. Plagioclase	15.6	

8-1G2 (Lower Intertidal Channels)		
Mineral	Counts	% Tot.
Mono	128	42.7
Coarse Poly	15	5.0
Fine Poly	4	1.3
Microcrystalline	1	0.3
Undulose	3	1.0
Plagioclase	18	6.0
K-Feldspar	19	6.3
Calcite Cement	38	12.7
Quartz Cement		
Poikilotropic Cement		
Interpartical Porosity	67	22.3
Intrapartical Porosity		
Igneous Lithic	7	2.3
Sedimentary Lithic		
Metamorphic Lithic		
Calcite		
Fe Oxide		
Clay Rims		
Matrix		
Total Counts	300	
Total Mono Quartz	128	
Total K-Feldspar	19	
Total Plagioclase	18	
Total	165	
Norm. Mono Qtz	77.6	
Norm. K-Feldspar	11.5	
Norm. Plagioclase	10.9	

9-1E (Erg-margin)		
Mineral	Counts	% Tot.
Mono	159	53.0
Coarse Poly	14	4.7
Fine Poly	4	1.3
Microcrystalline	1	0.3
Undulose	1	0.3
Plagioclase	11	3.7
K-Feldspar	18	6.0
Calcite Cement	44	14.7
Quartz Cement		
Poikilotropic Cement		
Interpartical Porosity	42	14.0
Intrapartical Porosity	1	0.3
Igneous Lithic	4	1.3
Sedimentary Lithic		
Metamorphic Lithic		
Calcite		
Fe Oxide		
Clay Rims		
Matrix	1	0.3
Total Counts	300	
Total Mono Quartz	159	
Total K-Feldspar	18	
Total Plagioclase	11	
Total	188	
Norm. Mono Qtz	84.6	
Norm. K-Feldspar	9.6	
Norm. Plagioclase	5.9	

9-1I (Erg-margin)		
Mineral	Counts	% Tot.
Mono	145	48.3
Coarse Poly	17	5.7
Fine Poly	3	1.0
Microcrystalline	3	1.0
Undulose	18	6.0
Plagioclase	17	5.7
K-Feldspar	18	6.0
Calcite Cement	21	7.0
Quartz Cement		
Poikilotropic Cement		
Interpartical Porosity	53	17.7
Intrapartical Porosity	3	1.0
Igneous Lithic	1	0.3
Sedimentary Lithic		
Metamorphic Lithic		
Calcite	1	0.3
Fe Oxide		
Clay Rims		
Matrix		
Total Counts	300	
Total Mono Quartz	145	
Total K-Feldspar	18	
Total Plagioclase	17	
Total	180	
Norm. Mono Qtz	80.6	
Norm. K-Feldspar	10.0	
Norm. Plagioclase	9.4	

10-1A (Subtidal Ooid-bearing Shoals & Bars)		
Mineral	Counts	% Tot.
Mono	131	43.7
Coarse Poly	22	7.3
Fine Poly	1	0.3
Microcrystalline	2	0.7
Undulose	7	2.3
Plagioclase	3	1.0
K-Feldspar	10	3.3
Calcite Cement	50	16.7
Quartz Cement		
Poikilotropic Cement		
Interpartical Porosity	25	8.3
Intrapartical Porosity		
Igneous Lithic	1	0.3
Sedimentary Lithic	2	0.7
Metamorphic Lithic		
Calcite		
Ooids	31	10.3
Carbonate Fossils	15	5.0
Clay Rims		
Matrix		
Total Counts	300	
Total Mono Quartz	131	
Total K-Feldspar	10	
Total Plagioclase	3	
Total	144	
Norm. Mono Qtz	91.0	
Norm. K-Feldspar	6.9	
Norm. Plagioclase	2.1	

10-1C2 (Subtidal Ooid-bearing Shoals & Bars)		
Mineral	Counts	% Tot.
Mono	127	42.3
Coarse Poly	21	7.0
Fine Poly	4	1.3
Microcrystalline	1	0.3
Undulose	3	1.0
Plagioclase	2	0.7
K-Feldspar	15	5.0
Calcite Cement	56	18.7
Quartz Cement		
Poikilotropic Cement		
Interpartical Porosity		
Intrapartical Porosity		
Igneous Lithic		
Sedimentary Lithic		
Metamorphic Lithic		
Calcite		
Ooids	41	13.7
Carbonate Fossils	30	10.0
Clay Rims		
Matrix		
Total Counts	300	
Total Mono Quartz	127	
Total K-Feldspar	15	
Total Plagioclase	2	
Total	144	
Norm. Mono Qtz	88.2	
Norm. K-Feldspar	10.4	
Norm. Plagioclase	1.4	

140

APPENDIX F
STRATIGRAPHIC COLUMNS FOR THE WEST SAN RAFAEL SWELL (WSRS) AND
EAST SAN RAFAEL SECTION (ESRS)

       Stratigraphic columns were created from measured sections at the WSRS and ESRS sections. These columns are highly condensed and as a result some grouping has occurred in the facies assignments. Each stratigraphic column is composed of a facies assignment column and a lithologic column. Key characteristics have been added to the stratigraphic column.
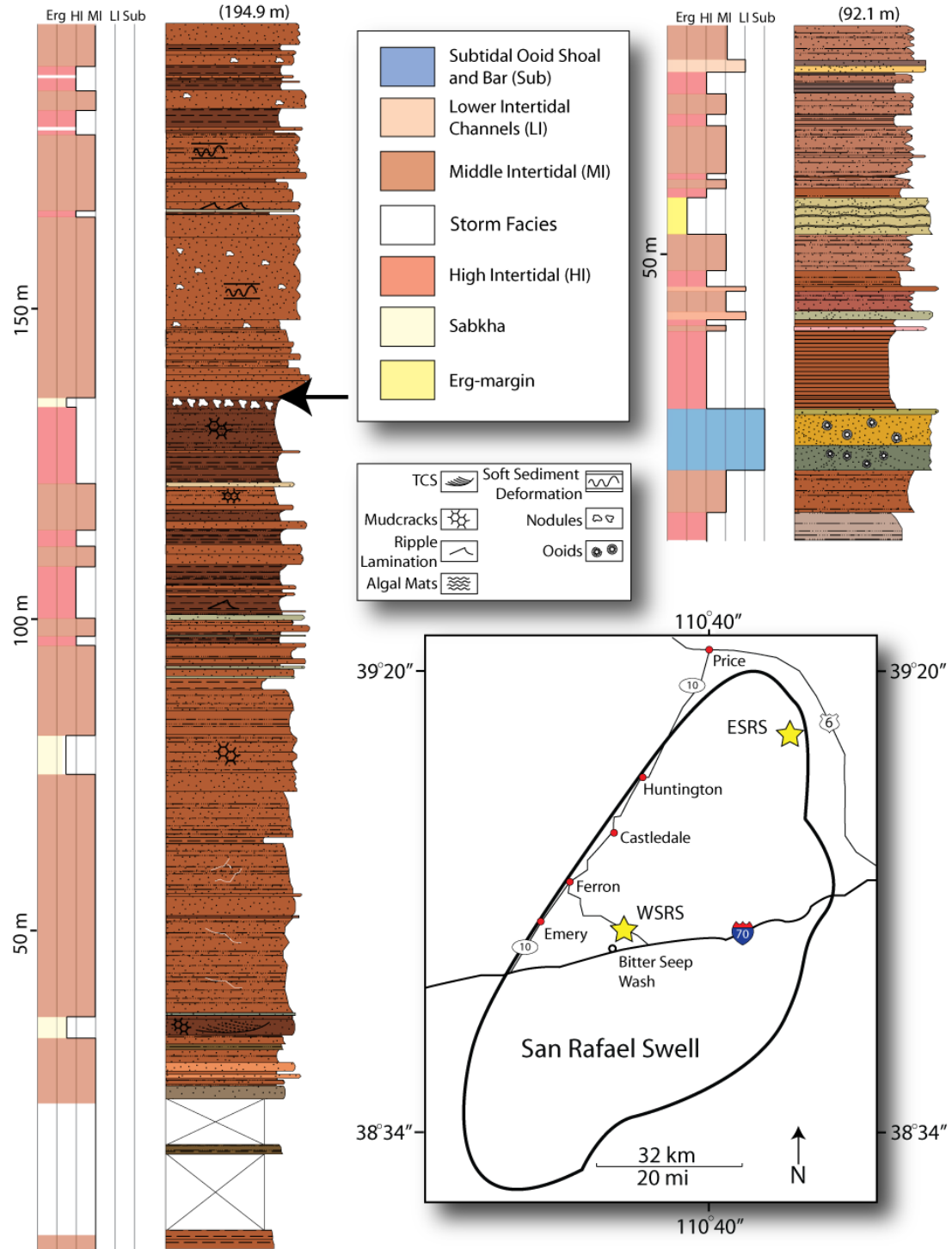
Figure F1: Stratigraphic columns representing the WSRS and ESRS sections. The first column of each section is the facies assigned to that section of rock. The lithologic column shows relative grain size and the weathering profile. Due to the condensed version of these stratigraphic columns, some grouping has occurred in the facies assignments. The black arrow indicates the approximate stratigraphic position of the BSWS located approximately 5km (3.1mi) south of the WSRS section. This has been modified from Hicks and others (2010).